# Formation of Alumina Coatings by Thermal and Anodic Oxidation Processes and their Characterization

*By*
**Rupesh Kumar Choudhary**

**ENGG01201204015**

**Bhabha Atomic Research Centre, Mumbai**

***A thesis submitted to the***
***Board of Studies in Engineering Sciences***

***In partial fulfillment of requirements***
***for the Degree of***

**DOCTOR OF PHILOSOPHY**
***of***
**HOMI BHABHA NATIONAL INSTITUTE**

**July, 2019**

# Homi Bhabha National Institute[1]

## Recommendations of the Viva Voce Committee

As members of the Viva Voce Committee, we certify that we have read the dissertation prepared by **Rupesh Kumar Choudhary** entitled "**Formation of Alumina Coatings by Thermal and Anodic Oxidation Processes and their Characterization**" and recommend that it may be accepted as fulfilling the thesis requirement for the award of Degree of Doctor of Philosophy.

| | | |
|---|---|---|
| Chairman - Name & Signature with date | Prof.R. Tewari | 28/08/2020 |
| Guide / Convener - Name & Signature with date | Prof. V. Kain | 28/8/2020 |
| Examiner - Name & Signature with date | Prof. GVS Nageswara Rao | |
| Member 1- Name & Signature with date | Prof. A. K. Arya | 28/08/2020 |
| Member 2- Name & Signature with date | Prof. R. Kapoor | Rajeev Kapoor<br>28/8/2020 |
| Member 3- Name & Signature with date | Prof. S. Majumdar | Sanjib Majumdar<br>28/08/2020 |

Final approval and acceptance of this thesis is contingent upon the candidate's submission of the final copies of the thesis to HBNI.

I hereby certify that I have read this thesis prepared under my direction and recommend that it may be accepted as fulfilling the thesis requirement.

Sept. 21, 2020

**Date:**

**Place: Mumbai**

**Signature**

**Guide**

---

[1] This page is to be included only for final submission after successful completion of viva voce.

# STATEMENT BY AUTHOR

This dissertation has been submitted in partial fulfillment of requirements for an advanced degree at Homi Bhabha National Institute (HBNI) and is deposited in the Library to be made available to borrowers under rules of the HBNI.

Brief quotations from this dissertation are allowable without special permission, provided that accurate acknowledgement of source is made. Requests for permission for extended quotation from or reproduction of this manuscript in whole or in part may be granted by the Competent Authority of HBNI when in his or her judgment the proposed use of the material is in the interests of scholarship. In all other instances, however, permission must be obtained from the author.

Rupesh Kumar Chaudhary

Rupesh Kumar Choudhary

# DECLARATION

I, hereby declare that the investigation presented in the thesis has been carried out by me. The work is original and has not been submitted earlier as a whole or in part for a degree / diploma at this or any other Institution / University.

Rupesh Kumar Chaudhary

Rupesh Kumar Choudhary

# List of Publications arising from the thesis

## Journal

1. R. K. Choudhary, P. Mishra, V. Kain, K. Singh, S. Kumar, and J. K. Chakravartty, Scratch Behavior of Aluminum Anodized in Oxalic Acid: Effect of Anodizing Potential, *Surf. Coat. Technol.*, 2015, **283**, p 135–147
2. R. K. Choudhary, V. Kain, and R. C. Hubli, Formation of Alumina-aluminide Coatings on Ferritic-martensitic T91 Steel, *J. Min. Metall. Sect. B-Metall.*, 2014, **50**, p 165–170
3. R. K. Choudhary, V. Kain, and R. C. Hubli, Stirring Effects on Aluminium Coatings Electrodeposited in Ionic Liquids, *Surf. Eng.*, 2014, **30**, p 562–567
4. R. K. Choudhary, S. Rajak, A. C. Bidaye, V. Kain, and R. C. Hubli, Substrate and Current Density Effects on Electrodeposited Aluminium Coatings, *Surf. Eng.*, 2013, **29**, p 677–682

## Conferences

1. R. K. Choudhary, P. Mishra, S. Kumar, A. K. Debnath, and V. Kain, Development and Characterization of Porous Anodic Aluminum Oxide Films Formed in a Mixture of Oxalic Acid and Citric Acid, International Conference on Frontiers in Materials from Basic Science to Real-time Applications, 2019, CNMS, Jain University, Bengaluru
2. R. K. Choudhary, P. Mishra, A. K. Debnath, and V. Kain, Structural and Optical Properties of Anodic Tantalum Pentoxide Films, International Conference on Frontiers in Materials from Basic Science to Real-time Applications, 2019, CNMS, Jain University, Bengaluru

Rupesh Kumar Chaudhary

Rupesh Kumar Choudhary

**Dedicated to my parents**

# ACKNOWLEDGEMENTS

At the verge of achieving this milestone I would like to express my sincere gratitude to a number of people. At the outset I express greatest respect and honour to my childhood School teachers **Shri R. K. Jha** and **Shri A. K. Jha** for their unique and easy to understand way of learning Science. To be honest it would not be inappropriate to accept that they truly motivated me to pursue a carrier of engineering aptitude. I also express a deep sense of gratitude to the professors of Metallurgical Engineering Department, BIT Sindri, Dhanbad from whom I could learn with clarity the basics of Metallurgy during my undergraduate programme.

I express my sincere thanks to **Dr. A. C. Bidaye (Ex-head, SES/MPD, BARC)** and **Dr. R. C. Hubli (Ex-head, MPD, BARC)** who explained me thoroughly about the scientific importance and scope of the present work and provided me a golden opportunity to undertake this assignment as a Ph.D. research project. They also helped me a lot to conceptualize the scientific merit of the project that could generate keen interest in me to avail this opportunity.

I express my deepest sense of gratitude and appreciation to **Prof. Vivekanand Kain** for his incredible guidance throughout the research project. I am fortunate enough and feel indebted for getting the continuous support, motivation, encouragement and extremely fruitful and critical suggestions, despite of his busy schedule for highly important projects and matters of the Division. For such a wonderful guidance I express sincere thanks to him from the bottom of my heart.

My special thanks go to **Shri Prabhat Mishra, Head, SES/MP&CED, BARC** who continuously urged me for timely completion of the project and provided me with valuable suggestions time-to-time. The scientific discussion with him on various technical and scientific aspects could be of great help to me.

I extend my deep sense of gratitude and thanks to **Dr. Kulwant Singh**, **SO/H, MSD**, **BARC**, **Dr. Abhijit Ghosh, SO/H, G&AMD, BARC, Dr. A. K. Debnath, SO/H, TPD, BARC** and **Dr. A. K. Sahu, SO/F, G&AMD, BARC** for their extensive cooperation during analytical study part of the research project.

I would not forget to remember **Shri Vishal B. Nikam, Shri Pawan Kumar Verma, Shri Jamil Haider** and **Mrs. K. P. Sreeshma**, for their extensive cooperation during experiments, my sincere thanks to all of them.

This thesis would not have been completed without the blessings, love, care and support of my parents, brother, sisters and in-laws. The deep interest of my wife **Mrs. Archana Choudhary** for higher education motivated me a lot to complete this thesis. The enjoyment gained while playing with my lovely daughter **Miss Aaradhya** could keep me lighter and fresh enough to complete this thesis without any stress.

Finally, I express deep sense of gratitude to all my friends, colleagues, relatives and well wishers for their cooperation and help during the entire tenure of this project.

Rupesh Kumar Choudhary

# CONTENTS

# List of Figures

# List of Tables

# Chapter-9

## Conclusions and Scope for Future Work

### 9.1 Conclusions

In the present work, alumina coatings were developed on Fe9Cr1Mo steel and aluminum substrates for diversified applications including the two main potential applications, use of alumina coating as a tritium permeation barrier for test blanket modules of fusion reactors and corrosion protection of aluminum. A detailed literature survey was done on the methods of formation, characteristics and properties of alumina coatings and the aspects not covered in literature were highlighted. Based on the gap areas prevailing in literature the alumina coatings were developed by two different approaches, in the first approach alumina coatings were formed on Fe9Cr1Mo steel mainly by thermal oxidation of the aluminum electrochemically obtained from $AlCl_3$-EMIC ionic liquid bath. The so formed alumina coatings were studied for crystal structure, chemical composition and scratch adhesion. This study also included establishing the effect of unexplored parameters such as substrate types and their pre-treatments, ionic salt purity, applied current density and agitation of the electrolytic bath on the growth rate, crystal structure, chemical composition, morphology, topography, roughness and adhesion of the electrodeposited aluminum.

The following conclusions were drawn from the studies done on electrodeposition of aluminum on mild steel, copper and Fe9Cr1Mo steel substrates using $AlCl_3$-EMIC ionic liquid bath and the alumina layers formed on Fe9Cr1Mo steel by thermal oxidation of the electrochemically deposited aluminum.

- A simple chemical treatment to a low grade (but cheap) $AlCl_3$ (98%)–EMIC (95%) ionic liquid enabled it to be efficiently used for electroplating of aluminum having purity better than 99%, on copper and mild steel substrates. However, in comparison to the high purity baths the cathode current efficiency was relatively low in this case. The cathode current efficiency decreased further on increasing the deposition current density. In comparison to polished copper and mild steel surfaces, the adhesion of aluminum was much better on wet alumina blasted mild steel substrates.

- Solution stirring enabled electrodeposition of aluminum on wet alumina blasted Fe9Cr1Mo steel substrate in $AlCl_3$ (98%)–EMIC (98%) ionic liquid at room temperature, at a current density of 20 $mAcm^{-2}$ or higher, which was otherwise unachievable. This could demonstrate the role of concentration polarization during electrodeposition of aluminum in ionic liquids. Solution stirring had a pronounced effect on the thickness and roughness of aluminum coatings formed on wet alumina blasted Fe9Cr1Mo steel. The coating thickness increased linearly on increasing the stirring speed. However, at a stirring speed as high as 800 rpm the obtained coating was highly rough (Rq>16 µm) compared to the roughness of 4–5 µm at 200–600 rpm. Solution stirring had a large impact on the preferred orientation of the crystallographic planes of aluminum. In comparison to the aluminum deposited at 200 rpm the aluminum obtained at 800 rpm showed 26% increase in normalized intensity of (111) reflection, but the intensity of (200) reflection decreased by 37%. Stirring speed of 200–400 rpm was found to be optimum for depositing bright, smooth and adherent aluminum coatings on Fe9Cr1Mo steel from $AlCl_3$ (98%)–EMIC (98%) ionic liquid at room temperature.
- Electrodeposition of aluminum in $AlCl_3$ (98%)-EMIC (98%) ionic liquid followed by a two-step thermal oxidation resulted in the formation of amorphous but adherent alumina coatings on Fe9Cr1Mo steel. Thermal oxidation also resulted in the formation of $Fe_2Al_5$, $Fe_3Al$ and $AlCr_2$ intermetallics by reaction of aluminum with the Fe9Cr1Mo steel

substrate. These intermetallics were present at the interface between unreacted aluminum and substrate. The alumina coatings showed no major adhesive delamination up to 20N.

In the second approach, alumina coatings were formed on aluminum substrate by anodization of aluminum metal in 10% oxalic acid and mixtures of oxalic acid and citric acid of different concentrations. The obtained coatings were studied in detail for crystal structure, chemical composition, morphology, topography, roughness, hardness, electrical resistivity, cohesive and adhesive strength, and wear and friction behaviour with a special emphasis given to the scratch testing. During anodization the effect of anodizing potential and bath concentration on the characteristics and properties of the alumina coatings were studied.

The following conclusions were drawn from this study.

- Anodization of aluminum in 10% oxalic acid at 10–30V leads to the formation of amorphous alumina on aluminum base. At higher potentials the alumina coating contained a marginally higher oxygen concentration. A higher anodizing potential leads to the formation of a porous and rougher anodic coating. The electrical resistivity of anodic coating was lower than that of the pure alumina reported in literature, and the resistivity increased on increasing the potential during anodization. A higher anodizing potential leads to the formation of a harder alumina coating on aluminum substrate. Thickness, average roughness and porosity had a marked effect on the adhesive strength of the coatings. A thicker, rougher or more porous alumina coating formed at higher potentials displayed low adhesive strength. The use of ultrasound agitation during anodization made the coatings more uniform.
- Aluminum anodization experiments conducted in a mixed solution of oxalic acid and citric acid established that bath concentration had no relation with the formation of crystalline oxide and the alumina coatings were amorphous irrespective of the bath

concentration used for anodization. The oxygen concentration of the anodic oxide coatings formed on aluminum was found to increase linearly with anodizing potential but the stoichiometric alumina was formed at 40V. The porosity of anodic coatings increased linearly as the anodizing potential was increased. However, bath concentration had no major impact on porosity of the coatings.

## 9.2 Scope for future work

The purpose of developing alumina coatings on Fe9Cr1Mo steel was the potential use of this coating as a tritium permeation barrier for fusion reactors. Therefore, the applicability of such coatings should be demonstrated by means of simulated tritium permeation tests and this may be considered as a future work. Similarly, it was shown that the anodizing potential had a major influence on the morphology and porosity of the anodic alumina coatings formed on aluminum substrate. By modulating the anodizing potential the porosity along with other properties of the coating were optimized. A coating of minimum porosity and maximum hardness and adhesion is required for corrosion protection. It would be appropriate to practically measure the corrosion resistance of this coating and its superiority over the un-optimized coatings should be practically demonstrated, this would be the second future work.

# Abstract

Alumina, because of its excellent combination of physical, chemical and mechanical properties, is considered as an important coating material for electronic and electrical devices, automobile and machinery, thermal engineering, energy, cutting tools, orthopaedic implants, etc. The high tritium permeation reduction factor of alumina makes it a potential candidate for their use as tritium permeation barrier for Test Blanket Modules (TBMs) of fusion reactor.

In this work, alumina coatings were formed by two different approaches. In the first approach, alumina coatings were developed for TBM related applications by thermal oxidation of the aluminum electrochemically obtained on T91 steel from $AlCl_3$-1-ethyl-3-methyl-imidazolium chloride ionic liquid. The so formed alumina coatings were studied for their crystalline phase, chemical composition and adhesion. Before converting aluminum to alumina the effect of bath purity, substrate types and their pre-treatments, and bath agitation on the characteristics and properties of aluminum coatings was established. It was established that by means of a simple chemical treatment low purity ionic liquids can be efficiently used for electroplating work. The alumina coatings formed by two-stage thermal oxidation of electrodeposited aluminum showed the formation of amorphous alumina having adhesive strength better than 20N. In the second approach, alumina coatings were developed for improving the corrosion behaviour of aluminum, by anodizing aluminum in 10% oxalic acid and mixtures of oxalic acid and citric acid. The anodic alumina coatings formed on aluminum substrate did not show the formation of crystalline phase. The anodic coatings showed oxygen concentration greater than that of the stoichiometric alumina. Further, the thickness, roughness and porosity of the coatings increased significantly on increasing the potential during anodization. By analysis of acoustic emission signal and optical microscopy imaging of scratch track during scratch testing it could be confirmed that the coatings formed at higher anodizing potentials had inferior adhesive strength. Hardness, wear resistance and electrical resistivity of the coatings were found to improve as the potential during anodizing was increased.

# Chapter-1

# Introduction

## 1.1 Background

Alumina occurs in nature in the form of minerals such as corundum ($Al_2O_3$), diaspore ($Al_2O_3{\cdot}H_2O$), gibbsite ($Al_2O_3{\cdot}3H_2O$) and bauxite etc. [1]. The history of alumina dates back to the age of ancient Sumerians, Greeks and Romans who used it for medicinal and other purposes in the form of potassium aluminum disulphate alum ($KAl(SO_4)_2{\cdot}12H_2O$) [1]. The industrial application of alumina was started in 1887 when the Austrian chemist Carl Joseph Bayer developed a method for commercial production of alumina from the impure bauxite mineral [2]. This method is popularly known as the Bayer process. The use of alumina in the form of coating was started in 1973 by tooling companies as a thermal barrier coating [3]. Since then alumina has gained a huge popularity as a versatile engineering ceramic material for tonnage to nanoscale applications.

## 1.2 Characteristics, properties and applications of alumina

Alumina is aluminum and oxygen based covalent ceramic that can be formed in different types of crystal structures viz. hexagonal, orthorhombic, tetragonal, monoclinic and cubic. The thermodynamically stable phase is $\alpha$-$Al_2O_3$ which has trigonal or hexagonal crystal structure similar to that of the corundum [4]. The widely known $\gamma$-$Al_2O_3$ is metastable and has cubic crystal structure [5]. The other metastable phases are $\theta$, $\kappa$, $\eta$ and $\delta$-$Al_2O_3$ [4].

Alumina exhibits excellent physical, mechanical and chemical properties including high melting temperature, high hardness [6], excellent wear resistance [6], high strength and stiffness [6], superior chemical and thermal stability [7], moderately high thermal conductivity [7], very high electrical resistivity [7], excellent dielectric strength [7] and optical properties [5]. It may be noted that the different polymorphs of alumina exhibit a vast difference in properties therefore, for a given application the selection of an appropriate phase is desirable. For example, among the $\gamma$, $\eta$, $\theta$, $\delta$, $k$ and $\alpha$ polymorphs of alumina $\alpha$ and $\kappa$ polymorphs are better suited as wear and abrasion resistant materials because of their higher hardness and thermal stability [4]. Similarly, $\gamma$ and $\theta$ polymorphs are useful for catalytic applications [4]. The amorphous alumina due to its higher band gap and dielectric constant than silica has been considered as a better candidate material for dielectric applications [8].

Because of its excellent properties alumina is considered as a very important engineering material finding applications in electronic, electrical, automobile and machinery, thermal engineering, energy, cutting tools, orthopaedic and dental implants etc. In electronic devices alumina is used as a substrate for microwave and high power radio frequency (RF) circuits and also for making sensors and multichip modules [7]. Alumina is also used for making capacitors and resistors for electronic circuits. The electrical engineering applications of alumina are focused mainly on its use as high voltage electrical insulators [9]. In automobile engines alumina is used as exhaust port liners and cylinder and piston liners [10]; whereas alumina is used as a diffusion barrier between the bond coat and construction material of gas turbine blades, for increasing the life of the blades [11]. The ultrafine powders of alumina in combination with water are of great concern for using them as a nanofluid for air-cooled heat exchangers [12]. The energy applications are based on the development of nanoporous alumina templates for micro-solid oxide fuel cells [13]. Alumina strengthened by zirconium oxide, titanium carbide and titanium nitride is useful for making tools for machining of cast iron, steel and nonferrous metals and alloys [14]. Mainly because of low friction, low wear rate, high resistance against scratch and indentation damage and excellent bio-compatibility, alumina is used as medical prosthetic devices in the form of total hip arthroplasties [15]. Moreover, alumina ceramic is also used as crown and bridge frameworks for dental implants [16].

Similar to bulk alumina, coatings of alumina are also considered as a very important engineering material. Alumina coatings show excellent photoluminescence [17,18], optical [19], corrosion [20,21], mechanical [22] and tribological [22,23] properties. They find numerous applications such as wear, abrasion and corrosion resistant layers on various components [24,25], fabrication of capacitive sensors [26] and films for optical and optoelectronic devices [27]. Also, the alumina layers formed by thermal oxidation of the aluminum coatings formed on ferritic-martensitic steel have been considered as a potential candidate for tritium permeation barrier for fusion reactors. Alumina coatings can be formed by various techniques including chemical vapour deposition (CVD) [28], metal organic chemical vapour deposition (MOCVD) [29], plasma enhanced chemical vapour deposition (PECVD) [30], laser assisted CVD (LACVD) [31], atomic layer deposition (ALD) [32], magnetron sputtering [33], pulsed laser deposition (PLD) [4], electron beam evaporation [34], cathodic arc [35], thermal spray [36], anodization [37], sol-gel [38], and thermal oxidation [39] methods.

For the past several years, alumina coatings have been formed on aluminized ferritic-martensitic steel surfaces, making them suitable for potential use as a tritium barrier for test blanket modules (TBMs) of fusion reactors [40,41]. Among the various ceramic coatings studied so far alumina has been accepted unanimously for this purpose since it shows the highest resistance for tritium permeation and also possess optimum resistance for corrosion in liquid PbLi, the latter is being proposed as a coolant for Indian TBM. There have been identified several processes including pack aluminizing, hot dip aluminizing and electrochemical methods to form alumina coatings for tritium permeation barrier applications [39–41]. The electrochemical method consists of two independent processes: first, the formation of aluminum coatings of suitable thicknesses by electrodeposition in ionic liquids and second, annealing the coatings in a controlled atmosphere so that the aluminum gets converted to the layers of iron-aluminide and alumina. There has been reported several studies on this subject [39,41,42]. However, there is not sufficient work available on the adhesion evaluation of the aluminide/alumina coatings formed by this method. For successful applications of alumina coatings for fusion reactor or other applications it must be mechanically strong and should possess adequate adhesive strength. Further, although there have been reported numerous studies on the formation of aluminum coatings from various types of ionic liquids [43–45], still the effect of purity of the ionic salts used for preparing the bath, bath agitation and substrate types on the properties of aluminum coatings have not been explored properly.

Anodization is considered as a very powerful technique to form oxide coatings of metals and alloys. In the case of aluminum, there have been reported numerous studies on the anodization behaviour of aluminum and the properties of alumina coatings so formed [46–48). The alumina coatings formed by anodization are known to improve the corrosion resistance and mechanical properties of aluminum. However, the alumina coatings formed by this technique are normally porous and so an expensive sealing treatment is required to close the pores and make the coating suitable for corrosion protection applications [49]. The porosity of anodic coating is dependent on the anodizing conditions including electrolyte used, potential applied between cathode and anode and temperature of the bath. Among these parameters anodizing potential has the strongest effect on porosity, and the coatings obtained at a higher potential are porous due to electric-field-assisted dissolution of the oxide [50]. Also, the coatings obtained at a higher potential are relatively hard. Therefore, anodizing potential needs to be optimized in such a way that a coating of relatively low porosity and higher hardness is formed. However, these aspects have not been covered in literature at a greater length [51]. Further, for corrosion protection applications the coating must be adequately resistant to indentation and scratch damages. In this context the scratch test can provide valuable information e.g. the critical load of cohesive and adhesive failure of the coating can be measured by scratch testing. Vojkuvka et al. [52] made extensive use of nanoindentation and scratch tests augmented with field emission electron microscopy (FE-SEM) image analysis to compare the mechanical behavior of nanoporous anodic alumina coatings obtained from three different acidic electrolytes. They came out with an interesting finding that the anodic alumina coatings obtained using phosphoric acid were able to deform under nanoindentation and scratch tests without breaking up, suggesting their potential applications in nanotechnology [52]. They reported that the anodic oxide coatings formed in oxalic acid and sulphuric acid solutions were brittle and showed comparable mechanical behavior [52]. But in the work of Vojkuvka et al. [52] the maximum applied load during scratch test was limited to 450 mN and they have not gone into the aspect of the adhesion of anodic oxide coating with the underlying substrate. Riddar et al. [53] reported the effect of aluminum microstructure and distribution of silicon particles therein on the scratch behavior of anodic aluminum oxide coatings. They anodized the aluminum cylinders obtained by sand casting; permanent mold casting; extrusion and high pressure die casting methods, in sulphuric acid electrolyte [53]. They showed that depending upon the manufacturing method of aluminum substrate, the anodic oxide coating behaved differently during scratch test [53]. Similarly, Malayoglu et al. [54] compared scratch behavior of the oxide coatings produced by plasma electrolytic oxidation and hard-anodizing methods using sulphuric acid electrolyte on 6082 aluminum alloy (Al-Si-Mg-Mn alloy). With the help of scratch adhesion test they found out that the coatings produced by plasma electrolytic oxidation gives better adhesion values

[54]. However so far, the effect of anodizing potential on the scratch behavior of anodic oxide coating formed on aluminum has not been reported. Anodizing potential is a very important parameter as it directly influences the structural properties of the coating by self-ordering of the pores and changes in the porosity and pore size [55,56]. Also, for obtaining practically useful information about the mechanical integrity of the coatings it is required to carry out scratch tests at a sufficiently high load.

## 1.3 Objectives of the present research

Therefore, giving due considerations to the gap areas prevailing in literature the objectives of the present study are as follows.

- The electrochemical formation of aluminum coatings on copper, mild steel and Fe9Cr1Mo steel substrates using Aluminum chloride ($AlCl_3$)-1-ethyl-3-methyl-imidazolium chloride (EMIC) ionic liquid bath. During electrodeposition studies focus was given to explore the effect of electrolyte purity, substrate types and their pre-treatments, current density and bath agitation on the characteristics and properties of aluminum coatings. The selection of chloroaluminate type ionic liquid bath for electrodeposition was based on their advantages including high aluminum concentration, low viscosity, high electrochemical stability and higher deposition rate [57].
- Establish the cathode current efficiency during aluminum electrodeposition, and crystal structure, chemical composition, thickness, morphology, topography and adhesive strength of the so formed aluminum coatings.

- Convert the so obtained aluminum on Fe9Cr1Mo steel to alumina layers by thermal oxidation, and study the crystal structure, chemical composition and adhesion of the oxidized coatings.
- Anodize aluminum in oxalic acid and mixtures of oxalic acid and citric acid. Characterize the so formed alumina coatings with respect to chemical composition, morphology, porosity, hardness, adhesive strength and wear resistance. Optimize the processing conditions so that alumina coatings having a better combination of these properties are formed on aluminum substrate. The selection of oxalic acid for anodization experiments was based on the fact that in this medium the so obtained coatings are relatively hard, hence they are better suited as a protective coating.

# Chapter-2

## Literature Review

As described in Chapter-1, alumina coatings are considered as a very important engineering material for development of numerous devices and finished components. Alumina coatings can be formed by several techniques including chemical vapour deposition (CVD), atomic layer deposition (ALD), physical vapour deposition (PVD), sol-gel and oxidation methods. The CVD technique can be further divided into thermal CVD, metal organic CVD (MOCVD), plasma enhanced CVD (PECVD) and laser assisted CVD (LACVD). Similarly, the PVD techniques may be classified into magnetron sputtering, pulsed laser deposition (PLD), electron beam evaporation, vacuum arc or cathodic arc deposition and plasma spray deposition. The oxidation methods can also be classified as anodic oxidation and high temperature air oxidation. Anodic oxidation may be further subdivided into anodizing and plasma electrolytic oxidation methods. The various methods of alumina coating formation along with their subdivisions are depicted in the flow diagram shown in Fig. 2.1.

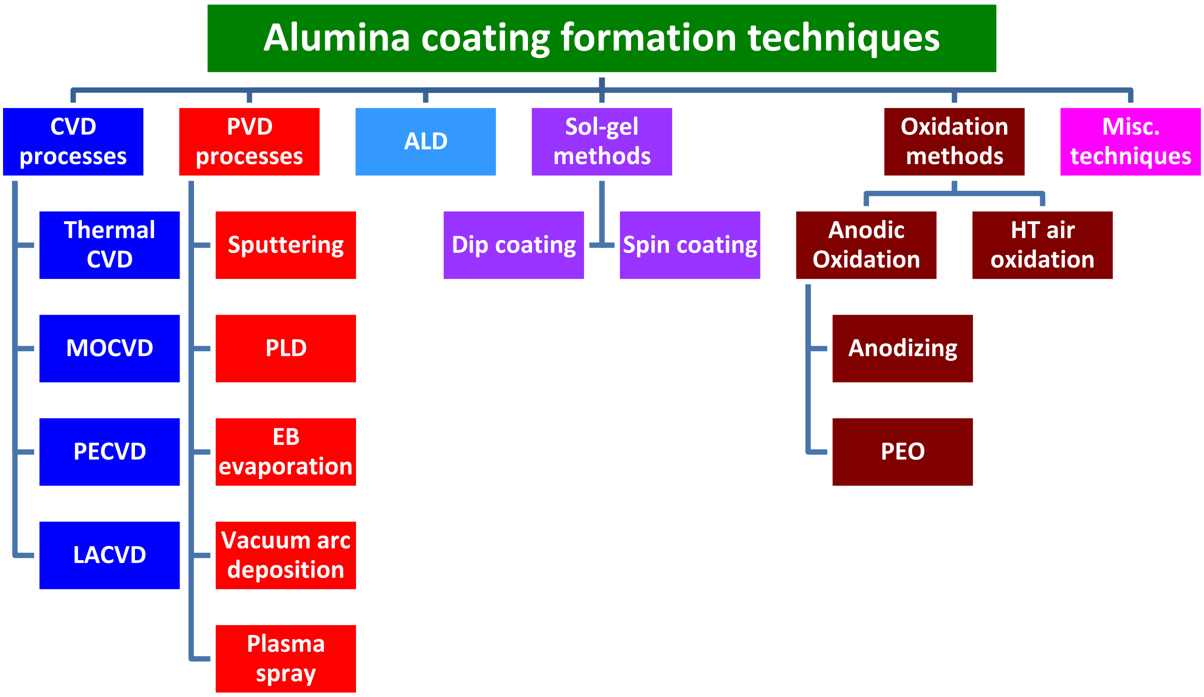

**Fig. 2.1** Various techniques of alumina coating formation.

In the following sections, a review on alumina coating formation techniques along with the main outcome of the studies reported on characteristics and properties of alumina coatings is given.

## 2.1 Alumina coating formation techniques

In this section, details of the alumina coating formation techniques, including main findings of the reported results are provided.

### 2.1.1 CVD methods

In this section, working principles of the commonly used CVD techniques namely, thermal CVD, metal organic CVD, plasma enhanced CVD and laser assisted CVD are briefed. Also, some of the important results reported on alumina coating formation using these techniques are highlighted.

### *Thermal CVD*

Using chemical vapour deposition technique a solid film is deposited on a heated surface after chemical reactions of two or more different vapors. In conventional or thermal CVD, high temperature (exceeding 900 °C) is required to meet the activation energy desired for the occurrence of chemical reactions [58]. A typical CVD system consists of the following components: the reactant supply system, the reactor and the exhaust [58]. Chamber pressure, reactor geometry, flow rate of vapours and substrate temperature are the main parameters that have direct influence on the characteristics and properties of the coatings.

Muller et al. [28] formed $\alpha$-$Al_2O_3$ coatings by CVD technique at 1050 °C from a feed gas mixture of $AlCl_3$, $H_2$ and $CO_2$ on a TiN coated nickel based super alloy substrate, for potential use of the coating as a diffusion barrier between the alloy substrate and the top NiCoCrAlY protective coating. The TiN layer was supposed to act as an inhibitor for alumina whiskers formation. Annealing tests conducted at 1100 °C for 100 h reportedly showed that a 3 μm thick layer of α-$Al_2O_3$ was very effective to prevent the diffusion of top NiCoCrAlY layer into the alloy substrate.

Larsson and Ruppi [59] studied the microstructure and wear behaviour of the $\gamma$-$Al_2O_3$ coatings deposited on TiN and Ti(C,N) pre-coated cemented carbide substrates at 800 °C by CVD technique using a gas mixture of $AlCl_3$, $CO_2$, $H_2$ and $H_2S$. The crater wear resistance of the $\gamma$-$Al_2O_3$ coated tools was reported as better than that of the commercially available $\kappa$-$Al_2O_3$ coated tools, because of the favourable fine grained microstructure design of $\gamma$-$Al_2O_3$ coating.

Halvarsson and Vuorinen [60] found that the formation of a crystalline phase of alumina by CVD technique depends on the crystallographic details of the nucleating surface.

Experimentally, they showed that by introducing different types of interlayers e.g. TiC, TiN or Ti(C,N) before alumina deposition, two different polymorphs of alumina namely $\alpha$-$Al_2O_3$ and $\kappa$-$Al_2O_3$ can be obtained by CVD technique from a feed gas mixture of $AlCl_3$, $CO_2$ and $H_2$ under identical conditions. The amount of lattice misfit between the planes of nucleating surface and that of the alumina phase were reported as a controlling factor to promote the growth of a particular crystalline phase of $Al_2O_3$.

***Metal organic CVD***

MOCVD process employs organometallic compounds as precursors in combination with some reactants [58]. For alumina coating formation by this technique aluminum acetylacetonate and aluminum tri-isopropoxide vapours are generally used as precursors. Using this method, it is possible to form uniform coatings on simple as well as complex shape objects. Gas flow rate, chamber pressure, reactor geometry and substrate temperature are the key parameters of this method. The characteristics and properties of the coatings are easily controllable by varying the deposition parameters.

Li et al. [29] prepared amorphous alumina coatings on SS 316 by MOCVD technique, for its potential use as a tritium permeation barrier for fusion reactors, using sublimed aluminum acetylacetonate precursor and hydrogen gas mixed with water vapour, at a substrate temperature of 350 °C. They succeeded to obtain coatings without any pores or cracks. Deuterium permeation resistance was evaluated for this coated specimen and the deuterium permeability was found to be 51–60 times less than the same for uncoated SS 316 steel. The relatively low deuterium permeation resistance was correlated with the amorphous nature of the coating. The same group of authors studied [29] the influence of alumina coating microstructure on the deuterium permeation behaviour. Two different microstructures were obtained by opting different annealing temperatures of 700 °C and 900 °C, respectively. The coating annealed at 700 °C was amorphous and had homogeneous microstructure but when annealing was done at 900 °C the coating was found to consist of $\gamma$-alumina along with a network of $MnCr_2O_4$ phase. A permeation reduction factor of 65–139 at 600–700 °C was reportedly achieved for the coating annealed at 700 °C but the same was found to drop to 6–11 for the coating annealed at 900 °C. The network of $MnCr_2O_4$ spinel was believed to act as a short-cut path for deuterium diffusion in the case of coating annealed at 900 °C.

### *Plasma enhanced CVD*

The temperature required to form coatings by a thermally activated CVD technique can be lowered drastically by assisting the process by means of plasma [61]. This has manifold advantages, for example, various types of substrates can be used for deposition, and the control of dopant migration during growth of semiconductor grade films also becomes easier. In plasma enhanced CVD process the precursors which are in the form of vapours are fed into the plasma of inert gas like argon created by pulsating electric fields having frequency in the range of 50 kHz–13.5 MHz [61]. The electrons of the plasma collide with the precursor gas molecules and forms highly reactive species including free radicals and ions [61]. These reactive species form coatings at a low substrate temperature. Precursor flow rate and temperature, plasma power, frequency, distance between the electrodes and substrate temperature are some of the important parameters controlling the properties of the films.

Snyders et al. [30] studied the effect of $AlCl_3/O_2$ precursor ratio used during deposition on the crystal structure and morphology of the alumina coatings formed on silicon wafers. A very strong effect of precursor ratio on the crystallinity of the coatings was reported. The coatings showed a mixture of $\alpha$ and $\gamma$ phases of alumina for $AlCl_3/O_2$ ratio $\leq 0.5$ whereas pure $\alpha$ phase was reported for $0.5<AlCl_3/O_2$ ratio$<1.15$. When $AlCl_3/O_2$ ratio was greater than 1.15, only $\gamma$-$Al_2O_3$ was reported to form. The formation of different crystalline phases of alumina was attributed to the change in plasma characteristics as the precursor composition was altered. However, the coatings prepared by Synders et al. [30] were significantly porous because of diffusion of Cl atoms into the growing film. The diffused Cl atoms agglomerated to form $Cl_2$ bubbles inside the $Al_2O_3$ matrix to form the porous coating.

Konstantinidis et al. [62] used pulsed PECVD with different duty cycles to control chlorine concentration of the alumina films deposited on silicon wafer. On increasing the duty cycle from 62 to 91% the chlorine concentration of the film was successfully reduced to half. This could be done because of two factors: first, greater dissociation of $AlCl_3$ precursor in the plasma and second increased ion bombardment of growing film enhancing the desorption of Cl. Due to low Cl concentration the $Al_2O_3$ films obtained by Konstantinidis et al. [62] were denser and smoother than the same reported by Snyders et al. [30]. The higher duty cycle was also seen to have favourable effect on the formation of thermodynamically stable $\alpha$-$Al_2O_3$ rich films. This was believed to be due to the fact that a higher duty cycle generates a higher ratio of flux of bombarding ions to flux of depositing material species. This leads to enhanced ion bombardment of depositing species on the substrate surface thus increasing their mobility and that could promote the growth of $\alpha$-$Al_2O_3$ phase.

Jiang et al. [63] used high power PECVD system and $AlCl_3$ precursor to form α-$Al_2O_3$ films having very low Cl concentration. The high discharge power used during deposition could enable better precursor dissociation in plasma as well as intense ion bombardment of depositing species on substrate surface, leading to the formation of $\alpha$-$Al_2O_3$ having negligible Cl concentration. The different crystalline phases of alumina as observed by Jiang et al. [63], upon varying the discharge power, is in agreement with the observation made by Kyrylov et al. [64] who obtained crystalline alumina coatings on TZM substrate by bipolar pulsed PECVD technique. Kyrylov et al. [64] reported $\gamma$-$Al_2O_3$ at 0.7 W/cm$^2$, a mixture of $\alpha$ and $\gamma$

phases at 5.65 W/cm$^2$ and finally $\alpha$-$Al_2O_3$ at 9.05 W/cm$^2$ power density. Kyrylov et al. [64] reported similar phase change by increasing the substrate temperature from 500 to 620 °C. The maximum values of hardness and elastic modulus obtained by Jiang et al. [63] for alumina coatings were approximately 25 GPa and 380 GPa, respectively.

Ntsama-Etoundi [65] reported the deposition of alumina coatings on nickel based super alloys by microwave plasma enhanced chemical vapour deposition technique conducted in oxygen plasma with trimethylaluminium used as a precursor. The effect of microwave power, process chamber pressure, deposition temperature, and precursor flow rate on deposition rate and properties of the coating was studied. The rate of deposition of the coating was found to depend mainly on the precursor flow rate and it increased linearly as the precursor flow rate was increased. The obtained aluminum oxide films reportedly showed good electrical resistivity values of the order of $8\times10^{11}$–$4\times10^{12}$ Ωcm. The mass density and electrical resistivity of the films were reported to increase on increasing the temperature of deposition.

### *Laser assisted CVD*

This method can be grouped into thermal-laser CVD and photo-laser CVD techniques [58]. In thermal-laser CVD the temperature of the substrate is increased locally by selecting lasers of such a wavelength that the energy of the laser is not absorbed by the precursor gas molecules and it is only used for heating the substrate [58]. But, in the case of photo-laser CVD the laser interacts with the precursor gas molecules to form reactive species that react to form the coating [58]. In this case substrate heating is not required.

You et al. [31] obtained alumina films by laser assisted CVD technique on AlN substrate using a diode laser and aluminum acetylacetonate precursor. The effect of laser power, chamber pressure and deposition temperature on the crystal structure, surface morphology and deposition rate of the films were systematically studied. The formation of amorphous alumina was observed at 50 W, whereas crystalline alumina was reportedly formed at a power higher than 100 W. Besides crystal structure, surface morphology of the coatings were also found to depend on the laser power and the morphology turned to faceted granular structure from cauliflower structure on increasing the laser power. Also, a low chamber pressure could help to promote the growth of faceted grains. The deposition rate was found to decrease beyond 80 W power and 0.4 kPa pressure.

Kadokura et al. [66] studied the characteristics of alumina coatings formed by LACVD method on yttria-stabilized zirconia substrate, using aluminum tri-acetylacetonate precursor, $O_2$ gas and Nd:YAG laser. The formation of $\alpha$-$Al_2O_3$ was confirmed at temperature higher than 1100 $^\circ$C, and below this temperature the so formed coatings mainly consisted of $\gamma$-$Al_2O_3$ phase. A strong correlation between crystalline structure and morphology was established by Kadokura et al. [66] for two different crystalline phases of alumina, showing cone type and hexagonal facet type of structures for $\gamma$-$Al_2O_3$ and $\alpha$-$Al_2O_3$, respectively.

### 2.1.2 Atomic layer deposition (ALD)

The method of ALD may be treated as analogous to CVD technique but actually it differs in the way that the precursor gases enter the deposition chamber, widely known as viscous flow ALD reactor, and the nature and sequence of chemical reactions taking place during film nucleation and growth [67]. In CVD all the required precursors are present in the deposition chamber at a given time and they react themselves to form a film on the substrate surface. However in the case of ALD the precursors or reactants are rather fed into the reactor in the form of alternate pulses that lasts only for few seconds and the formation of a monolayer of the material is confirmed when reaction of substrate with all the needed precursors is completed [67]. Just because of self-limiting nature of the process atomic scale precision may be easily achieved during growth of the film [67]. For depositing alumina films by ALD method trimethylaluminum (TMA) and water are commonly used as precursors and, starting from TMA both the precursors are alternately fed into the reactor and nitrogen purging is done each time after completion of one precursor pulse [32]. When TMA is introduced into the reactor it reacts on the active native sites for example, hydroxide groups (OH), on the substrate surface to form methyl terminated aluminum. The subsequent reaction with water forms $Al_2O_3$ and the by-product gas ($CH_4$) are flushed out [68]. The reactions with TMA and water are repeated in a cyclic fashion to increase the thickness of the film. The main advantages of ALD are the capability of the process to produce highly uniform and flat films without any defects like pin holes etc. rendering its potential use in sophisticated electronic devices [67]. Further, substrate heating is not very critical for ALD and it is possible to form alumina coatings even at room temperature. Thus it opens the door to use variety of materials as a substrate. The disadvantage of this method is that the deposition rate is very slow and thus a large number of cycles are required to form a few nanometer thick films [68].

Groner et al. [32] formed $Al_2O_3$ films by ALD technique on variety of substrates including Si, Mo coated Si, Au, Co, Cr, Cu, Mo, Ni, NiFe, NiMn, Pt, PtMn, SS, W and ZnO, using TMA and water at 125–425 °C. The obtained films reportedly showed a dielectric constant of 7.6 and films as thin as 12 nm were highly effective to bring down the leakage current to less than 1 $nA/cm^2$ at an applied electric field of 2 MV/cm. The electrical properties of $Al_2O_3$ films formed on different substrates were reported to vary and the same was attributed to a large extent to the difference in reactivity of various metals/elements, presence or absence of native oxide layers of various thicknesses and compositions on different substrates, and substrate roughness.

Finch et al. [68] successfully demonstrated that the alumina coatings formed by ALD technique can be used in bio-micro electro mechanical systems (bio-MEMS). The purpose of such coatings is to act as a dielectric medium for preventing electrical shorting of bio-MEMS devices without altering the biological processes being measured. The $Al_2O_3$ films formed on borosilicate glass substrate reportedly showed normal cell proliferation behaviour (on human coronary artery smooth muscle cells) *in vitro* for 7 days confirming satisfactory biocompatibility.

Kim et al. [69] used ozone ($O_3$) in combination with TMA to form $Al_2O_3$ films on Si substrate by ALD technique and found that increasing the substrate temperature beyond 350 $^{\circ}$C did not result in decreased film growth rate, as is the case when $H_2O$ is used as a source of oxygen for $Al_2O_3$ formation by ALD; rather the growth rate was found to increase marginally. This difference was attributed to the temperature dependent dehydroxylation of $Al_2O_3$, decreasing the amount of deposited material, when TMA and $H_2O$ reactants were used to form the film. The increase in film growth rate with temperature, in the case of film formed by TMA and $O_3$ reactants, was reportedly due to decomposition of $O_3$ contributing to the film formation.

### 2.1.3 PVD methods

In this section, working principles of the commonly used PVD techniques namely, sputtering, pulsed laser deposition, electron beam evaporation, vacuum arc deposition and thermal spray deposition are briefed. Additionally, some of the key results reported on alumina coatings formed by using these techniques are highlighted in this section.

### *Sputtering*

In sputtering atoms from the surface of a material, also termed as target or cathode, are ejected by momentum transfer from high energy bombarding ions [70]. The process is done in a vacuum chamber where glow discharge plasma of a non-reactive gas for example, argon is created between the cathode and anode. The negatively charged cathode attracts with a greater force the heavier $Ar^+$ ions and this leads to ejection of atoms from the target material. The ejected materials get deposited on the substrate, kept at a certain distance in front of the target, and this process is named as non-reactive sputtering. However, if the ejected atoms of a target need to react with a reactive gas for example $O_2$, $N_2$, etc. so that a compound coating is formed the process is known as reactive sputtering. Further, using a definite arrangement of strong magnetic field lines on cathode it is possible to confine the movement of the electrons of plasma near cathode regions so that the electrons spend a large amount of time in plasma and better ionization is achieved [70]. If such a magnetic field is used the method becomes magnetron sputtering. Further, if an electrically insulative coating is to be formed from an insulative target, sputtering cannot be done using a direct current power source due to accumulation of positively charged particles on cathode/target surface and in that case a pulsed dc power or radio frequency power is used to sputter the target. Therefore, depending on the type of power source used, the sputtering may be called as dc, pulsed dc or rf sputtering. Moreover, if magnetic field is also present then the process becomes dc magnetron sputtering, pulsed dc magnetron sputtering or rf magnetron sputtering. In order to form alumina coatings by magnetron sputtering a disc shaped $Al_2O_3$ target is sputtered out in argon plasma either by pulse dc or rf power. The parameters of this process are power density of cathode, pulse frequency and duty cycle (if pulse dc/rf power is used), target-to-substrate distance, and substrate temperature and biasing.

Kohara et al. [33] formed $Al_2O_3$ coatings on pre-oxidized CrN coated cemented carbide tool steel and silicon wafers at 600–750 °C using pulsed dc reactive magnetron sputtering method. They reported that due to pre-oxidation of CrN, a layer mainly consisting of $\alpha$-$Cr_2O_3$ phase formed on top of the CrN coated cemented carbide tool steel substrate that could stabilize $\alpha$-$Al_2O_3$ at a relatively low temperature of 700-750 °C. It may be noted that $\alpha$-$Cr_2O_3$ has a corundum ($\alpha$-$Al_2O_3$) crystal structure. The role of this layer on the formation of $\alpha$-$Al_2O_3$ was clearly validated from the fact that the coating formed on silicon wafer in the same batch reportedly showed only weak XRD reflections of $\gamma$-$Al_2O_3$. Further, Kohara et al. [33] noticed a steep rise in hardness of $Al_2O_3$ coatings, from 14 GPa at 600 °C to 23 GPa at 750 °C, mainly because of the increased proportion of $\alpha$-$Al_2O_3$ in the coatings.

Kakati et al. [71] showed that using unbalanced magnetron under poisoned conditions it is possible to form metastable crystalline phases of alumina at a very low substrate temperature. They reported the formation of $\theta$ and $\gamma$ phases of alumina on bell metal substrate by rf magnetron sputtering at 80–120 °C. The alumina coatings were reportedly well adherent to bell metal and showed improved corrosion behaviour under different pH conditions revealed from the copper accelerated salt spray tests.

Wallin et al. [72] reported that using reactive high-power impulse magnetron sputtering (HiPIMS), a relatively dense $\alpha$-$Al_2O_3$ film can be formed on cemented-carbide and molybdenum substrates at temperature as low as 650 °C, with or without biasing the substrate. In contrast to conventional magnetron sputtering, HiPIMS employs high-power pulses to the target at a relatively low duty cycle. This generates highly ionized plasma having a broad energy distribution, but the average power consumed and target heating achieved are close to that of the conventional magnetron sputtering. Wallin et al. [72]

reported that at 575 °C the formation of $\gamma$-$Al_2O_3$ took place but there could not form any crystalline phase of $Al_2O_3$ at 500 °C or lower substrate temperature.

Schneider et al. [73] formed crystalline alumina films, consisting of $\theta$ and $\kappa$ phases, on stainless steel 316 coated silicon substrates by ionized magnetron sputtering at 370–430 °C. In this technique, the plasma discharge consisting of $Ar^+$ ions, O and sputtered Al species is further ionized by means of a separate power source so that the O and Al atoms also get converted into their respective ionic form. This way the ion flux is considerably increased, and by applying a negative bias potential of suitable magnitude to the substrate, the ion energy is also increased. The ion flux or ion current density can be further increased by increasing the amount of power applied to the discharge. The greater mobility of reactive species thus achieved leads to the formation of crystalline films on a moderately heated substrate. Schneider et al. [73] reported the formation of pure $\kappa$-$Al_2O_3$ at 3.5 $mAcm^{-2}$ ion current density, however beyond this value a mixture of $\theta$ and $\kappa$ alumina phases could form. The obtained alumina films were stoichiometric and the films were reported as hard as CVD deposited $\kappa$ alumina films.

### ***Pulsed laser deposition***

In pulsed laser deposition method, a short laser pulse (10 to 30 ns) is focused on a solid target, kept in vacuum or controlled atmosphere, so that the temperature of the spot is rapidly increased beyond the vaporization temperature [74]. This creates a plume of evaporated material in front of the target which is deposited as a coating on a substrate. Laser wavelength, spot size, pulse energy, pulse width, laser fluence, laser repetition rate, substrate temperature, chamber pressure and target-to-substrate distance, etc. are main parameters of the process. Best films in terms of properties are obtained by optimizing the deposition conditions. Usually, KrF excimer lasers and Nd:YAG solid state lasers are employed for depositing thin films by PLD method [74].

Boidin et al. [8] deposited alumina films by PLD technique on glass and silicon wafer without external heating of the substrate. The effect of argon gas pressure (used during deposition) on the growth rate, crystal structure, roughness and refractive index of the films was studied. For chamber pressure kept in the range of $10^{-6}$ to $10^{-2}$ mbar there could not be seen any effect on crystal structure of the film and it was reported as amorphous. However, chamber pressure had a definite role on growth rate of the film, and at pressure of the order of $10^{-6}$ to $10^{-4}$ mbar a growth rate of approximately 1.6 Å/s was reported whereas at $10^{-2}$ mbar a higher growth rate of 1.8 Å/s was obtained. The occurrence of low deposition rate at low pressure was attributed to the fact that the interaction between ablated plume and Ar gas leads to angular broadening of the plume hence the flux of ablated species reaching the substrate surface decreases leading to a low deposition rate [8]. Boidin et al. [8] reported a decrease in RMS roughness of the film with decreasing the working pressure and this could be due to the fact that because of less thermalization at low pressure the energy of depositing species is high on the substrate surface. This makes the adatoms more mobile on substrate surface and so a uniform film of low roughness was reportedly obtained. The refractive index of the alumina films formed at different pressures was reported as not to be very different.

Balakrishna et al. [5] deposited alumina films on silicon substrate at 973K by PLD method using a sintered $\alpha$-$Al_2O_3$ target. They studied the effect of oxygen partial pressure on the crystallinity, thickness, roughness and refractive indices of the films. The obtained films were reported as amorphous at 3.5 x $10^{-1}$ mbar oxygen partial pressure but, cubic $\gamma$-$Al_2O_3$ was formed in the oxygen partial pressure range of 3.5 x $10^{-2}$–2.5 x $10^{-5}$ mbar with best crystallinity observed at 3.5 x $10^{-3}$ mbar. The formation of crystalline films at low oxygen pressure was assigned to the higher energy of depositing species on the substrate surface due to low thermalization, as explained in the previous paragraph. The decrease of oxygen partial pressure was found to be helpful in the formation of relatively thick and dense films having low roughness and better refractive index values [5]. This was also correlated with the higher energy of depositing species hitting the substrate surface and therefore forming a uniform and denser film. Another work reported by Balakrishna et al. [75] showed that the substrate temperature plays a decisive role in the formation of crystalline or amorphous alumina films by PLD method and, at an optimized pressure of $3 \times 10^{-3}$ mbar crystalline films were reported to form at a temperature higher than 673K. The alumina films formed at higher substrate temperatures (>773K) reportedly possessed better values of nanohardness and refractive index due to the formation of a relatively dense microstructure. A different work reported by the same authors [4] established that the post deposition annealing of alumina up to 973K leads to the formation of $\gamma$-$Al_2O_3$. They further reported that by increasing the annealing temperature beyond 1073K $\theta$ and $\delta$ phases of alumina can be formed. The thermodynamically stable $\alpha$-$Al_2O_3$ could be obtained by carrying out annealing at temperature higher than 1573K [4]. In a recent study, Balakrishna et al. [76] showed that the type of crystalline phase of alumina formed by PLD depends to a large extent on the crystal structure of the substrate employed, as the growing film has a tendency to adopt the crystal structure of the substrate. This way, they succeeded to obtain $\gamma$-$Al_2O_3$ (400) on SrTiO3 (100), $\alpha$-$Al_2O_3$ (024) on $\alpha$-$Al_2O_3$ $(1\bar{1}02)$, $\alpha$-$Al_2O_3$ (006) on $\alpha$-$Al_2O_3$ (0001) and $\alpha$-$Al_2O_3$ (006) on MgO (100) at $3.5 \times 10^{-3}$ mbar and 700 °C [76].

### *Electron beam evaporation*

Electron beam evaporation is a coating forming technique in which a target (chemically same as the coating) is bombarded with an electron beam from an electron beam source [77].

The evaporated discharge gets deposited in the form of a thin film on a substrate kept in the deposition chamber in front of the target. This method has the merit of higher deposition rate, suitability of the process for obtaining coating on a range of materials (materials having both low and high melting temperatures are suitable), high material utilization efficiency and very low level of film contamination, etc. [77].

Nayar et al. [34] prepared alumina films on silica substrate by electron beam evaporation technique. Crystallinity, optical properties and nanohardness were studied for as- deposited films and the films subjected to annealing at 400–1130 °C. The as-deposited films were reportedly amorphous whereas the films annealed up to 950 °C were found be a mixture of $\gamma$ and $\delta$ alumina phases. When annealing temperature was increased up to 1130 °C, three phases namely $\gamma$, $\delta$ and $\theta$ were reported to co-exist but the stable $\alpha$-$Al_2O_3$ could not form. The absence of $\alpha$-$Al_2O_3$ even at 1130 °C was attributed to the suppression of $\gamma + \delta \rightarrow \alpha$ transformation reaction due to silica which was used as the substrate [34]. Alumina films under annealed conditions reportedly showed a relatively high value of refractive index and low absorbance in comparison to the as-deposited films ($n$: 1.666 for as-prepared and 1.778 for annealed films). The hardness of annealed films was better than that of the as-deposited films (6–8 GPa for as-deposited and 11–12 GPa for annealed films were reported). This was reportedly assigned to the amorphous to crystalline phase transformation of alumina [34].

He et al. [78] deposited alumina films on glass substrate by electron beam evaporation method but made an important change that instead of directing the flux of depositing species towards the substrate at normal incidence, as is done normally, the flux was directed to the substrate at various angles (0° to 80°). This could result in the formation of films having various levels of porosity because of the self-shadowing effect that reportedly becomes predominant at higher inclination angles [78]. As the inclination angle was increased from 0°

to 80° the refractive indices of the films deposited at various substrate temperatures (300 to 1073 K) were found to decrease by more than 10% [78]. On the other hand, transmittance of the film was found to increase as the inclination angle was increased and at 80° the transmittance of the film was reported as maximum and equal to that of the glass substrate, indicating the formation of anti-reflection films [78]. The porosity of the films formed at 60° and 80° was reported to increase with temperature, in contrast to the porosity of the films formed below 60° that showed a reverse trend. This was assigned to the formation of a large number of defects such as pin holes and voids etc. in the cases of films grown at inclination angles greater than 60° [78].

Reddy et al. [79] successfully converted the amorphous alumina grown by electron beam evaporation technique on titanium substrate to crystalline and nanostructured alumina by post deposition annealing. The films annealed in air in the temperature range of 500–800 °C reportedly showed the formation of a mixture of $\alpha$, $\delta$, $\theta$, $\varepsilon$ and $\chi$ phases of alumina. Interestingly, the films annealed at 700 °C showed the formation of tripod type of structure whereas annealing at 800 °C resulted in the formation of alumina nano-rods [79]. The formation of tripod or nano-rod structure was attributed to the morphology evolution of titanium substrate due to $TiO_2$ formation during annealing, and also the cracking of alumina films due to difference in coefficient of thermal expansion between $Al_2O_3$ and $TiO_2$ that leads to ingress of oxygen into alumina during annealing [79].

### ***Vacuum arc deposition***

In this method, an electric discharge is created in front of a water cooled cathode by means of self focused and localized arcs [80]. In contrast to sputtering or electron beam evaporation where the discharge is electrically neutral, the arc discharge is mainly ionic in nature [80]. Therefore, it is possible to tailor coatings of desired properties for example, density, hardness and adhesion by controlling the energy of the discharge [80]. For depositing alumina coatings by cathodic arc technique, the cathode used is aluminum and so the discharge consists of Al ions which are converted to $Al_2O_3$ by introducing oxygen gas. It may be noted that due to extremely localized heating of cathode the cathodic arc produces macroparticles or droplets of the cathode material. These macroparticles are usually getting deposited on the coating and are considered as defects [80]. To remove or trap such particles, electromagnetic filters are used and therefore this method is also known as filtered cathodic arc deposition. Working pressure, arc current and voltage, substrate temperature and biasing potential are the main parameters of this method.

Brill et al. [35] formed alumina coatings on graphite, inconel, vanadium and palladium substrates by filtered vacuum arc technique. An effort was made by them to bring down the substrate temperature required for $\alpha$-$Al_2O_3$ formation by applying negative bias potential to the substrate. For deposition conducted on unbiased substrate a mixture of amorphous and $\alpha$-$Al_2O_3$ was reportedly formed at 720 °C whereas, a mixture of $\gamma$-$Al_2O_3$ and $\alpha$-$Al_2O_3$ could be formed at an increased temperature of 835 °C. The films grown at 650 °C and -300V biasing potential consisted of pure $\alpha$-$Al_2O_3$. This clearly shows the effectiveness of bias potential for depositing crystalline film at lower substrate temperature. This was essentially due to the fact that applying a negative biasing potential to the substrate leads to bombardment of depositing species by positive ions drawn towards the substrate. This actually increases the kinetic energy of adatoms and hence the formation of a thermodynamically stable phase becomes easier. The deuterium permeability tests conducted at 400 °C on alumina coated palladium substrates reportedly showed a deuterium permeation reduction factor of around 400. However, in contrast to the results reported by Brill et al. [35] on crystallinity of alumina coatings, Tay et al. [81] did not find any effect of bias potential on crystallinity of the alumina coatings formed by cathodic arc method and the coatings remained amorphous despite the use of bias potential during film growth. But, the amount bias potential used by Tay et al. [81] was much less and the same was in the range of 60–140 V. Thus the relatively low energy of bombarding ions due to lower biasing potentials did not help to form crystalline alumina coatings. Further, Tay et al. [81] noticed that the refractive index of alumina coatings increased on increasing the biasing potential due to improved packing density of the coatings. Similarly, the hardness, modulus of elasticity and refractive index values of the coatings formed at higher substrate temperature were reportedly increased due to densification of the coatings.

Choong et al. [82] used a novel ring technique for introducing oxygen gas during deposition of alumina coatings by off-plane double bend filtered cathodic arc method. This arrangement could enable better ionization of oxygen thereby lowered the amount of oxygen needed for stoichiometric alumina formation. Because of low oxygen partial pressure used during deposition, the coating growth rate was reportedly much higher due to increase in mean free path. The optimum deposition rate reported by Choong et al. [82] was 3.25 nm/s which is nearly double than that reported by Brill et al. [35].

Zhao et al. [83] studied the influence of oxygen partial pressure used during alumina film deposition by off-plane double bend filtered cathodic arc method on chemical composition, hardness and Young's modulus, and residual stresses of the films. They showed that the obtained films were oxygen rich when a higher concentration of oxygen was used and, at an oxygen partial pressure of $6 \times 10^{-4}$ Torr stoichiometric films were reportedly formed. Similarly, the values of hardness and Young's modulus were reportedly found to increase on increasing the oxygen partial pressure. The compressive residual stresses were detected in the films and its magnitude decreased with increasing the oxygen partial pressure. More importantly, the coefficient of friction for the stoichiometric alumina films formed by Zhao et al. [83] on silicon substrate was less than 0.08 against DLC (diamond like carbon) balls whereas such films when formed on quartz showed optical transmittance comparable to that of the substrate, in the wavelength range of 200–900 nm. These results clearly show that the alumina coatings formed by filtered cathodic arc method are suitable for their use as wear resistant and optical coatings.

### *Thermal spray deposition*

In thermal spray deposition method, metallic, ceramic or polymeric materials in the form of powder, wire, or rod are fed to a torch in which they are heated to a temperature higher than their melting point [84]. The molten material in accelerated jet form is then projected on a substrate to be coated. Upon impingement on substrate surface the molten droplets get solidified in the form of overlapping lamellae and a coating is resulted [84]. The thickness of the coating is normally increased by increasing the number of passes. Depending on the type of heating method adopted, thermal spray processes are known as flame spray, plasma spray, high velocity oxy-fuel spray and detonation gun spray techniques [84]. Using thermal spray deposition technique adherent coatings of very high hardness finding applications as wear and abrasion resistant layers can be easily obtained.

Sarikaya [36] studied the effect of spraying distance, substrate temperature, coating thickness and SS 304L substrate roughness on the microstructure and hardness of alumina coatings formed by atmospheric plasma spray (thermal plasma created by Ar and $H_2$ gases) deposition using 95% $Al_2O_3$ powders. An increase in substrate roughness (3.28 to 5.74 µm) and coating thickness (100 to 600 µm) reportedly increased the porosity (4 to 9%) and roughness of the coatings (4 to 10 µm) therefore the hardness was decreased. Spray distance of 12 cm was reported as optimum for obtaining coatings having highest hardness (950 HV) and lowest surface roughness (<7 µm) and porosity (approx. 8%), due to maximum temperature attained by the sprayed particles hitting the substrate surface. An increase in substrate temperature (up to 500 °C) increased the mobility of depositing species on the substrate surface leading to decrease in surface roughness and porosity of the coatings that could in turn increase the hardness of the coatings (maximum reported hardness in their work was approx. 1200 HV).

Singh et al. [85] formed conventional and nanocrystalline alumina coatings on SS 304L substrates by atmospheric plasma deposition technique using micro and nano sized powders of alumina. Microstructure, sliding wear and $SiO_2$-$Al_2O_3$ slurry erosion behaviour of the coatings were compared. The coatings prepared using micron sized alumina powders reportedly showed the formation of micron sized interconnected lamellars. However, the microstructure of nanostructured coatings revealed smaller lamellars and presence of few partially melted and agglomerated particles. The wear rate and coefficient of friction were reported as lower for nanostructured coatings as compared to the conventional coatings. The two phase microstructure observed for nanostructured coating and presence of very fine particles (generated during wear test) between the two counter parts during wear test were identified as the underlying causes for low wear rate of this coating. Similarly, the slurry erosion resistance was found to be better for nanostructured alumina coating compared to the conventional coating.

Gao et al. [86] replaced the traditionally used externally-fed powder system by a novel designed internally-fed powder technique during plasma spray deposition of alumina coatings. In this technique instead of injecting the source powder directly into plasma flame just outside the nozzle, as is done in the case of conventional plasma spray deposition method, the powder was introduced between cathode and anode of the spray gun. Using 2.5 kW internally-fed plasma spray method, the spraying efficiency was reportedly matched with that of the 40 kW externally-fed plasma spray technique. Further, at constant power the use of high energy plasma, by either increasing current or voltage, could reportedly increase the hardness of the coating (900 to 1500 kg/mm$^2$) because of the formation of a less porous microstructure. However, energy of the plasma was more effectively increased by increasing voltage instead of increasing current. It may be noted that in the work of Gao et al. [86] the formation of a mixture of $\alpha$ and $\gamma$ alumina phases was reported but their powder consisted of pure $\alpha$-$Al_2O_3$. This was reportedly due to higher degree of under cooling of alumina droplets on substrate surface, enhancing the probability of $\gamma$-$Al_2O_3$ nucleation.

Turunen et al. [87] prepared alumina coatings on steel plates by high velocity oxy-fuel (HVOF) thermal spray process using two different fuel gases namely, propylene ($C_3H_6$) and $H_2$. The effect of the type of fuel gases used along with its flow rate and spray distance or standoff distance on flame temperature and velocity of flame was established. Propylene was reportedly found to be a better fuel gas than hydrogen since it could help in achieving higher flame temperature. Alumina coatings were prepared using alumina feedstock powder (99.3%) and the effect of various parameters such as fuel gas/oxygen ratio, total gas flow rate, standoff distance, thickness per pass and total coating thickness on the microstructure, and mechanical and electrical properties of the coatings was studied. Using HVOF thermal spray method alumina coatings were reportedly formed of various passes or layers of various thicknesses as revealed from microscopic examination of the cross-section of the coatings, this type of structure is not normally obtained by APS technique. The pores in the coatings were found be present between the two adjacent passes. By increasing the $C_3H_6/O_2$ ratio to 0.28 the temperature and velocity of the flame were reported as maximum (2390 ± 251°C and 755 ± 120 m/s, respectively) and this could result in the formation of alumina coatings having lowest porosity and highest mass density (3.72 g/cm$^3$). The thermal conductivity of the coating was reported as highest (4.41 W/mK) when the thickness per pass was increased to its highest value of 22.6 µm. This way the porosity was significantly lowered as the number of passes was decreased. Similar effect was observed on the dielectric constant/strength of the coatings and the value of dielectric constant was highest (8.2) when the number of passes and hence the porosity was lowest [87]. Lastly, coatings having low wear rate were reportedly obtained by selecting higher fuel gas/oxygen ratio, higher coating thickness per pass, higher total gas flow rate and lower standoff distance. The effect of all such parameters was realized in maximization of the fame temperature and velocity.

Saravanan et al. [88] used detonation gun thermal spray method with liquefied petroleum gas (LPG) employed as a fuel gas. This technique is not much different than the just above described HVOF thermal spray technique, for depositing alumina coatings on steel substrates. LPG when ignited in oxygen created explosion or detonation that released enormous amount of heat to melt the injected alumina powders. Saravanan et al. [88] demonstrated that a combination of the following process parameters: lower spray distance, higher carrier gas flow rate and higher fuel/oxygen ratio lead to the formation of alumina coatings of low porosity and high hardness because of higher velocity of the molten particles on substrate surface. Crystalline alumina coatings of hardness as high as 1363 HV were reportedly formed by choosing fuel to oxygen ratio of 1:3.6, carrier gas flow rate of 30 div. and spray distance of 145 mm.

### 2.1.4 Anodization and plasma electrolytic oxidation techniques

Anodization is a classical electrochemical method of forming metal oxide coatings. In this technique, the oxide coating of a metal is formed by considering the selected metal as anode in a suitable electrolytic solution. The cathode is normally a different metal. Anodization can be done in both potentiostatic as well as galvanostatic mode. The characteristics and properties of the resulting coatings can be controlled by optimizing the associated process parameters like type of bath and its concentration used for anodization, applied potential/current, bath temperature, bath agitation, anodization time, opting for external variables like magnetic field, etc. The advantages of this method are simplicity and cost effectiveness as no expensive equipments are required. Also, it is much easy to form coating on a complex shaped metal. The disadvantage of this method is that the obtained coatings are highly porous in nature which is not always required. Besides, the crystalline coatings are generally produced only at a very high potential/current for which cooling arrangement for anodizing bath becomes essential. Also, it is not possible to form the same coating on different types of metallic substrates. Further, non conducting materials cannot be used to form the coatings. Moreover, in several cases it is nearly impossible to increase the coating thickness beyond a certain value if an impervious oxide layer is formed on the outer surface of the coating.

For the past several decades, oxide coatings of metals like Al [37], Ti [89], Nb [90], Ta [91], Mg [92], Zr [93] and alloys of Al [94], Ti [89] and Mg [95] have been extensively formed by anodization technique. However, this technique is much popular for Al and Ti.

By anodization of aluminum, alumina ($Al_2O_3$) coatings as well as freestanding alumina membranes can be formed. Anodized aluminum/aluminum alloys find numerous uses including cookware, door frames for houses, spacecraft components [96], templates for growing nanowires for electronic, optoelectronic and magnetic devices [97], solar cells [98], sensors [99], separator for Li ion batteries [100] and membranes for biomedical devices [101], because of the combination of several outstanding properties including light weight, stronger surface, periodic arrangement of vertically aligned pores in the oxide under certain experimental conditions [102], improved corrosion resistance [94], high refractive index [103], optimum reflectance and transmittance [104] in visible spectrum and attractive visual appearance. For anodization of aluminum several conventional acidic baths like sulphuric acid [94], phosphoric acid [46], oxalic acid [47], chromic acid [48], nitric acid [105], sulfamic acid [17] and mixtures of these acids [106,107] have been extensively explored. During past five years, several new organic baths for example squaric acid [108], malonic acid [109], malic acid [110], selenic acid [111], oxocarbon acid [112], phosphonic acid [113], etidronic acid [114] and pyroposphoric acid [115] have been successfully designed to carry out the anodization of aluminum. In the subsequent paragraphs major findings of some of the excellent works reported in literature on aluminum anodization are summarized.

Ghrib et al. [37] studied the photoluminescence and optical properties of anodic alumina films formed in sulphuric acid. They reported significant improvement in refractive index, reflectance and luminescence values and a substantial decrease in optical losses for the films subjected to annealing at 650 °C, due to structural densification happened to the films. However, the crystallinity of the films was found to deteriorate due an amorphous $Al_2O_3$ layer formed on top of the oxide coating.

Chen et al. [100] prepared 60 μm thick through-hole anodic alumina membranes by a two-step anodization technique in 0.3M oxalic acid, for potential use of the membrane as a separator in Li-ion batteries. The characteristics of the anodic alumina separator were compared with that of the conventional polymer based separator. In comparison to polymer separator the alumina separator reportedly showed improved wettability with organic electrolyte and also exhibited excellent ionic conductivity and electrolyte retention capabilities, the essential criterion for a separator to qualify for use in Li-ion batteries. Further, they showed that the Li-ion batteries with alumina membrane used as a separator exhibited superior rate capabilities and better low temperature performances.

Santos et al. [116] prepared nanoporous anodic alumina by two-step anodization of aluminum foil in oxalic acid and successfully demonstrated its potential use as photoluminescent enzymatic sensor. The resulting change in effective optical thickness (derived from the PL spectrum) during functionalization, activation and enzyme immobilization stages was used for developing the sensor. The sensitivity of the sensor was shown to vary as a function of length and diameter of pores of the aluminum oxide. Their findings established that the nanoporous anodic alumina is of tremendous use for making optical biosensors.

Tsai et al. [117] used anodic aluminum oxide template for developing electron field emitters by electrochemically growing nanowires of nickel in vertically-aligned nano-tubes of the template. They succeeded to obtain electron field emitters of different emission characteristics with best emission seen from the wires of 100 nm length. It was established that the length and diameter of the tubes/wires had a significant effect on electron emission characteristics.

Hu et al. [118] used three different pour sealing methods namely hot nickel acetate bath, cold nickel acetate bath and hot water bath, to further enhance the corrosion resistance of aluminum anodized in sulphuric acid. The highest pore sealing was reportedly achieved using hot nickel acetate bath. Whereas, sealing done in cold nickel acetate bath was the least effective. Accordingly, the specimens sealed in hot nickel acetate bath reportedly showed highest corrosion resistance in de-aerated 1 wt.-% NaCl, followed by the anodized specimens sealed in hot water. Least corrosion resistance was observed for the as-anodized and un-sealed specimens.

Plasma electrolytic oxidation (PEO) is similar to anodization but employs much higher voltages, exceeding the voltage required for dielectric breakdown of the oxide. For PEO of aluminum at least 200 V is required [119]. This process is little complex as in addition to electrochemical oxidation that happens during anodizing, melting and solidification of the oxides so formed also takes place during PEO [120]. The coatings formed by this method are harder, stronger, thicker and more adherent than the same produced by simple anodization. Also, the coatings contain higher proportion of crystalline phases. On the other hand, the coatings obtained by this technique have some inherent defects like surface cracks, randomly arranged pores and inclusions, and higher residual stresses etc. According to Stojadinovic et al. [121] during PEO of aluminum there are several steps involved to form the oxide coating. The first step is the formation of a large number of separated discharge channels on the anode surface due to dielectric breakdown of the oxide. The local temperature of such channel goes on increasing up to $10^4$ K due to excessive amount of heat generated during electron avalanches [121]. Therefore, the substrate and oxide melts and a part of it get deposited into these channels where oxidation takes place. The oxidized metal subsequently expels out from the channels and gets deposited onto the coating surface, thereby increasing the coating thickness significantly as a result of repetition of this step [121].

Stojadinovic et al. [121] studied a few characteristics of the aluminum oxide coatings formed by PEO technique in an aqueous solution of sodium tungstate. A mixture of $\gamma$-$Al_2O_3$ and $\alpha$-$Al_2O_3$ phases was reportedly formed. Microhardness of the coatings was reported to decrease as the PEO time was increased. Surface morphology and topography of the coatings were reported as strongly dependent on the PEO time.

Guohua et al. [122] used sodium silicate, sodium phosphate and a combination of these baths for constant current PEO of aluminum. They observed a noticeable difference in the characteristics of the coatings formed in these baths. The coatings formed in phosphate electrolyte were found to contain a large amount of $\alpha$-$Al_2O_3$ due to a relatively high discharge voltage attained during the process; whereas, $\gamma$-$Al_2O_3$ and mullite were the main crystalline phases when PEO was conducted in silicate electrolyte. The coatings formed in phosphate electrolyte reportedly showed pores of larger diameter than that of the coatings formed in silicate solution. Guohua et al. [122] assigned this difference to the higher discharge voltage generated in phosphate solution leading to enhanced melting and sputtering of the anode surface that could result in the formation of a more porous coating.

Shen et al. [120] studied the microstructure and thermal shock resistance of the alumina coatings formed by PEO of aluminum conducted in sodium phosphate solution. They observed that the roughness of the PEO coatings depends mainly on current density and processing time and initial roughness of substrate does not account much. A longer time and higher current density applied during PEO reportedly made the coating rougher. Pore density of the coating was reported to decrease sharply as the processing time was increased whereas a reverse trend was observed for pore diameter. The decrease in pore density was attributed to the self-healing behaviour of small pores as the processing time was increased; whereas, the increase in pore size was assigned to the enhanced ejection of oxide species from the channels. They reported superior thermal shock resistance of PEO coatings as there were no cracks seen on the coating surface after carrying out the cyclic thermal shock tests up to 40 times in air.

Wu et al. [123] extended the PEO method to hot dip aluminized steel for improving its mechanical properties by forming $Al_2O_3$ layers on top of the aluminized steel. FeAl/$Al_2O_3$ (bilayer) and FeAl/Al/$Al_2O_3$ (trilayer) structures with crystalline alumina consisting of $\gamma$-$Al_2O_3$, mullite and $\gamma$-$Al_2O_3$ phases were reportedly formed. Wu et al. [123] observed that the PEO treated specimens had hardness as high as 19 GPa, substantially higher than that of the aluminized steel.

### 2.1.5 Sol-gel methods

The technique of coating formation by sol-gel method can be divided into two categories first, sol-gel dip coating and second, sol-gel spin coating [124]. However, spraying and electrolytic methods have also been suggested in conjunction with sol-gel used as a depositing fluid [124]. In sol-gel dip coating method a substrate is dipped into a fluid sol and after a few seconds of dipping the substrate is vertically withdrawn from the sol at a constant speed. During this process the gravitational draining, solvent evaporation and condensation reactions lead to the formation of a solid film on the substrate surface [125]. Sol-gel dip coating is a very cost effective method for producing coatings as no expensive equipment is required. The sol-gel spin method differs from the sol-gel dip technique that in the case of former the thickness of the film is controlled by the combined action of centrifugal draining and evaporation [125]. By sol-gel methods, coatings of $ZrO_2$, $TiO_2$, $SiO_2$, $CeO_2$ and $Al_2O_3$ etc. can be easily prepared for various purposes [124]. Besides ceramic coatings it is also possible to form organic-inorganic and metal rich coatings using this method [124]. Some of the reported results on characteristics, properties and applications of the $Al_2O_3$ coatings produced by sol-gel method are described in the following paragraphs.

Wang et al. [38] prepared $Al_2O_3$ coatings on Fe-Cr-Al alloys for tritium permeation barrier applications for fusion reactors, by sol-gel method using a magnetically stirred solution of Al-iso-propoxide $Al(OC_3H_7)_3$, $HNO_3$ and water. They investigated the effect of substrate pre-oxidation and annealing temperature on the characteristics of alumina coatings. At 500 °C their coating remained amorphous whereas in the temperature range of 650–800 °C metastable $\gamma$-$Al_2O_3$ was formed and finally at 1100 °C they succeeded to obtain the stable $\alpha$-$Al_2O_3$. For coating prepared on pre-oxidized substrate there was no difference in crystal structure and it remained as $\alpha$-$Al_2O_3$ at 1100 °C. Although, the outer surface of the coatings prepared by Wang et al. [38] appeared porous, but a highly dense structure, desirable for tritium permeation barrier application, was reportedly seen along the cross-section.

Ueki et al. [126] studied the electrical insulative behaviour of the alumina coatings, prepared by sol-gel technique on SS304 substrate, in molten Pb-Li pool for fusion reactor applications. For the electrical insulation test carried out up to 170h duration (in Pb-Li pool maintained at 300 °C) the coatings displayed promising electrical insulation behaviour, but the insulation behaviour was breached when the temperature of the pool was increased beyond 430 °C. The thermal expansion mismatch between coating and substrate above the curing temperature of coating reportedly lead the coating detachment and that could result in breakdown of insulation behaviour.

Hua et al. [127] prepared optical grade amorphous $Al_2O_3$ films on silicon and fused quartz substrates by sol-gel spin-coating method using a mixed solution of $Al(NO_3)_3 \cdot 9H_2O$, glacial acetic acid, acetylacetone and polyvinyl alcohol. Although their films showed optical transparency exceeding 92% in the wavelength range of 400–1200 nm but, the reported value of optical band gap was much less than that of the bulk alumina.

Ruhi et al. [128] compared the pitting corrosion behaviour of sol-gel alumina coated and uncoated 9Cr-1Mo ferritic steel in chloride bearing environment. This steel is being widely used in petroleum and power generating plants [128]. They found that the alumina coatings increased the corrosion resistance of 9Cr-1Mo ferritic steel by one order of magnitude in 100 and 200 ppm $Cl^-$ containing solution. SEM examination of the coated and uncoated specimens, after corrosion test, confirmed the occurrence of only a few numbers of shallow pits for coated specimen in comparison to the large number of wider and deeper pits for uncoated specimens.

Mitra et al. [129] reported on the formation of optically transparent, high catalytic activity, hexagonally ordered, mesoporous aluminum oxide thin films on soda lime and silica glass substrates by sol-gel method. X-ray diffraction (XRD) measurement reportedly showed the formation of $\gamma$-$Al_2O_3$, after the coating was annealed at 900 °C. The catalytic activity of ordered mesoporous alumina films was reportedly found to be significantly better than that of the disordered alumina films, reflected by the difference in decomposition reaction rate of aqueous $KMnO_4$.

### 2.1.6 Thermal methods to form alumina coatings on aluminized surfaces

Research work done in the past few years has established that the alumina coatings formed on the aluminized surface of ferritic-martensitic steels are promising for their use as tritium permeation barrier (TPB) for fusion reactors [39–42]. By high temperature selective oxidation of aluminized steel alumina coatings can be formed. The formation of iron-aluminide can be done by pack cementation and hot dip aluminizing (HDA) methods [40,130]. In hot dip method, the steel specimen is dipped into aluminum melt kept in an inert atmosphere, at around 700 °C to form $Fe_2Al_5$ on the steel surface [131]. The specimens are then subjected to annealing to convert the brittle $Fe_2Al_5$ to ductile Fe-Al. Subsequent oxidation of the specimens at around 950-1075 °C leads to the formation of $Al_2O_3$ layers on top of the aluminide coatings [132]. Glassbrenner and Wedemeyer [133] obtained an α-Fe(Al)/FeAl/$Al_2O_3$ trilayer coating on F82H-mod and MANET ferritic-martensitic steels by heat treating the hot dip aluminized specimens at 1040 and 1075 °C for 30 minutes, for fusion reactor applications. They succeeded to achieve complete incorporation of aluminum into the steel. Further, the formation of α-$Al_2O_3$ was observed only at 1075 °C. Similarly, Chang et al. [130] reported on the formation of Fe-Al/$Al_2O_5$ layers on 9Cr-1Mo substrate using a two-step HDA technique. Recently, Purushothaman et al. [134] showed a fivefold increase in hydrogen permeation resistance of RAFM steel when $Al_2O_3$/Fe-Al-Si layers were formed onto it. Further, they confirmed that using an aluminum melt of higher Si concentration coatings having improved properties along with higher permeation resistance were easy to form. Abro and Lee [135] observed that the $\alpha$-$Al_2O_3$ scales eventually formed on aluminized carbon steel during corrosion testing in $N_2$/0.1% $H_2S$ gas at 800 °C significantly improved the corrosion resistance of the specimens. Very recently, Li et al. [136] reported on the formation of $TiAl_3$/$Al_2O_3$ coatings on TiBw/Ti6Al4V titanium matrix composites by HDA followed by high temperature oxidation, for their potential use as an oxidation resistant material for aerospace and automobile applications.

The second thermal method to form alumina coatings is the pack cementation. In this technique, the component is placed in an air-tight retort containing a mixture of aluminum alloy, alumina and an activator, for example, ammonium chloride [137]. The specimens to be coated are embedded in the mixture of powders followed by argon gas purging of retort to exclude air. Subsequently, the retort is heated to 800–1050 $^{o}$C for several hours and finally cooled down to room temperature [137]. The aluminum halide so formed decomposes into aluminum on the substrate surface. Yang et al. [40] reported on the formation of Fe-Al/$\alpha$-$Al_2O_3$ layers by controlled atmosphere oxidation of the pack aluminized SS316L specimens. Gas phase tritium permeation test of their specimens indicated tritium permeation reduction factor higher than 3000. Similarly, Yuan et al. [138] reported a tritium permeation reduction factor higher than 1000 for the alumina coatings formed by in-situ oxidation of the pack aluminized CLAM and SS316L steels.

### 2.1.7 Alumina coating formation by oxidation of aluminum electrodeposited in ionic liquids

For the past several years, electrochemical deposition of aluminum using non-aqueous baths has been practiced for various purposes [139–142]. Due to relatively narrow electrochemical potential window of water, the electrodeposition of aluminum is not possible in aqueous medium as hydrogen evolves on cathode at a much lower potential than that required for aluminum ion reduction. There are mainly two non aqueous routes for aluminum electrodeposition namely, molten salts and ionic liquids. The difference between the two lies only in the melting temperature. Molten salts melt at temperature much higher than 100 °C whereas ionic liquids have melting temperature lower than 100 °C [143]. Therefore, electrodeposition of aluminum is much simple in ionic liquids than molten salts. Further, by using electrochemical methods not only the thickness of the coating can be controlled easily rather it is also possible to form coatings of very low thickness in comparison to the relatively thick and non uniform coatings obtained by hot dip aluminizing, as mentioned by Wulf et al. [131]. The aluminum coatings formed on steel substrates by electrodeposition method can be converted to Fe-Al/$Al_2O_3$ layers for using them as tritium permeation barrier coatings for fusion reactor related applications. For the past 3–4 years there is a spurt on research done on this subject [39,41,42,144,145]. Zhang et al. [39] formed aluminum coatings on 321 stainless steel substrate in $AlCl_3$-EMIC ionic liquid and then converted Al coating to (Fe,Cr,Ni)Al/$(Fe,Cr,Ni)_3Al/\gamma\text{-}Al_2O_3$ layers by two-step heat treatment method. They reported deuterium reduction factor more than two orders at 600–627 °C for the coated steel. In their another work [41], a deuterium reduction factor of more than two-three orders was reported for the alumina-aluminide coatings formed on HR-2 steel using the same method. In another work reported by the same group [42], the tritium permeation resistance of $Al_2O_3$/FeAl coatings on 321 stainless steel substrate was studied and the tritium permeation reduction factor for coated steel was found to be higher than 3 orders of magnitude at 500–700 °C, in comparison to the bare steel. Considering the significant importance of ionic liquids in electroplating of Al and other metals a brief introduction to the same is given in the following paragraphs.

Ionic liquids are compounds that are entirely composed of ions and are normally in liquid state below 100 °C [146]. They have been widely used for various materials processing activities including separation, electrolysis, lubrication, thermal fluids, biomass treatment, liquid crystals, nanotechnology and nuclear energy etc. [147–149]. Ionic liquids have many attractive properties that include high thermal stability, low vapour pressure, good solubility, wide electrochemical potential window, high electrical conductivity and non flammability [147–149]. Ionic liquids can be broadly categorized in five different types namely, halometallate ionic liquids, air and water stable ionic liquids, deep eutectic solvents, ionic liquids with metal containing cations and protic ionic liquids [147]. In the following paragraphs a brief description of these ionic liquids is given.

### *Halometallate Ionic liquids*

Halometallate ionic liquids, the earliest type of ionic liquid identified suitable for electrodeposition, are formed by mixing an organic chloride with a metal chloride such as $AlCl_3$, $ZnCl_2$ or $FeCl_3$ [147]. In the case of aluminum, the widely used ionic liquid formed by mixing an organic chloride (EMIC or BMIC) with $AlCl_3$ is known as first-generation ionic liquid [147]. The $[Al_2Cl_7]^-$ complex so formed in the Lewis acidic solution can be reduced to metallic Al by applying a suitable potential difference between anode and cathode. The acidity of halometallate ionic liquids can be optimized by varying the molar ratio of metal chloride to organic chloride. Halometallate ionic liquids are advantageous as nanostructured materials can be directly deposited using this electrolyte without the need of a template [147]. On the other hand, such ionic liquids are unstable in air and moisture containing environment and therefore an inert atmosphere is required for carrying out the processing activities.

### *Air and water stable ionic liquids*

These ionic liquids are very stable in air and moisture containing environments and therefore inert atmosphere is not required for their preparation and processing. Such ionic liquids being hydrophobic in nature also possesses wide electrochemical window and therefore have been extensively employed for electrodeposition of a large number of metals [147]. Examples of air and water stable ionic liquids are $BF_4^-$, $PF_6^-$, $[F_3CSO_3]^-$(TfO), $[(F_3CSO_2)_2N]^-$($NTf_2$), Ethylsulfate and 1-butyl-3-methylimidazolium salicylate based ionic liquids [147].

### *Deep eutectic solvents*

As the name employs, deep eutectic solvents are the eutectic mixture of either Lewis acids and bases or Bronsted acids and bases [150]. These ionic liquids are composed of quaternary ammonium salts (e.g. Choline chloride, ChCl) and hydrogen bond donors (urea, carboxylic acids and polyols) [147,150]. The main advantages of deep eutectic solvents include biocompatibility, wide range of solubility, wide deposition potential window, very low reactivity with air and moisture and low cost [147]. Electrodeposition of various metals including Ni, Zn, Cu, Se, Co, Sm, Pd, Pb, In, Ag, Sn and Fe has been successfully reported using deep eutectic solvents [147].

### *Ionic liquids with metal containing cations*

These ionic liquids are designed to increase the solubility of metal salts by employing metal complexes as cations [147]. Using these ionic liquids higher deposition rate can be obtained and it is possible to carry out electrodeposition at higher current densities [148]. Examples of such ionic liquids are $[Cu(MeCN)_2][NTf_2]$, $[Cu(PhCN)_2][NTf_2]$, $Ag(MeCN)_4]_2[Ag(NTf_2)_3]$ and $[Ag(EtIm)_2]NTf_2$ complexes containing ionic liquids [147].

***Protic ionic liquids***

By transfer of protons from a Bronsted acid to a Bronsted base, protic ionic liquids are formed [147]. In comparison to aprotic ionic liquids protic ionic liquids are cheaper and also possess less toxicity. However, protic ionic liquids have narrower potential window and therefore their use in electrodeposition is limited to metals having less negative reduction potentials [147].

## 2.1.8 Other techniques to form alumina coatings

Jie and Ying-Chun [151] developed a very simple and cost effective room temperature deposition technique named as chemical liquid phase deposition for obtaining very smooth thin films of alumina on semiconductor substrates for example, GaAs and Si, from a controlled pH aqueous solution consisting of $Al_2(SO_4)_3{\cdot}18H_2O$ and $NaHCO_3$. The formation of $Al_2O_3$ was reportedly achieved by dehydration and polymerization reactions of $Al(OH)_3$ precipitated on the submersed substrate surface. A mixture of $\beta$-$Al_2O_3$ and $\gamma$-$Al_2O_3$ phases was reportedly formed after annealing the film at temperature higher than 1000 °C. However, this process could be applied only for ultrathin alumina films finding applications in electronic devices and beside this limitation it is also not possible to use this process on substrates other than semiconductors.

Mohan et al. [152] reported on the formation of alumina layers by electrophoretic deposition route for its potential use as a protective overlay coating on yttria stabilized zirconia (YSZ), the latter being widely used as a thermal barrier coating for advanced gas turbine engines for aero-propulsion systems. The electrophoretic deposition of alumina was reportedly carried out by applying a potential difference of 30V across the two electrodes (the cathode was alumina coated graphite discs on which YSZ was previously applied and the anode was made of graphite) kept in a colloidal suspension prepared by dispersing alumina powder in an acetone-ethanol-iodine based organic solvent. Liquid phase calcium-magnesium-alumino-silicate (CMAS) interaction test with the sintered alumina coated specimens reportedly showed complete suppression of CMAS melt filtration across the alumina overlay coating.

Kavitha and Jayaram [153] used combustion flame pyrolysis technique to deposit crystalline alumina coatings on SS316 and silica substrates. The effect of three different precursor solvents namely, 100% water, 50% water + 50% methanol and 100% methanol, each containing dissolved aluminum nitrate, used to deposit the coating, on the crystal structure and surface morphology of alumina coatings was studied. Coatings were produced by the reaction of atomized precursor droplets with the high temperature oxy-acetylene flame, very similar to that happens during thermal/plasma spray method. The alumina coatings deposited using 100% water and 50% water + 50% methanol at 700 and 950 °C substrate temperature were reported as amorphous under un-annealed conditions. However, the coatings deposited using 100% methanol solvent were reportedly composed of pure $\alpha$-$Al_2O_3$ phase at the substrate temperature of 800 °C, due to substantial amount of extra heat produced by exothermic reaction in this case. Surface morphology of the coatings was found to depend more on the substrate temperature rather than the type of solvent used. The coatings deposited with 100% water as a solvent were reported as relatively hard due to less porosity.

Exner et al. [154] obtained alumina films on alumina and glass substrates by aerosol deposition method. The effect of powder characteristics for example, specific surface area, particle size and compressibility index on ease of deposition was studied. To deposit adherent coating on alumina substrate the most important and reported parameter was the specific surface area of the alumina particles. Particles having specific area on the higher side (5.5–8 $m^2/g$) were easy to deposit on alumina substrate whereas, for glass substrate alumina particles having low specific surface area but larger average diameter (1.5 to 4.5 µm) could form the adherent film.

Wu et al. [155] designed and developed a novel method termed as microwave plasma jet technique to deposit alumina coatings under atmospheric pressure conditions on SS304 substrate. High temperature plasma of helium and nitrogen was generated in front of the high purity aluminum disc target using 2.45-GHz microwave source. The evaporated aluminum atoms reacted with oxygen from atmosphere and formed alumina coating on the substrate placed near the plasma jet. The coating formed at 800W microwave power was reported as a mixture of $\delta$ and $\beta$ alumina whereas at 1500W $\alpha$ and $\beta$ phases were seen in the coating. A deposition rate of 2 µm/min was reportedly achieved by this technique.

# Chapter-3

## Experimental

This chapter describes the materials and methods used for (a) electrodeposition of aluminum coatings from $AlCl_3$-EMIC ionic liquid and their characterization, (b) thermal oxidation of electroplated aluminum and characterization of the subsequently formed alumina layers and (c) anodization of aluminum in 10% oxalic acid and a mixed solution of oxalic acid and citric acid, and characterization of the so formed alumina coatings.

## 3.1 Aluminum electrodeposition in $AlCl_3$-EMIC ionic liquid

The study on aluminum electrodeposition is divided into two parts. In the first part electrodeposition was done using a relatively low purity electrolytic bath under unstirred conditions whereas, the second part deals with the aluminum electrodeposition in a relatively high purity bath with continuous stirring. The details of experiments done without stirring are provided in section 3.1.1 and that for with stirring in section 3.1.2.

### 3.1.1 Electrodeposition without electrolyte stirring

In this section, materials and methods used for electrodeposition of aluminum in an unstirred $AlCl_3$-EMIC ionic liquid bath are described. Additionally, the characterization techniques used for analyzing the so formed coatings are also described.

**Materials and methods**

Anhydrous $AlCl_3$ powder (purity: 98%) and EMIC (purity: 95%) were used to prepare the bath. Mild steel (MS: 25 mm x 15 mm x 1 mm) and copper (25 mm x 15 mm x 1 mm) plates were used as substrate to deposit aluminum, whereas high purity aluminum (purity better than 99.5%) sheets of 150 mm x 25 mm x 2 mm dimension were used as anode. A custom designed glove box equipped with a load lock facility was used for carrying out the electroplating experiments. High purity argon gas was used to create an inert atmosphere inside the glove box. Additionally, anhydrous phosphorous pentoxide ($P_2O_5$) powder was kept inside the glove box in order to decrease the moisture content further.

Electroplating experiments including electrolyte preparation were done in a 500 ml glass beaker. The electrolyte was prepared by slow addition, with constant stirring, of $AlCl_3$ powder into EMIC in a molar ratio of 1.5:1. The as prepared solution had a dark brown colour, probably due to impurities such as residual water. To remove the residual water pieces of aluminum foil were immersed in the solution over a period of 1 week [43]. The solution finally obtained was translucent and had a light brown colour. This step was very critical and essential otherwise no aluminum could be deposited. Two types of substrates were prepared; in one type, the copper and MS plates were polished to mirror finish, and in another type the MS plates were subjected to wet alumina blasting (particle grit size: 10 µm). For pretreatment of copper and MS the substrates were first degreased in acetone and then chemically cleaned in a proprietary alkaline solution (trisodium tripotassium silicate) at 70 °C followed by dipping in 30% HCl for 20–30 s and finally rinsed with deionized water. Cleanliness of the substrates was checked by a water film test. The substrates were then dried, weighed and covered with a lacquer on areas not to be plated upon. Subsequently, the cathode was immediately transferred to the electrochemical cell. The aluminum anodes were also cleaned in a 10% NaOH solution just before the start of electrolysis to remove the inherent oxide layer formed on their surface. Experiments were conducted at room temperature (28 °C) for 1h in the applied deposition current density range of 5–17.5 $mAcm^{-2}$ in steps of 2.5 $mAcm^{-2}$. The current density value was obtained from the literature [43,156].

After the plating was over, the cathode was taken out and the same was washed immediately in a sufficient volume of analytical grade isopropyl alcohol for about 15–20 min to dissolve the residual ionic liquid still adhering to the specimen. The last step was found to be very important as, failing that, the deposited aluminum was quickly ruined due to reaction with the residual ionic liquid. The removal of residual ionic liquid could be done more efficiently in a Soxhlet apparatus [157].

The cathode current efficiency (*CCE*) was calculated by weight gain method as per equations 3.1.1.1 and 3.1.1.2 [158].

$$CCE(\%) = \frac{W_{cs} - W_s}{W_t} \times 100 \qquad (3.1.1.1)$$

where, *CCE*: Cathode current efficiency (%), $W_{cs}$: Weight of coated specimen (g), $W_s$: Weight of uncoated specimen (g) and $W_t$: Theoretical weight of deposit (g)

The theoretical weight of deposit can be calculated as

$$W_t = \frac{I \times t \times M_{Al}}{n \times F} \qquad (3.1.1.2)$$

where, *I*: Current (A) passed during electroplating, *t*: duration (s) of electroplating, $M_{Al}$: Molecular weight of Al, *n*: number of electrons taking part in the reaction and *F*: Faradays constant (96500 C/mol)

**Characterization of electrodeposited coatings**

For characterization two specimens prepared under identical conditions were used. Crystal structure of the coatings was determined by X-ray diffraction (XRD) measurements in θ–2θ mode using monochromatic CuKa$_{\alpha}$ radiation (wavelength: 0.154 nm). The chemical composition of the coatings was determined by X-ray fluorescence (XRF) and energy dispersive X-ray spectroscopy (EDS) measurement techniques. The surface morphology and grain size estimation were done in a scanning electron microscope (SEM) at an electron accelerating potential of 20 kV. The thickness of the coatings was measured by examination of cross-section of the coated specimens. One specimen was studied for evaluating the coating-substrate bonding strength in a progressive linear microscratch test. In this scratch test, done as per ASTM standard C1624-05, the indenter is driven into the coating up to a maximum defined test load at a defined loading rate. Progressive mode scratch test is advantageous as it covers the wide range of force. Therefore a single test can determine the load of adhesive failure. On the contrary, constant load scratch test requires a number of tests to be done in order to confirm the load at which adhesive failure occurs in the coating [159]. The adhesion test was performed using a microscratch tester up to 30N load at the loading rate of 30 N/min. The scratch impressions created in the coating due to indenter penetration were examined under an optical microscope.

### 3.1.2 Electrodeposition under stirred electrolyte conditions

In this section, the materials, methods and experimental techniques used for electrodeposition of aluminum using a stirred $AlCl_3$-EMIC ionic liquid bath are described. The characterization techniques used for analyzing the so obtained coatings are also described.

#### Materials and methods

The electrodeposition experiments were conducted in the high purity argon gas filled glove box. The electrolyte was prepared by slow addition of anhydrous $AlCl_3$ powder (purity: better than 98%) into EMIC (purity: better than 98%) in a molar ratio of 2:1. Wet alumina blasted T91 (Fe9Cr1Mo) steel test coupons of 25 mm x 20 mm x 2 mm size and having an average roughness of 1.5 µm were used as the substrate. Just before electrodeposition, the substrates were pretreated in the following sequence: ultrasonication in analytical grade acetone followed by alkaline cleaning in a trisodium tripotassium silicate solution kept at 70 °C, washed under the stream of tap water, immersed in a boiling 10 wt.-% NaOH solution for about 15 min, washed under the stream of tap water, dipped into 30 vol.-% HCl for 10–15 s and finally washed with deionized water. The cleaned substrate was dried and then immediately transferred to the electrochemical cell where two parallel, vertically aligned, high purity aluminum sheets were used as anode. Electrodeposition was conducted at room temperature for 2 h in constant current mode at a fixed current density of 20 $mAcm^{-2}$. Stirring of solution was done using a speed controlled magnetic stirrer. The speed of magnetic stirrer was varied from 200 rpm to 900 rpm in steps of 100 rpm.

### Characterization of coatings

Crystal structure of the coatings was determined by XRD measurement. The details of XRD measurement are given in section 3.1.1. The morphology of the coatings was examined under both stereo optical microscope and SEM. The surface topography and roughness of the coatings were measured by a stylus based profilometer (vertical resolution: 100 nm) having the stylus tip diameter of 250 nm. The profilometer was operated in the raster scan mode at 0.5 mg contact force. The thickness of the coatings was measured by magnetic method (resolution: 0.1 µm, accuracy: 1%), as per standard ISO 2178, at a minimum of eight different points excluding edges of the specimens. The average of these values was reported as the thickness of the coating. In magnetic method of thickness measurement the magnetic gauge is kept on the coated specimen. The magnitude of force of attraction between the magnetic gauge and substrate is inversely proportional to the thickness of the non magnetic coating and the thickness is derived from the magnetic force [160].

## 3.2 Thermal oxidation of aluminum coatings

This section describes the conversion of aluminum coatings, obtained by the techniques described in sections 3.1.1 and 3.1.2, to alumina layers by thermal oxidation method, and characterization of the so obtained coatings using various analytical tools.

**Materials and methods**

Approximately 20 μm thick aluminum coating electrodeposited in $AlCl_3$-EMIC ionic liquid at 10 $mAcm^{-2}$ current density was taken up for thermal oxidation to convert the aluminum into alumina. The thermal oxidation experiments were conducted in a programmable electric furnace. Due to large difference in coefficient of thermal expansion of aluminum and T91 steel it was difficult to obtain adherent aluminum oxide coatings by a single step thermal oxidation. A few such experiments conducted in air resulted in complete delamination of the coating. Therefore, a two-stage thermal oxidation procedure was envisaged. First, the aluminum coated specimen was subjected to heating in vacuum ($2.0 \times 10^{-3}$ Pa) at a slow heating rate of 3 $^{\circ}Cmin^{-1}$ up to the maximum temperature of 300 $^{\circ}C$ followed by soaking at this temperature for more than 24 hours. In the second step, the adherent aluminum coatings obtained after first thermal treatment were heated in air (in the closed furnace) at a relatively fast heating rate of 10 $^{\circ}Cmin^{-1}$ up to 650 $^{\circ}C$ followed by soaking at this temperature for more than 16 hours. The specimen was cooled to room temperature at a very slow cooling rate of 2–3 $^{\circ}Cmin^{-1}$. The improved bonding of aluminum coating with T91 steel, due to diffusion of aluminum atoms into the substrate, after first stage of thermal treatment did not allow the coating to get delaminate during second stage of thermal oxidation.

### Characterization of oxidized coatings

XRD measurement was done on aluminum coated specimens before and after the thermal oxidation. Details of the procedure of XRD measurement are given in section 3.1.1. The obtained pattern was matched with JCPDS database and peaks of aluminum, iron-aluminide and chromium-aluminide were identified (card nos. 85-1327, 14-0336, 50-0955 and 02-1239, respectively). Diffusion of aluminum into T91 steel after first stage of thermal oxidation was confirmed by measuring the chemical composition of the specimen by XRF with top aluminum layer removed by mechanical grinding and polishing. EDS measurement was done to analyze the composition of the as-deposited and oxidized specimens. The oxidized specimens were checked for electrical insulation by measuring electrical resistance of the specimens using a two probe electrical resistance measuring gauge. The thickness of the coatings was measured by examination of cross-section of the coated specimen. Adhesion test was conducted for the oxidized specimen using the procedure described in section 3.1.1. During scratch test a load of 0.9 N was applied at the start of the test whereas the maximum test load was limited to 20 N near the end of the test. Parameters of the scratch tests are listed in Table 3.2. Normal load, frictional force and coefficient of friction, acoustic emission and depth of penetration data were recorded simultaneously using a computer based data acquisition system interfaced to the scratch adhesion tester. The resulting scratch impressions left on the coated specimen were examined under an optical microscope and the type of damage occurring to the coating was identified.

**Table 3.2** Parameters used during scratch testing of thermally oxidized aluminum coatings

| Parameter | Value |
|---|---|
| Begin load | 0.9 N |
| End load | 20 N |
| Loading rate | 30 N min$^{-1}$ |
| Acoustic emission sensitivity | 7 |
| Indenter speed | 4.71 mm min$^{-1}$ |
| Scratch length | 3 mm |
| Indenter type | Rockwell |
| Indenter material | Diamond |
| Indenter tip radius | 200 µm |

## 3.3 Anodization of electrochemically formed aluminum coatings

This section describes the electrochemical method of converting the aluminum, obtained by electrodeposition technique as described in sections 3.1.1 and 3.1.2, to layers of alumina and the subsequent characterization of the oxidized specimens.

### Materials and methods

Anodization of the aluminum coatings deposited on Fe9Cr1Mo steel substrate was conducted at an applied potential of 15V for 15 min duration in a freshly prepared 20 vol.-% $H_2SO_4$ solution maintained at 4–5 °C. The low bath temperature was achieved by placing the anodizing cell in a larger beaker and filling the annular space between the two beakers by ice cubes. During anodization experiments, the aluminum coated Fe9Cr1Mo steel specimen and the stainless steel 304L sheet were used as anode and cathode, respectively. Before transferring the aluminum coated Fe9Cr1Mo steel specimen to the bath it was cleaned in a dilute NaOH solution for 5–10 s to remove the oxide layer followed by dismutting in $HNO_3$.

### Characterization of anodic oxide layers formed on aluminum coatings

The crystal structure and chemical composition of the anodic coating were determined by XRD and EDS techniques, respectively. The surface morphology was analyzed by SEM. The procedure of XRD, EDS and SEM measurements is described in section 3.1.1.

## 3.4 Anodization of aluminum metal in oxalic acid

This section describes the use of anodization technique to form alumina coatings on aluminum metal substrates. In this section, details are given for the anodization experiments of aluminum conducted in 10% oxalic acid bath and characterization of the so obtained alumina coatings.

### Materials and methods

Specimens of dimension 30 mm × 25 mm were cut from the aluminum sheet of thickness 1 mm and used for the experiments. Table 3.4.1 shows the chemical composition of the aluminum used in this study. It may be noted that, for anodization studies aluminum in the form of an alloy was used because of the fact that for most of the industrial applications aluminum alloys are preferred over high purity aluminum because of their higher strength. The specimens were polished using successive finer grades of SiC papers. Just prior to anodizing, the specimens were first cleaned in 10% NaOH solution at 45 °C to remove the oxides present on its surface. The specimens were subsequently desmutted in 50% $HNO_3$ to remove the black stains. The black stains are caused by the formation of hydroxides of Fe, Cu and Si, present in the aluminum, during cleaning in NaOH solution [161]. The anodizing bath was prepared by dissolving the calculated amount of analytical grade oxalic acid crystals into 250 ml of de-ionized water, with the help of a magnetic stirrer. Experiments were conducted in a glass beaker at room temperature with slow stirring of solution for 1 h, in potentiostatic mode, at an applied potential of 10–30 V, potential varied in steps of 5 V for separate specimens. Studies available on anodization of aluminum in oxalic acid solutions show that at temperatures lower than room temperature the growth rate of aluminum oxide is considerably low, whereas at room temperature, the rate of growth of the oxide is substantially high [47,162]. On the other hand, at temperatures higher than room temperature the growth rate increases further but the size of the pores of aluminum oxide also increases significantly [163]. Therefore in the present work, anodization was conducted at room temperature. During anodizing, the temperature of the bath was monitored continuously with the help of a digital thermometer. No significant change in the temperature of the bath could be noticed when different potentials were applied (in the range of 10–30 V) and the temperature remained close to room temperature. Therefore the solution was not cooled. The anodizing potential range was chosen based on the studies reported in literature [164]. It may be noted that the anodization of aluminum in oxalic acid solution is possible within a large potential window (potentials lower than 5 V and higher than 60 V have been reported) [164,165]. However, the pore size of anodic alumina increases significantly with the increase in applied potential [56]. The presence of large pores is detrimental for applications such as corrosion protection due to easy penetration of the corrosion causing ions through these pores up to the very thin barrier oxide layer present on the aluminum base. Therefore, the chances of corrosion of the underneath base metal are increased. In order to circumvent this problem either boiling water sealing or chemical based sealing treatments are required to close the pores [49]. However, all such techniques are expensive as they consume high energy and/or costlier chemicals [49]. Furthermore, at higher anodizing potentials (exceeding 30 V), the volume expansion of the anodic oxide is very high [164]. This can result in generation of large amount of internal stresses in the coating leading to the formation of cracks in the coating. On the other hand, use of very low potential (less than 10 V) makes the coating soft and also results in high pore density. Consequently, such coatings have inferior mechanical properties. Therefore, in the present work, anodization was carried out in the potential range of 10–30 V. Table 3.4.2 lists the details of the electrochemical cell used for carrying out the anodization experiments. The ultrasound assisted anodization was done by placing the beaker containing solution in ultrasonic cleaners having 90, 120 and 200W ultrasound powers and a fixed frequency of 40 kHz. Ultrasound assisted anodization was done for 30 minutes at a constant applied potential of 30V.

**Table 3.4.1** Chemical composition of aluminum used in the study

| Element | Al | Si | Fe | Cu | Zn |
|---|---|---|---|---|---|
| Wt.-% | 96.17 | 1.71 | 1.08 | 0.609 | 0.431 |

**Table 3.4.2** Anodizing cell details

| **Material/parameter** | **Identity/Value** |
|---|---|
| Anodizing bath | 10% Oxalic acid |
| Anode | Al sheet |
| Cathode | AISI SS316 L sheet |
| Anodizing potential | 10–30 V |
| Stirring speed | 50 rpm |
| Bath temperature | 30 °C |
| Anodizing time | 1h and 1h 20 min |

### Characterization of anodized aluminum

In the characterization part, for every test two specimens prepared under identical conditions were used. The chemical composition of the aluminum used for anodizing was measured by X-ray fluorescence (XRF; Innov-X, Delta). The crystal structure of the anodized aluminum was determined by both Bragg–Brentano (θ-2θ) XRD (ITAL STRUCTURES

Italy, HRD 3000) measurements and grazing incidence X-ray diffraction (GIXRD; X'Pert PRO MRD, PANalytical B.V.) measurements, using monochromatized CuKα radiation at a wavelength of 0.154 nm. During GIXRD measurements the incidence angle was fixed at 1°. The chemical composition of the anodized specimens was measured by EDS (Bruker; AXS Microanalysis GmbH) and XPS, using Mg-Kα (1253.6 eV) source and DESA-150 electron analyzer (Staib Instruments, Germany). The binding energy scale was calibrated to Au-4f7/2 line of 84.0 eV. For fitting and deconvolution of XPS data Gauss (~80%)-Lorentz (~20%) model was used. The surface morphology was analyzed by FE-SEM (ZEISS, AURIGA) at an accelerating voltage of 5 kV. During FE-SEM analysis, the secondary and the backscattered electrons were detected by the SE and the EsB detectors, respectively. Also, a thin layer of gold was sputtered on the anodized specimens to make the specimen surface electrically conductive for easy charge dissipation during FE-SEM examination. The thin layer of gold was deposited at a pressure of 10 Pa, for the time duration of 30 s, using an ion sputter coater (SEC Korea; MCM-100; 220VAC, 50 Hz) that consisted of a gold target of 50 mm diameter. A diamond stylus based surface profilometer (MEP Technology, NANOMAP-500LS), operating in the stage scan mode was employed to measure the surface topography and average roughness ($R_a$) of the specimens. In order to obtain more representative information about surface topography the profilometry was done on a relatively large area (1 mm × 1 mm). Parameters of the profilometry analysis are given in Table 3.4.3. The thickness of the anodic oxide coatings was measured by eddy current method (KARL DEUTSCH, LEPTOSKOP 2042, resolution: 0.1 μm, accuracy: better than 1 μm) using a zero degree configuration probe, at several points on the specimen, and the average of these values is reported. The thickness measured by eddy current method was corroborated by cross-section view FE-SEM examination of the anodized specimens. The hardness of the anodized specimens was measured by using a Vickers microhardness tester (ESEWAY hardness tester) operating at 100 gf and dwell time of 10 s. The hardness was measured at a minimum of five different points excluding edges of the specimens and the average of these values is reported. The elastic modulus was measured on the polished cross-section of the anodized specimens by nanoindentation technique (FISCHERSCOPE, HM2000) at a predefined load of 30 mN. The surface electrical resistivity of the specimens was measured by a custom designed four point probe method. During resistivity measurement, an electric current measuring 0.5 nA was applied between the outer two probes whereas the voltage was measured between the inner two probes. This is a standard technique for measuring the electrical resistivity of films and coatings by four point probe method [166]. The resistance against scratch damage was studied using a microscratch adhesion tester (CSM Instruments; RST S/N: 27-0497) operating in the progressive mode, as per ASTM: C1624-05. Scratch tests were conducted up to the maximum normal load of 50 N. The length of the scratch was kept at 3 mm. Parameters of the scratch test are given in Table 3.4.4. During scratch test normal load, frictional force, coefficient of friction, depth of penetration and acoustic emission curves were recorded online. The resulting scratch impressions were analyzed under optical microscope and SEM (SEC Korea; SNE-4500 M). More details of scratch test are given in section 3.1.1. Specimens anodized at 20, 25 and 30 V were selected for the scratch test. Wear test of the anodized aluminum specimens was done in a reciprocating-sliding wear tester operating at 5, 7, 9 and 11N normal load, 10 Hz sliding frequency and 2 minute duration. Alumina balls were used as the counter body during wear test. 3D profilometry was done on the worn surfaces of the specimens to measure the depth and size of the wear scars created, for calculating the wear volume and wear rate. During wear test the value of coefficient of friction was recorded online as a function of time.

**Table 3.4.3** Parameters of surface profilometry

| Parameter | Numerical value |
|---|---|
| Scan distance | 1000 µm |
| Scan speed | 150 µm $s^{-1}$ |
| Sample frequency | 150 pts $s^{-1}$ |
| Data resolution | 10 nm |
| Contact force | 10 mg |

**Table 3.4.4** Parameters of progressive load scratch test

| Parameter | Numerical value |
|---|---|
| Loading rate | 30 N $min^{-1}$ |
| AE sensitivity | 90% |
| Indenter tip radius | 200 µm |
| Indenter type | Rockwell |

## 3.5 Anodization of aluminum in a mixed solution of oxalic acid and citric acid

The formation of alumina coatings by anodization of aluminum metal using mixed solutions of oxalic acid and citric is described in this section. The characterization tools used for assessing properties of the coatings and the procedure of measurement are also described.

### Materials and methods

Specimens of 30 mm × 25 mm size were cut from a 1 mm thick aluminum sheet and used for carrying out the anodization experiments. A window of 15 mm x 15 mm area was made on the specimens by covering the rest portion by a lacquer. Just prior to anodization, the specimens were first cleaned in a boiling 10% NaOH solution to remove the oxides present on its surface. Subsequently, the specimens were desmutted in 50% $HNO_3$. The bath for anodization was prepared by dissolving the calculated amount of analytical grade oxalic acid and citric acid powders in de-ionized water, with the help of a magnetic stirrer. Anodization baths of different acid concentrations were prepared by dissolving different amount of oxalic acid and citric acid, keeping constant the oxalic acid to citric acid ratio and the total volume of bath at 1:1 and 250 ml, respectively. 5g, 15g, 25g and 35g powders of both oxalic acid and citric acid were used for preparing the bath. For a total amount of acid exceeding 70g (35g oxalic and 35g citric acid) it was not possible to fully dissolve the acids. Therefore, the maximum amount of acid used for preparing the bath was limited to 70g. Anodization experiments were conducted for 1 h using magnetically stirred solution in potentiostatic mode at an applied potential of 20–70 V, varied in steps of 10 V for separate specimens. Beyond 70 V there was significant rise in temperature of the bath due to Ohmic heating therefore anodization experiments were conducted only up to 70 V.

### Characterization of aluminum oxide coatings

The crystal structure of the anodized aluminum was determined by Bragg–Brentano XRD technique using monochromatic CuKα radiation (wavelength: 0.154 nm). The chemical composition of the anodic coatings was measured by XPS using Mg-Kα (1253.6 eV) source and DESA-150 electron analyzer (Staib Instruments, Germany). The binding energy scale was calibrated to Au-4f7/2 line of 84.0 eV. For fitting and deconvolution of XPS data Gauss (~80%)-Lorentz (~20%) model was used. The surface morphology was analyzed by FE-SEM (ZEISS, AURIGA) at an accelerating voltage of 5 kV. Porosity of the coatings was measured by analyzing the FE-SEM images using ImageJ software.

## 3.6 Presentation of results and discussion in this thesis

Results of the experiments conducted on aluminum electrodeposition using unstirred ionic liquid bath, described in section 3.1.1, are outlined in Chapter-4. Results of the aluminum electroplating studies done in a magnetically stirred ionic liquid bath, as detailed in section 3.1.2, are elucidated in Chapter-5. Results of the conversion of electroplated aluminum to alumina by thermal oxidation and electrochemical methods, as described in section 3.2 and section 3.3, respectively, are covered in Chapter-6. Results obtained from the experiments done on anodization of aluminum metal in oxalic acid and a mixture of oxalic acid and citric acid baths, as mentioned in sections 3.4 and 3.5, respectively, are described in Chapter-7 and 8.

# Chapter-4

## Effects of Current Density and Substrate on the Aluminum Coatings Electrodeposited in $AlCl_3$-EMIC Ionic Liquid

In this chapter, results of the experiments done on electrodeposition of aluminum using a relatively low purity, but cheaper $AlCl_3$ (98%)-EMIC (95%) ionic liquid bath under unstirred conditions, details given in section 3.1.1, are presented. For a quick reference the experimental conditions are summarized as follows. Aluminum electrodeposition experiments were conducted using an unstirred bath consisting of $AlCl_3$ (98%)-EMIC (95%) in a molar ratio of 1.5:1, in the applied current density range of 5-17.5 $mAcm^{-2}$ for 1h. Mirror finished MS, mirror finished copper and wet alumina blasted MS were used as substrate. The obtained aluminum coatings were studied for crystal structure, chemical composition, surface morphology and adhesive strength using XRD, EDS, SEM and scratch adhesion tester, respectively. This chapter also discusses the effect of current density on cathode current efficiency during deposition and, the effect of current density and substrate types on the crystal structure, surface morphology and adhesive strength of the aluminum coatings.

### 4.1 Effect of current density on cathode current efficiency

The cathode current efficiency during aluminum electrodeposition from $AlCl_3$ (98%)-EMIC (95%) bath on MS substrate, calculated by weight gain method (for details see section 3.1.1), as a function of deposition current density, is shown in Figure 4.1.1. It is evident that the cathode current efficiency decreased linearly as the current density was increased during deposition. Similar trend was observed also on the copper substrate. These results are in contrary to those reported by Jiang et al. [44] and Liu et al. [156] who observed decreased current efficiency only at much higher deposition current densities. In the present study, lower cathode current efficiency was attributed to the relatively low purity chemicals employed because of that side reactions become prominent at a higher deposition current density. The evidence of side reactions at higher current densities was found in the form of vertically aligned streak marks on the coated specimens (Fig. 4.1.2a and b). Such marks were considered as an indicator of hydrogen gas evolution at the cathode. However, no such marks were observed at low current densities (Fig. 4.1.2c). The evolution of hydrogen on the cathode was attributed to the presence of moisture in the low purity, lumpy EMIC used for the work. It may be noted that although electrodeposition of aluminum in ionic liquids has been practiced from the past several years, till date chemistry of the process is not well understood. Occurrence of the following cathodic and anodic reactions has been generally accepted during electrolysis of $AlCl_3$-EMIC [167].

Reaction at cathode

$$4\,Al_2Cl_7^- + 3e^- \leftrightarrow Al + 7AlCl_4^- \qquad (4.1.1)$$

Reaction at anode

$$4AlCl_4^- \leftrightarrow 2\,Al_2Cl_7^- + Cl_2 + 2e^- \qquad (4.1.2)$$

Overall reaction

$$2\,Al_2Cl_7^- \leftrightarrow 2Al + 2AlCl_4^- + Cl_2 \qquad (4.1.3)$$

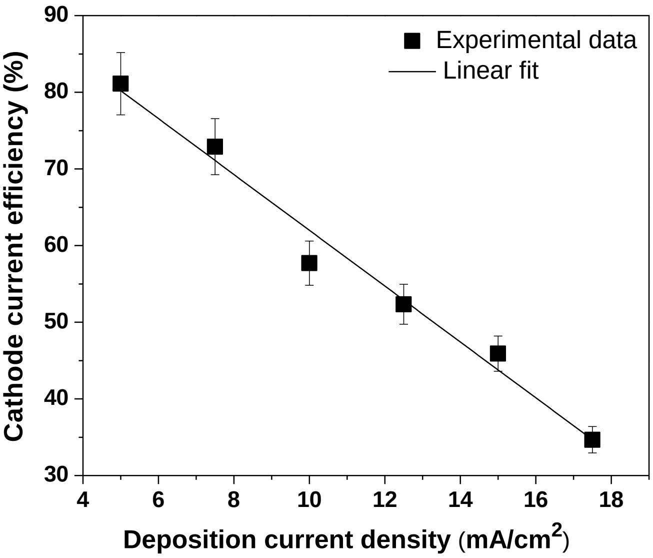

**Fig. 4.1.1** Experimentally calculated cathode current efficiency as function of applied current density for aluminum electrodeposition on mild steel using $AlCl_3$(98%)-EMIC(95%) ionic liquid bath.

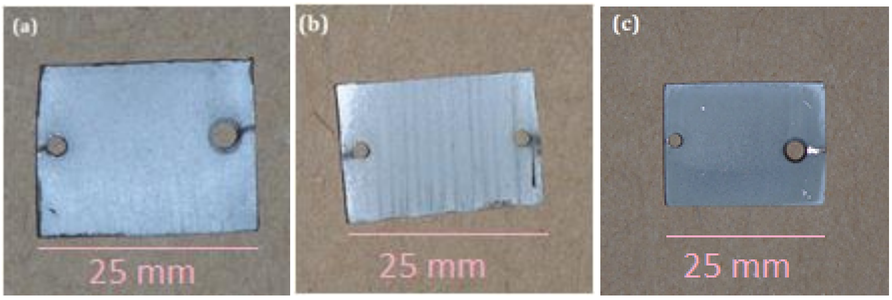

**Fig. 4.1.2** Photographs of the aluminum coatings electrodeposited on (a) wet alumina blasted MS at 15 mAcm$^{-2}$, (b) polished copper at 12.5 mAcm$^{-2}$ and (c) polished MS at 7.5 mAcm$^{-2}$ current density, using $AlCl_3$(98%)-EMIC(95%) ionic liquid bath at room temperature.

## 4.2 Crystal structure and chemical composition

Crystallinity of the aluminum coatings was examined by XRD technique for the specimens obtained at two different current densities (details given in section 3.1.1). The patterns obtained from XRD measurements of the coatings formed on copper substrate at 5 and 10 mAcm$^{-2}$ current densities are shown in Fig. 4.2.1. There could be seen (111) and (200) peaks of FCC aluminum at 38.5 and 44.9° diffraction angles. Further, at 5 mAcm$^{-2}$, the intensity of (200) peak was very low compared to (111) but the same become prominent at 10 mAcm$^{-2}$. At the same time, the intensity of peaks pertaining to Cu substrate lowered as the current density was increased. This was attributed to the increased thickness of aluminum coating leading to lesser penetration of X-rays into copper substrate.

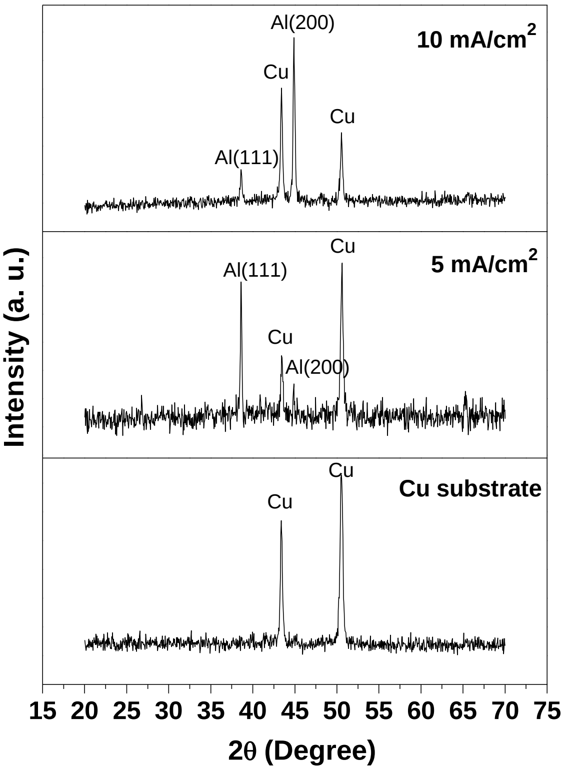

**Fig. 4.2.1** XRD patterns of the aluminum coatings formed on polished copper substrate at two different current densities (marked on the plot), using $AlCl_3$ (98%)-EMIC (95%) ionic liquid bath.

The chemical composition of the aluminum coatings deposited on copper and MS substrates, measured by XRF technique is given in Table 4.2. The XRF results showed 66.8 wt.-% Al, 32.5 wt.-% Cu and balance impurities such as, Fe and Mg for the coatings formed on copper. Similarly, on MS there was 64.5 wt.-% Al, 35.3 wt.-% Fe and 0.2 wt.-% Mn. Subtraction of substrate elements suggested the purity level of Al better than 99%. For further confirmation, few Al flakes were carefully removed from the coating deposited on MS and analyzed in EDS. The results of EDS measurement (last column, Table 4.2) also indicated the same level of purity. It may be noted that during EDS measurement O and Cl were detected only in trace amount hence their peaks were omitted during chemical composition analysis. Here it should be noted that the purpose of showing purity of the aluminum coating on different substrates by different techniques is just to ascertain that the aluminum coatings obtained from the $AlCl_3$ (98%)-EMIC (95%) bath are reasonably good and acceptable for most of the applications. But, it should be remembered that the XRF and EDS techniques are not very accurate to determine the purity of materials at a very fine level.

**Table 4.2** XRF and EDS results of electrodeposited aluminum coatings

| XRF analysis | | | | EDS analysis |
|---|---|---|---|---|
| | Al on Cu (Comp./wt.-%) | | Al on MS (Comp./wt.-%) | Al flakes removed from MS (Comp./wt.-%) |
| Al | 66.8 | Al | 64.5 | Al- 99.2 |
| Cu | 32.5 | Fe | 35.3 | Fe- 0.8 |
| Balance | Impurities Fe, Mg etc. | Mn | 0.2 | |

## 4.3 Effect of current density and substrate types on morphology

Surface morphology of the aluminum coatings formed on different types of substrates (polished copper and MS, and wet alumina blasted MS) and at various applied current densities was examined by SEM (procedure given in section 3.1.1). SEM images of the Al coatings deposited on polished copper substrate at 5, 7.5 and 10 $mAcm^{-2}$ current densities are shown in Figure 4.3.1a, c and e, respectively. It has been found that the coatings deposited at 5 and 7.5 $mAcm^{-2}$ (Fig. 4.3.1a and c) have cellular structure and insufficient coverage on the substrate. This feature is clearly visible in the higher magnification images shown in Fig. 4.3.1b and d. The coating formed at 10 $mAcm^{-2}$ was observed to fully cover the substrate and had microcrystalline, hexagonal plate shaped grains (Fig. 4.3.1e and f). From Fig. 4.3.1e and f, it is clear that the crystal size is very fine. Fine crystal size indicates the formation of a large number of nuclei, and the hexagonal shape of the crystals is indicative of a high deposition current density. Similar morphology was noticed for the coatings formed on polished MS (Fig. 4.3.2a–c). Jiang et al. [168] also reported identical morphology of the aluminum coatings deposited on tungsten and aluminum substrates at a more negative deposition potential. Figure 4.3.2b shows a less dense coating when deposited at 5 mAcm$^{-2}$ on polished MS. The formation of coatings with increased coverage on substrate surface, at a higher current density, was attributed to the increased overpotential. According to the atomistic theory of nucleation and growth in electrocrystallization, nucleation rate increases exponentially as the overpotential is increased [45]. The subsequent growth on numerous nucleation sites resulted in the formation of fine grained coating with better coverage of substrate. The cross-section view SEM image shown in Fig. 4.3.1g revealed approximately 10 µm thick uniformly grown coating on polished copper substrate.

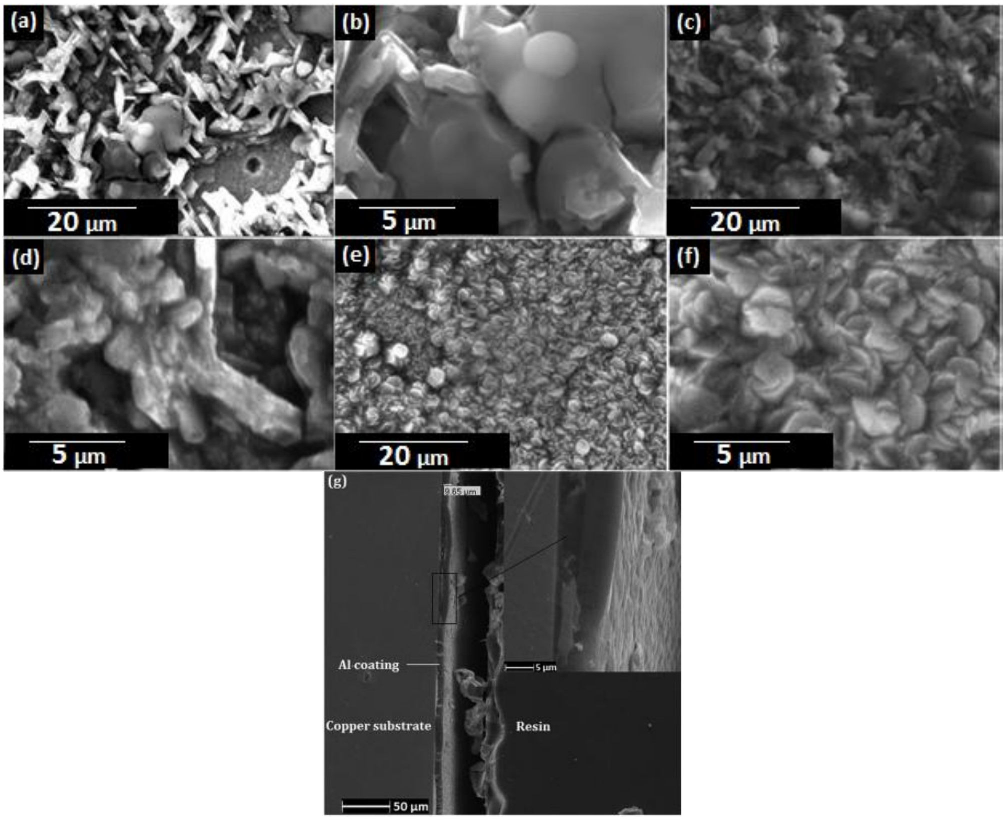

**Fig. 4.3.1** SEM images of the aluminum coatings formed on polished copper at (a) 5, (c) 7.5 and (e) 10 mAcm$^{-2}$ current density, using $AlCl_3$(98%)-EMIC(95%) ionic liquid bath; (b), (d) and (f) are higher magnification image of (a), (c) and (e), respectively; (g) cross-section view of (e).

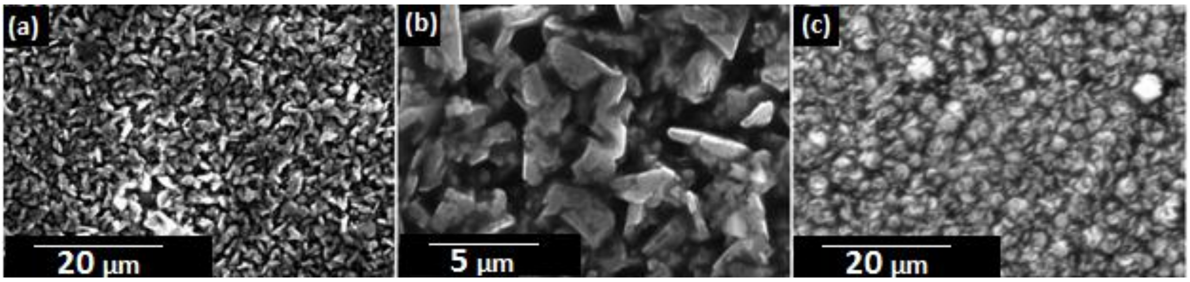

**Fig. 4.3.2** SEM images of the aluminum coatings deposited using $AlCl_3$ (98%)-EMIC (95%) bath on polished MS at (a) 5 and (c) 10 $mAcm^{-2}$; (b) is higher magnification image of (a).

The morphology of the aluminum coatings deposited on wet alumina blasted MS at 12.5 and 15 $mAcm^{-2}$ current densities are shown in Fig. 4.3.3a–d. In this case though there was only marginal difference in applied current density but the morphology of the resulting coatings differed greatly. The coating formed at 12.5 $mAcm^{-2}$ did not reflect any clear morphology (Fig. 4.3.3a and b), but at 15 $mAcm^{-2}$ highly compact and faceted grains of aluminum (Fig. 4.3.3c and d) could be easily seen. From these images, the average grain size of aluminum was estimated to be around 2–4 µm.

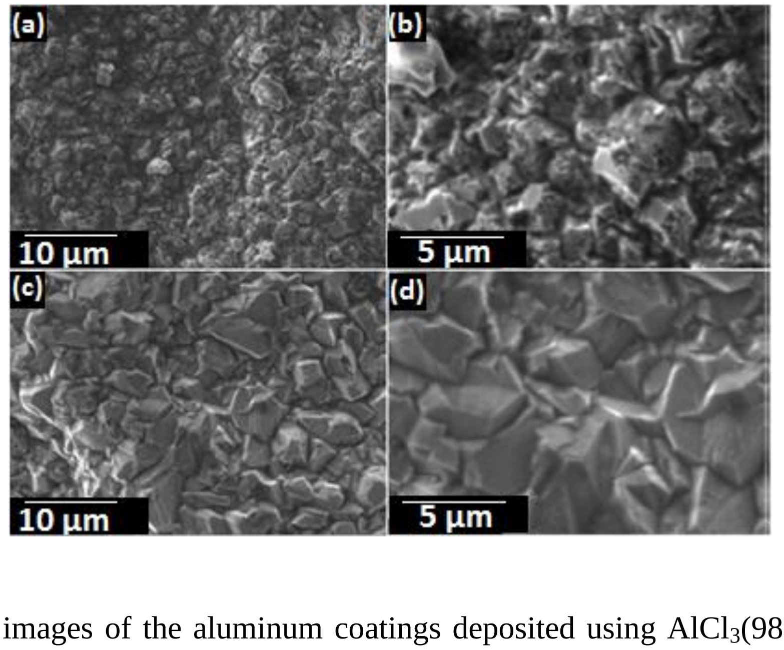

**Fig. 4.3.3** SEM images of the aluminum coatings deposited using $AlCl_3$(98%)-EMIC(95%) ionic liquid bath on wet alumina blasted MS at (a) 12.5 and (c) 15 $mAcm^{-2}$; (b) and (d) are higher magnification image of (a) and (c), respectively.

## 4.4 Adhesion evaluation of aluminum coatings

In the present study, adherent aluminum coatings could not be obtained beyond 10 mAcm$^{-2}$ current density either on mirror polished MS or copper substrates. Such coatings were found to be delaminated near base of the substrate (Fig. 4.1.2b). This was attributed to the building up of the excessive tensile stresses in the coating and the evolution of hydrogen gas at the cathode. However, on wet alumina blasted MS substrate adhesion of the coating was excellent and no delamination was observed. The load at which adhesive failure occurred to the aluminum coating deposited at 15 mAcm$^{-2}$ current density on wet alumina blasted MS substrate, was measured by a microscratch adhesion tester (for details of procedure see section 3.1.1) and no appreciable debonding between coating and substrate was found up to 20 N load, as revealed from the optical microscopy images of scratch track, shown in Fig. 4.4.1a–d. However beyond 20 N, multiple cracks and other defects appeared in the coating-substrate interfacial regions (Fig. 4.4.1e and f). The formation of adherent coatings on wet alumina blasted MS substrate and non-adherent coatings on well polished MS and copper substrates indicated the presence of stresses in the case of deposition done on polished substrate. It may be recalled that on wet alumina blasted substrate a little compressive stress is generated on the outer surface atoms during the blasting action that counteracts the tensile stresses developed during electroplating and hence the coatings formed on this substrate become adherent [169]. It may be noted that for protecting metals from corrosion by means of coatings it is essentially required that there should not be any uncovered portion left on the base metal otherwise the base metal will corrode at a much faster rate. This undoubtedly requires superior adhesion of the coatings.

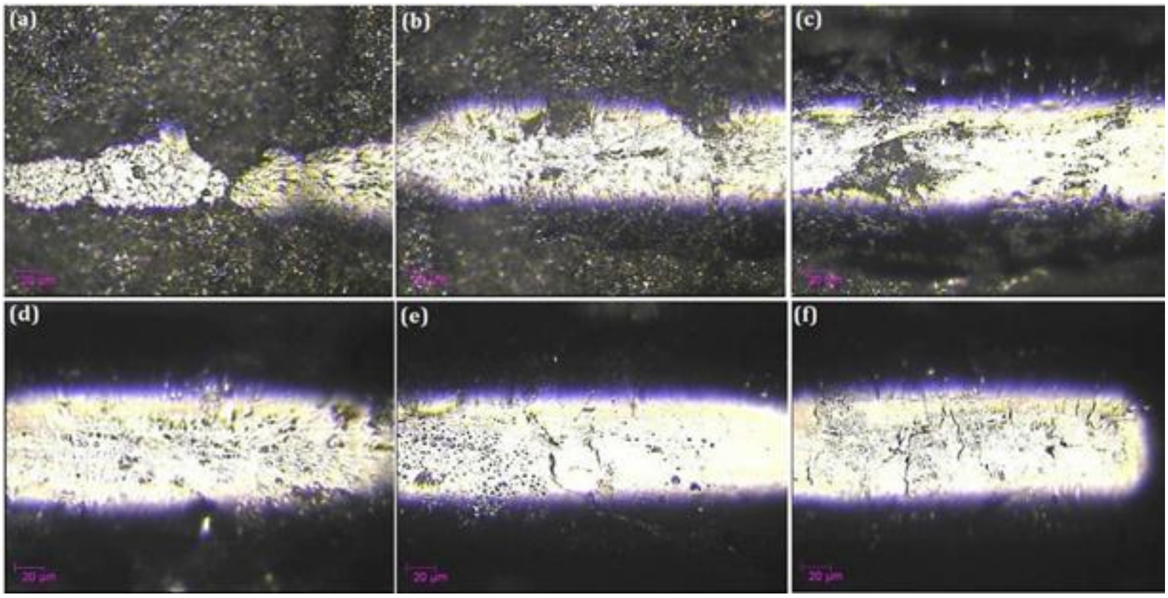

**Fig. 4.4.1** Optical microscopy images of the scratch track, created during scratch adhesion testing, on wet alumina blasted and aluminum coated mild steel at (a) 1, (b) 5, (c) 15, (d) 20, (e) 25 and (f) 30 N load.

## 4.5 Conclusions

The following conclusions were drawn from the present study.

- A simple chemical treatment to a low grade, but cheaper $AlCl_3$ (98%)–EMIC (95%) ionic liquid enabled it to be efficiently used for electroplating of aluminum on copper and mild steel substrates, having purity better than 99%. However, the cathode current efficiency obtained in this bath was relatively low in comparison to the high purity baths reported in literature.
- In $AlCl_3$ (98%)–EMIC (95%) ionic liquid bath the cathode current efficiency was found to decrease linearly on increasing the deposition current density.
- The morphological characteristics of the aluminum coatings deposited on polished MS and copper substrates were similar.

- Beyond 10 $mAcm^{-2}$ current density the adhesion of aluminum coating was found to be poor on polished MS and copper substrates but excellent on wet alumina blasted MS substrate.
- By choosing an optimum value of deposition current density adherent aluminum coatings were formed on wet alumina blasted MS substrate using a relatively cheap $AlCl_3$ (98%)-EMIC (95%) ionic liquid.

# Chapter-5

# Effects of Bath Stirring on Aluminum Coatings Electrodeposited using $AlCl_3$-EMIC Ionic Liquid

This chapter describes the difficulty associated with electrodeposition of aluminum on Fe9Cr1Mo steel using $AlCl_3$ (98%)-EMIC (98%) ionic liquid, at a relatively high current density, under unstirred conditions and overcoming this difficulty by means of bath stirring, referring section 3.1.2 of Chapter-3 for experimental details. A summary of the experimental conditions pertaining to this chapter is given as follows. Aluminum was electrochemically deposited on wet alumina blasted Fe9Cr1Mo steel in a magnetically stirred ionic liquid bath consisting of $AlCl_3$ (98%)-EMIC (98%) in a molar ratio of 2:1. Deposition was conducted for 2h, at 20 $mAcm^{-2}$ current density and 200-900 rpm stirring speed. The obtained aluminum coatings were studied for thickness, crystal structure, surface morphology and topography using magnetic gauge thickness meter, XRD, SEM and stylus based profilometer, respectively. In this chapter, the effect of bath stirring speed on the thickness, roughness, morphology, topography and crystal structure of the so formed aluminum coatings is established.

## 5.1 Issues of electrodeposition using unstirred ionic liquid

In the present work, using unstirred $AlCl_3$ (98%)-EMIC (98%) ionic liquid bath, aluminum electrodeposition experiments could be conducted only at current density less than 20 $mAcm^{-2}$. At 20 $mAcm^{-2}$ or higher current density colour of the solution turned to black from pale yellow and no more aluminum could be deposited using this solution at any value of current density. Liu et al. [170] reported electrodeposition of nanocrystalline aluminum in a partly decomposed $AlCl_3$-EMIC ionic liquid. At 50 $mAcm^{-2}$ colour of their solution also turned to black and no further deposition was reported using this solution [170]. They attributed it to the complete decomposition of the ionic liquid used for electrodeposition. In the present work also aluminum coatings could not be obtained on wet alumina blasted Fe9Cr1Mo steel substrate using $AlCl_3$-EMIC ionic liquid at 20 $mAcm^{-2}$ or higher current densities under unstirred conditions. However, upon stirring the solution aluminum was successfully plated out, and this fact excluded the possibility of decomposition of ionic liquids on account of the increase in deposition current density. The difficulty encountered while carrying out the plating experiments using an unstirred $AlCl_3$-EMIC ionic liquid at a relatively high current density has been attributed to the concentration polarization effect. Due to concentration polarization effect the sufficient amount of reducible $Al_2Cl_7^-$ ions could not get transported to the cathodic regions. This resulted in depletion of reducible $Al_2Cl_7^-$ ions near cathode and accumulation of $Al_2Cl_7^-$ ions in the bulk solution. The most likely reason for the observed change in colour of the solution (at 20 $mAcm^{-2}$ or higher current density under unstirred condition) was thought to be the dissolution of substrate elements e.g. $Fe^{2+}$ ions (from Fe9Cr1Mo steel) into the solution. When the electrolytic bath was stirred the transport of $Al_2Cl_7^-$ ions from bulk solution to cathodic regions could get enhanced as per the explanation given below.

The electrochemical deposition of Al in $AlCl_3$-EMIC ionic liquid can be described according to the reaction 4.1.1, mentioned in the previous chapter. In a pure $AlCl_3$-EMIC ionic liquid, $Al_2Cl_7^-$, $AlCl_4^-$ and $Cl^-$ ions are present in the solution and their relative concentration is defined as per the reversible reaction 5.1.1 [43].

$$Al_2Cl_7^- + Cl^- \underset{k_b}{\overset{k_f}{\rightleftharpoons}} 2AlCl_4^- \qquad (5.1.1)$$

Schaltin et al. [171] discussed the possible reactions of $Al_2Cl_7^-$ ions at cathode during electrodeposition of aluminum in a chloroaluminate bath. They mentioned that an $Al_2Cl_7^-$ ion while crossing the diffusion layer can either react electrochemically to form aluminum atoms (reaction 4.1.1) or it can react chemically with $Cl^-$ ion to form $AlCl_4^-$ ions (reaction 5.1.1). By the use of a finite element model and thermodynamics they showed that for a higher value of $k_b$, that happen at a higher rotation speed, an incoming $Al_2Cl_7^-$ ion can easily reach the cathode and contribute to the total current. Moreover, at a higher rotation speed the diffusion limiting current ($I_L$, equation 5.1.2) is increased because of the reduction in diffusion layer thickness ($\delta$, equation 5.1.3). In the present study, instead of using a rotating disc electrode the solution was stirred. But, the effect of the two conditions can be treated as similar.

The diffusion limiting current can be calculated as [172]

$$I_L = \frac{nFD}{\delta} c_b \tag{5.1.2}$$

where, $I_L$ is the diffusion limiting current, $n$ is the number of electrons taking part in the reaction, $F$ is the Faradays constant, $D$ is the diffusion coefficient and $c_b$ is the concentration of ions in bulk solution

The diffusion layer thickness can be calculated as [172]

$$\delta = \frac{a}{R^{2/3}} \tag{5.1.3}$$

where, $\delta$ is the thickness of diffusion layer, $R$ is the rate of stirring (rpm) and $a$ is a constant for a given solution, geometry and temperature

## 5.2 Effect of solution stirring speed during electroplating on coating thickness and roughness

The solution agitation not only enabled electrodeposition at higher current densities, it also resulted in increased deposition rate of the coating. The higher deposition rate again supported the increase in number of available reducible $Al_2Cl_7^-$ ions at the cathode on account of the increase in stirring speed. The thickness of the aluminum coatings formed on Fe9Cr1Mo steel, as a function of stirring speed, for electrodeposition experiments conducted at a constant current density of 20 mAcm$^{-2}$, details given in section 3.1.2, is shown in Fig. 5.2.1. It was found that the thickness increased linearly. Besides this one more advantage of stirring was the appreciable reduction in the formation of burrs on the edges of the coated specimens. The higher coating thickness at a higher stirring speed was attributed to the increased diffusion limiting current, as explained in section 5.1.

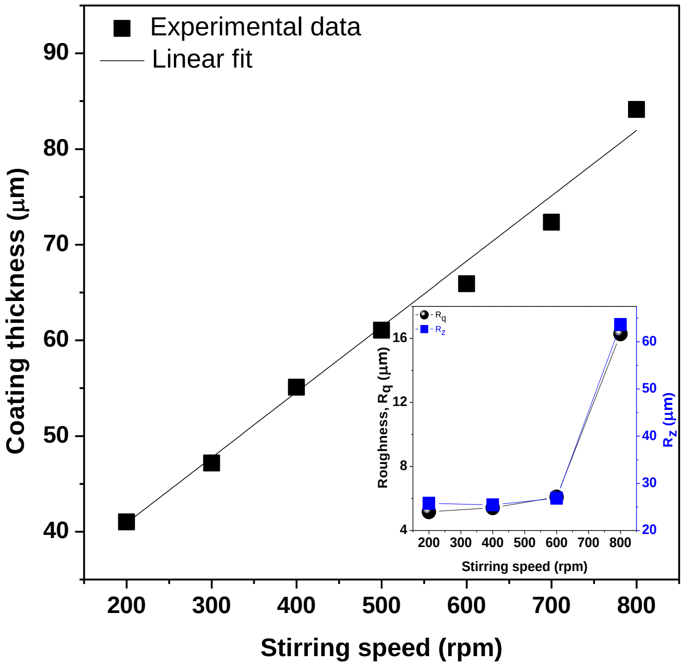

**Fig. 5.2.1** Thickness of the aluminum coatings formed on wet alumina blasted Fe9Cr1Mo steel, as a function of stirring speed, during electrodeposition from $AlCl_3$ (98%)-EMIC (98%) ionic liquid bath at 20 mAcm$^{-2}$ for 2h. Inset shows root mean square roughness and mean peak-to-valley distance for the coatings obtained at various stirring speeds.

Although the solution stirring resulted in higher deposition rate and reduction of burrs on the coated specimen edges, but on the other side it could also lead to increased roughness of the coatings, especially when the stirring speed was kept at 600 rpm or higher. The root mean square roughness ($R_q$) and mean peak-to-valley distance ($R_z$) measured for the coatings formed on Fe9Cr1Mo steel, at different stirring speeds, are shown in the inset of Fig. 5.2.1. This graph revealed that the roughness became abruptly high at stirring speeds exceeding 600 rpm. Also, images from the stereo optical and photographic examinations (Fig. 5.2.2a–d and Fig. 5.2.3a–c) of these coatings indicated the formation of large nodules on the coating surface at a higher stirring speed. The higher roughness was assigned again to the higher growth rate of the coatings formed at a higher stirring speed. The best coating in terms of optimum deposition rate, brightness, smoothness and without any visual defect was obtained at 200–400 rpm.

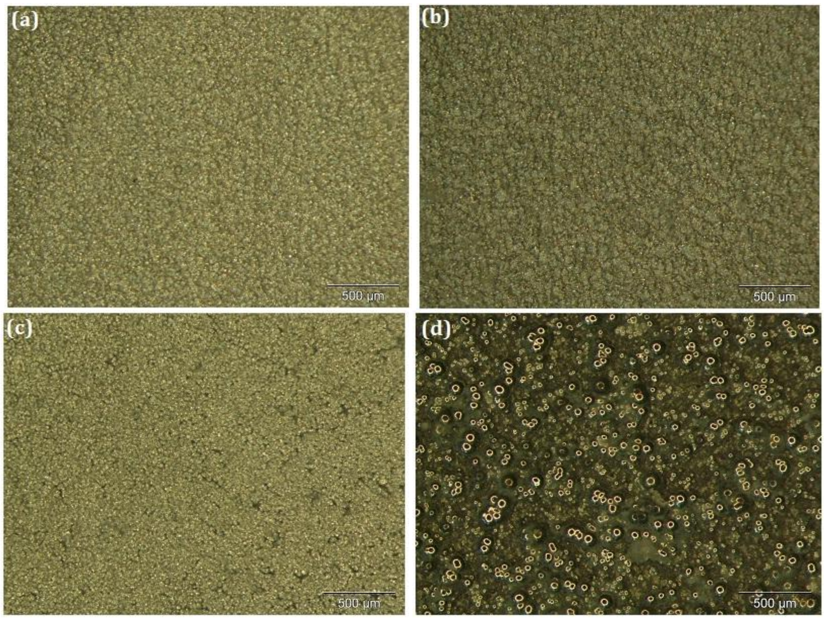

**Fig. 5.2.2** Stereo optical microscopy images of the aluminum coatings electrodeposited on wet alumina blasted Fe9Cr1Mo steel at (a) 200, (b) 400, (c) 600 and (d) 800 rpm stirring speed, using room temperature $AlCl_3$ (98%)-EMIC (98%) ionic liquid at 20 $mAcm^{-2}$ deposition current density for 2 h.

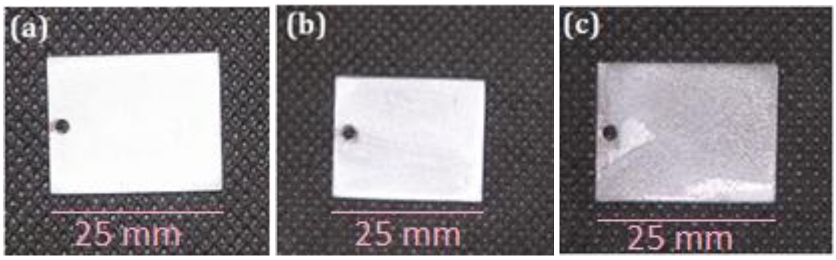

**Fig. 5.2.3** Photographs of aluminum coatings electrochemically formed on wet alumina blasted Fe9Cr1Mo steel using $AlCl_3$(98%)-EMIC(98%) bath at (a) 400 (b) 600 and (c) 800 rpm stirring speed.

## 5.3 Effect of solution stirring speed on morphology and topography

Morphology of the aluminum coatings formed on Fe9Cr1Mo steel, at various stirring speeds (section 3.1.2), was examined by SEM and the results of this analysis are shown in Fig. 5.3.1a–l. It is clear that the stirring speed has a pronounced effect on morphology. At 200 rpm the coating morphology consisted of disc shaped grains (Fig. 5.3.1a). The higher magnification image (Fig. 5.3.1b) of this coating revealed a non-uniform microstructure with a large separation existing between the individual grains. On increasing the stirring speed to 400 rpm, the morphology became relatively uniform (Fig. 5.3.1c) and the separation between the grains decreased to a large extent. A highly compact microstructure of the coating can be easily observed in Fig. 5.3.1d and 5.3.1e. A stirring speed of 600 rpm or higher could drastically change the morphology due to the formation of a large number of spherical nodules (Fig. 5.3.1e–l). Interestingly, the number density of spherical nodules increased on increasing the stirring speed from 700 to 900 rpm (Fig. 5.3.1g, i and k, respectively). One more important observation was the appearance of around 2 μm wide cracks in Fig. 5.3.1h, j and l. The most probable reason for crack formation was the substantial increase in the thickness of the coatings. It may be noted that for all other experimental conditions being the same, the coatings formed at 700, 800 and 900 rpm were approximately 1.75, 2.05 and 2.3 times thicker than the coating formed at 200 rpm (approximate thickness: 41 μm). The higher thickness leads to the development of higher residual intrinsic stresses in the coating, according to the equation 5.3.1 [173].

$$\sigma = \frac{E_s\left(t_s + \frac{E_c}{E_s}t_c\right)^3}{6rt_ct_s} \tag{5.3.1}$$

where, σ: stress in the coating; $E_s$: elastic modulus of the substrate; $E_c$: elastic modulus of the coating; $t_s$: thickness of the substrate; $t_c$: thickness of the coating; $r$: radius of curvature

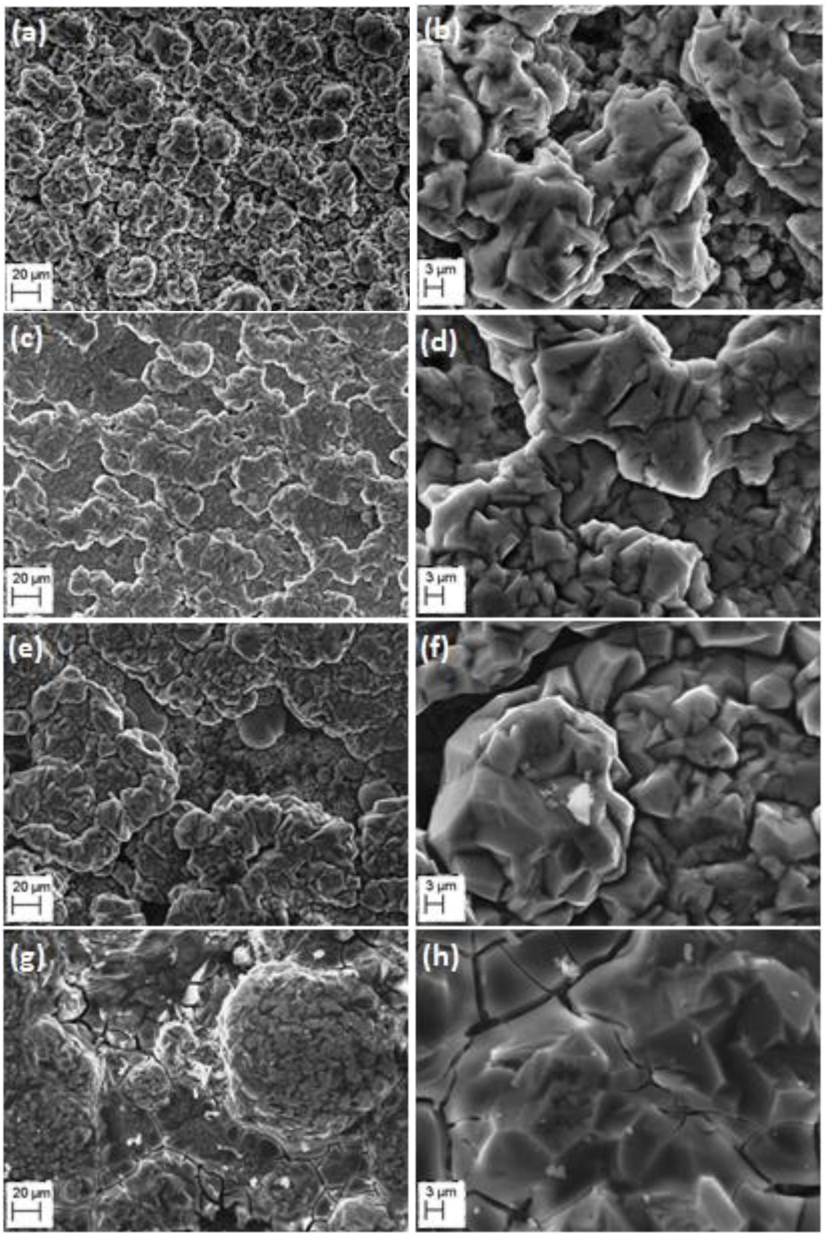

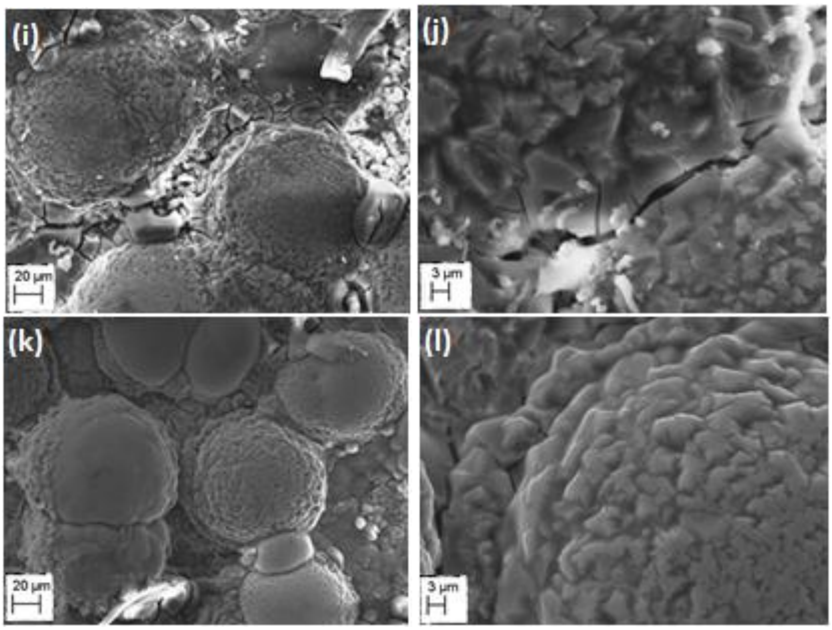

**Fig. 5.3.1** SEM images of the aluminum coatings electrodeposited on wet alumina blasted Fe9Cr1Mo steel, at 20 mAcm$^{-2}$ current density and 2h duration, using $AlCl_3$ (98%)-EMIC (98%) bath at (a) 200, (c) 400, (e) 600, (g) 700, (i) 800 and (k) 900 rpm stirring speed. (b), (d), (f), (h), (j) and (l) are the higher magnification images of (a), (c), (e), (g), (i) and (k), respectively.

Stafford et al. [174] reported the presence of high intrinsic stresses in the aluminum coatings electrodeposited using ionic liquids. In the present work also the increase in magnitude of intrinsic stresses with coating thickness was believed to result in the formation of cracks in the coatings. Moreover, from Fig. 5.3.1g–l it can be observed that the cracks are located mainly at the base of the large protruding nodules. This may be due to the fact that these regions can act as a site for stress concentration.

Surface topography of the aluminum coatings, formed on Fe9Cr1Mo steel substrate at various stirring speeds, examined by the profilometer is shown in Fig. 5.3.2a–l. From Fig. 5.3.2a–h it is evident that the coatings deposited at the stirring speed range of 200–700 rpm have similar topography. However, at 800 and 900 rpm there appeared a large number of spherical nodules, as clearly evident from Fig. 5.3.2i-l. Thus the results of profilometry supported the SEM examination results, discussed earlier. From Fig. 5.3.2j and l, diameter of the largest nodule was estimated to be around 100 μm. The topography images from 2D profilometry of the coatings obtained at various stirring speeds are shown in Fig. 5.3.3a–f. It is apparent that as the solution stirring speed was increased during electroplating the grain size of the resulting coatings also increased significantly. This was attributed to the increase in coating deposition rate, as discussed in section 5.2.

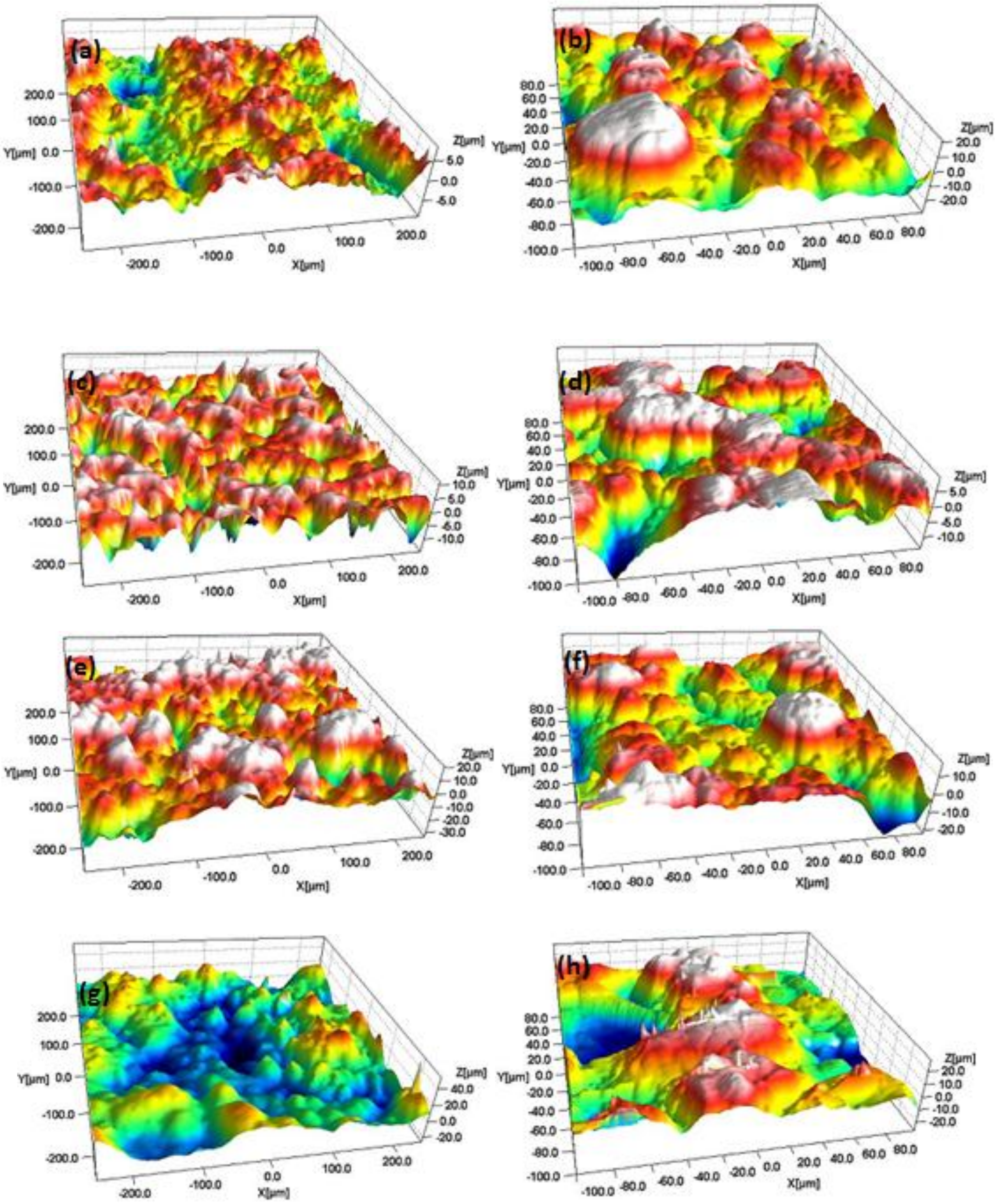

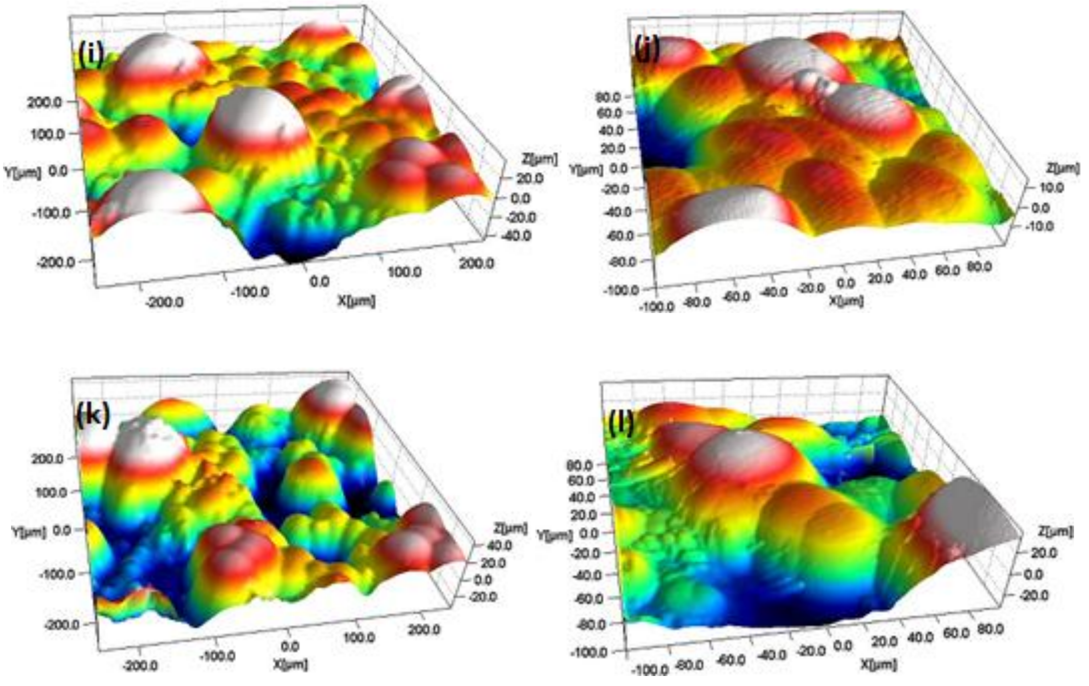

**Fig. 5.3.2** 3D profilometry images of the aluminum coatings formed on wet alumina blasted Fe9Cr1Mo steel using $AlCl_3$ (98%)-EMIC (98%) bath for 2h at (a) 200, (c) 400, (e) 600, (g) 700, (i) 800 and (k) 900 rpm stirring speed. (b), (d), (f), (h), (j) and (l) are the higher magnification images of (a), (c), (e), (g), (i) and (k), respectively.

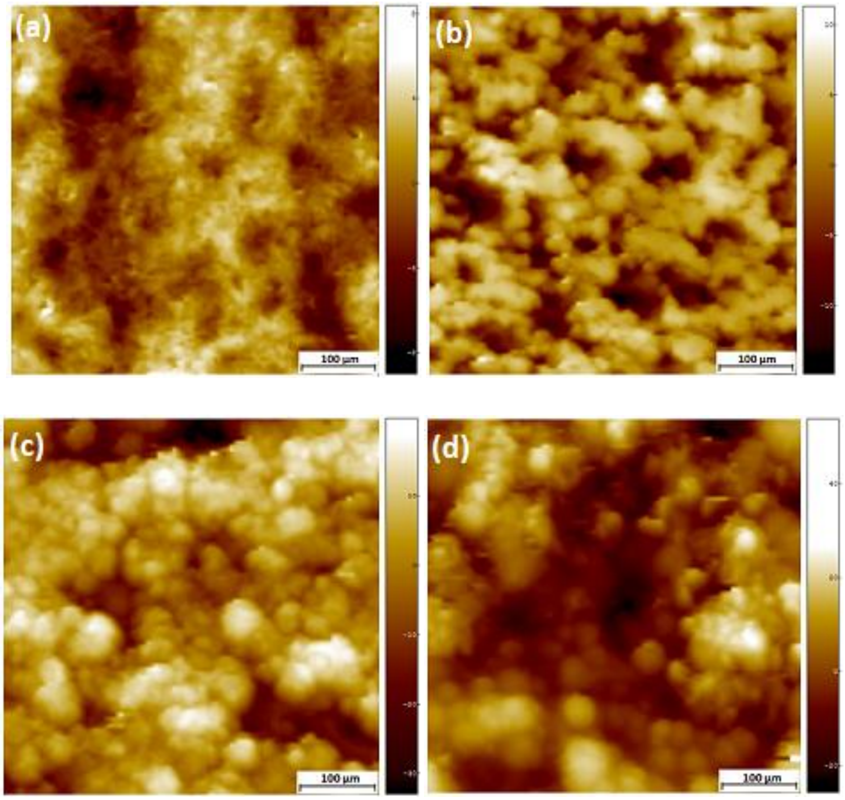

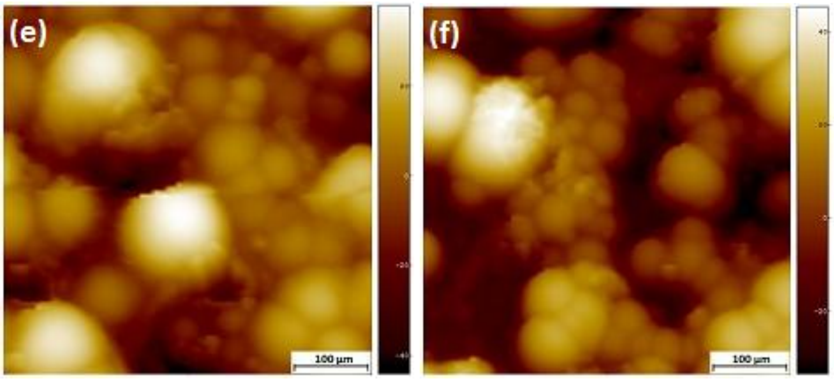

**Fig. 5.3.3** 2D profilometry images of the aluminum coatings electrodeposited on wet alumina blasted Fe9Cr1Mo steel using $AlCl_3$ (98%)-EMIC (98%) bath for 2h at (a) 200, (b) 400, (c) 600, (d) 700, (e) 800 and (f) 900 rpm stirring speed.

## 5.4 Effect of solution stirring speed on crystallographic orientation

The effect of solution stirring speed on the crystallinity of aluminum coatings was established by carrying out the XRD measurements of the coated specimens (section 3.1.2). Fig. 5.4.1a shows XRD patterns of the aluminum coatings formed on Fe9Cr1Mo steel at various stirring speeds. The patterns show (111), (200), (220) and (311) reflections of FCC aluminum. Further, it can be observed that on increasing the stirring speed the relative intensity of the planes is getting changed. Yue et al. [175] discussed about the effect of deposition current density and bath temperature on the crystallographic orientation of aluminum electrodeposited from $AlCl_3$–BMIC ionic liquid. They used equation 5.4.1 to calculate the normalized intensity of various reflections.

$$P_{hkl} = \frac{I_{hkl}/\sum I_{hkl}}{Ir_{hkl}/\sum Ir_{hkl}} \qquad (5.4.1)$$

where, $I_{\mathrm{hkl}}$ is the measured intensity of (hkl) reflection of aluminum coating, $\Sigma I_{\mathrm{hkl}}$ is the sum of the measured intensities of all the reflections of aluminum coating, $Ir_{\mathrm{hkl}}$ is the intensity of (hkl) reflection of aluminum given in the JCPDS database and $\Sigma ir_{hkl}$ is the sum of the intensity of all the reflections of aluminum given in the JCPDS database

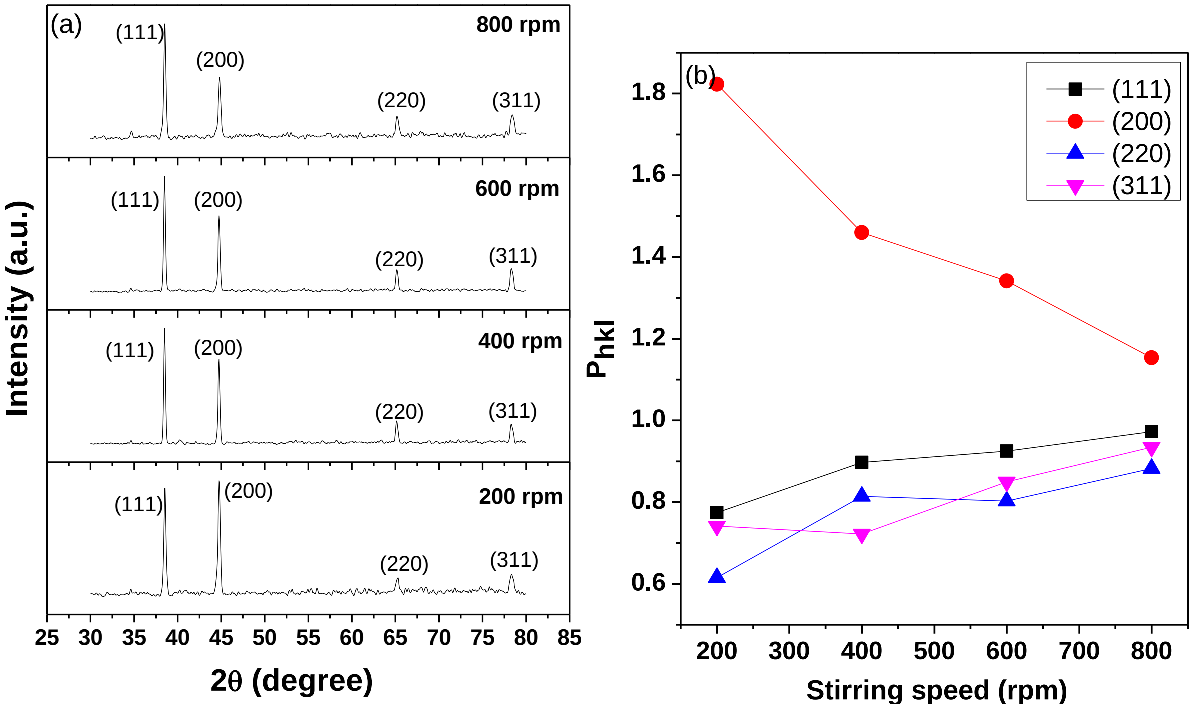

**Fig. 5.4.1** (a) XRD patterns and (b) calculated normalized intensity of XRD reflections ($P_{hkl}$), as function of stirring speed, for aluminum coatings electrodeposited on wet alumina blasted Fe9Cr1Mo steel using $AlCl_3$ (98%)-EMIC (98%) ionic liquid bath for 2h.

The normalized intensity calculated using equation (5.4.1), for all the observed reflections of aluminum is plotted against the solution stirring speed, employed during electroplating, in Fig. 5.4.1b. It is evident that as the solution stirring speed was increased from 200 to 800 rpm, the intensity of (200) reflection decreased drastically by 37%, whereas the intensity of (111) reflection increased by 26%. The other two relatively less prominent reflections namely (220) and (311) did not show any definite trend. Although the exact effect of solution stirring on the growth mechanism of crystallographic planes during electrocrystallization is not known but the same may be related to a greater extent to the deposition rate of the metal being deposited. In the present work, a higher stirring speed resulted in the formation of thicker coating, as discussed in section 5.2. In FCC crystal structure the atomic packing density of (111) plane is higher than that of the (200) plane and also the surface energy required to form (111) plane is lower than that for the (200) plane (Ref 176). Hence, at a higher stirring speed the (111) plane is expected to grow faster than the (200) plane [176]. This could finally result in decreased intensity of (200) plane and increased intensity of (111) plane.

## 5.5 Conclusions

The following conclusions were drawn from the present study.

- Solution stirring enabled electrodeposition of aluminum on wet alumina blasted Fe9Cr1Mo steel substrate from $AlCl_3$ (98%)–EMIC (98%) ionic liquid at room temperature, at a current density of 20 $mAcm^{-2}$ or higher. Without stirring the electroplating was possible only at current densities lower than 20 $mAcm^{-2}$. This behaviour confirmed the role of concentration polarization during electrodeposition of aluminum using ionic liquid.
- Solution stirring had a pronounced effect on the thickness of the coatings and the coating thickness increased linearly with stirring speed. However, at a stirring speed as high as 800 rpm the so obtained coating was significantly rough ($R_q$ higher than 16 µm) compared to the roughness of 4–5 µm at stirring speed of 200–600 rpm.
- Solution stirring had a significant impact on morphology and topography of the aluminum coatings formed on Fe9Cr1Mo steel. At a stirring speed exceeding 600 rpm there appeared a large number of spherical grains in the coatings.
- Solution stirring had a large impact on the preferred orientation of electrodeposited aluminum. In comparison to the coating formed at 200 rpm the coating obtained at 800 rpm showed 26% increase in normalized intensity of (111) reflection, whereas the intensity of (200) reflection decreased by 37%.

- By choosing an optimum value of solution stirring speed bright and smooth aluminum coatings were electrochemically obtained on wet alumina blasted Fe9Cr1Mo steel using room temperature $AlCl_3$ (98%)–EMIC (98%) ionic liquid.

# Chapter-6

# Formation of Alumina Coatings by Thermal Oxidation and Anodization of Electroplated Aluminum

In this chapter, results pertaining to crystal structure, chemical composition and microscratch adhesion behaviour of the Al plated T91 steel (Fe9Cr1Mo), after completion of the two-step thermal oxidation, as mentioned in section 3.2 of Chapter-3, are presented. The experimental conditions are briefed here again for a quick recap. Around 20 µm thick coating of aluminum was electrochemically formed on Fe9Cr1Mo steel using $AlCl_3$-EMIC ionic liquid. The aluminum coated Fe9Cr1Mo steel was then subjected to a two-stage thermal oxidation process to convert the aluminum to alumina. The thermally oxidized coatings were studied for crystal structure, chemical composition, morphology and adhesive strength using XRD, EDS, optical microscope and micro scratch adhesion tester, respectively. Also, one aluminum coated Fe9Cr1Mo steel was oxidized by anodization in 20 Vol.-% $H_2SO_4$ at 15V and 4-5 °C, and morphology and chemical composition of the resulting oxide layer were established by SEM and EDS, respectively.

## 6.1 Effect of thermal oxidation on crystal structure and chemical composition of electroplated aluminum

XRD results of the aluminum coating electrodeposited on T91 steel substrate, as described in section 3.1.2, and the same after completion of the two-step thermal oxidation, described in section 3.2 are shown in Fig. 6.1.1. Reflections of aluminum were seen in the patterns of both as-deposited and oxidized coatings, though the relative intensity of (111) and (200) reflections was changed after thermal oxidation. Besides this change, some distinct low intensity reflections belonging to Fe-Al and Cr-Al based intermetallic phases were observed after thermal oxidation. Konys et al. [177] reported the formation of Fe-Al based intermetallics e.g. $FeAl_2$, FeAl, $Fe_3Al$ and $Fe_2Al_5$ after annealing the electrochemically formed aluminum coatings at 980 °C. Similarly, Zhang et al. [39] also reported the formation of Fe-Al intermetallics after heat-treatment of aluminum coated steel at 700 °C. In the XRD pattern shown in Fig. 6.1.1 any peak pertaining to alumina could not be detected, indicating that the so formed alumina was amorphous. This was also supported by the unresolved baseline of XRD pattern of the oxidized specimen. There exists a large variation among the reported phases of alumina formed by thermal oxidation of aluminum. For instance, after air oxidation at 400 °C for 8 hours, Caporali et al. [178] reported the formation of amorphous alumina films on aluminum electrodeposited on mild steel using ionic liquids. But, Zhang et al. [39] reported the formation of $\gamma$-$Al_2O_3$ when the aluminum electrodeposited in $AlCl_3$-EMIC ionic liquid on 321 stainless steel work piece was oxidized in a controlled atmosphere at 700 °C.

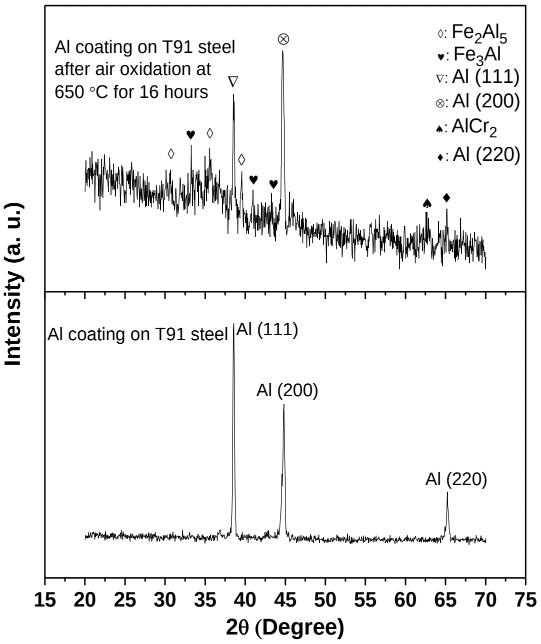

**Fig. 6.1.1** XRD pattern of aluminum coating electrodeposited on Fe9Cr1Mo steel from $AlCl_3$ (98%)-EMIC (98%) ionic liquid and XRD pattern of the same coating after being subjected to two-stage thermal oxidation treatment.

EDS measurements were taken for the as-deposited and oxidized aluminum coatings on Fe9Cr1Mo steel, to observe any change in chemical composition as a result of thermal oxidation. Fig. 6.1.2a and b shows the EDS patterns of as-deposited and oxidized aluminum coatings, respectively. The quantitative analysis of EDS spectrum (Fig. 6.1.2b) revealed approximately 50 wt.-% O present in the oxidized specimen whereas, no oxygen counts were observed in the case of as-deposited coating (Fig. 6.1.2a). The EDS pattern also showed a small peak of chlorine which comes from the constituents of the bath ($AlCl_3$ or EMIC). However, the EDS measurement could not detect iron and chromium from Fe-Al and Cr-Al intermetallic phases respectively, that were formed below the top alumina layer, as revealed from the XRD results (Fig. 6.1.1). This was essentially due to the fact that in EDS measurement the interaction of electrons in Z-direction is limited to a shorter distance compared to the deeper penetration of X-rays in XRD measurement.

The formation of alumina by thermal oxidation of aluminum coated Fe9Cr1Mo steel was also supported by the electrically insulative nature of such coatings, as detected by an electrical multimeter.

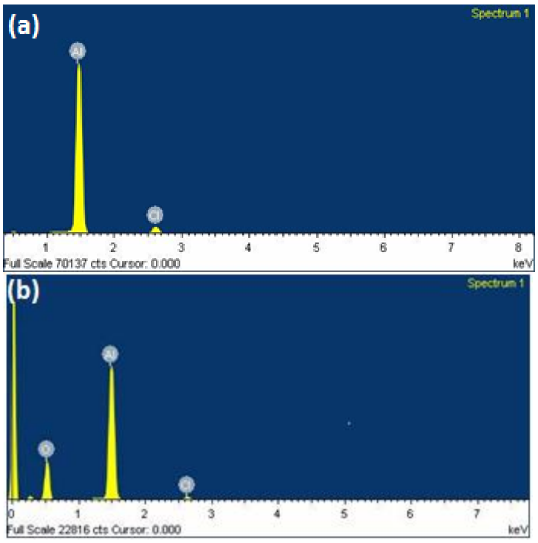

**Fig. 6.1.2** (a) EDS pattern of aluminum coating electrodeposited on Fe9Cr1Mo steel from $AlCl_3$ (98%)-EMIC (98%) ionic liquid and (b) EDS pattern of the same coating after being subjected to two-stage thermal oxidation treatment.

The cross-section view optical image of the oxidized specimen showed nearly 20-30 μm thick coating formed on T91 steel (Fig. 6.1.3). Since the two-step thermal oxidation was done up to the maximum temperature of 650 °C for more than 16 hours, there was substantial diffusion of aluminum atoms into the substrate. This could result in the formation of Fe-Al and Cr-Al based intermetallics in the Fe9Cr1Mo steel substrate region (confirmed from the XRD peaks of Fe-Al and Cr-Al phases shown in Fig. 6.1.1). Further, the two-step oxidation resulted in the formation of alumina layers on the outer surface of aluminum (evident from the oxygen peak appeared in the EDS pattern). Moreover, the presence of reflections of aluminum after thermal oxidation (Fig. 6.1.1) confirmed that aluminum was present in between the inner intermetallic region and the outer alumina layer. However, because of the low phase contrast such individual layers viz. alumina, aluminum and intermetallics could not be detected in the optical image of the cross-section of the coated specimen (Fig. 6.1.3).

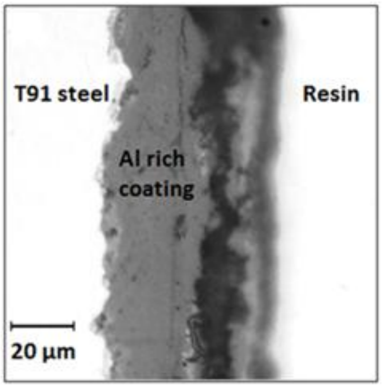

**Fig. 6.1.3** Cross-section view optical microscopy image of aluminum coated Fe9Cr1Mo steel, after being subjected to thermal oxidation treatment.

## 6.2 Adhesion measurement of oxidized aluminum coatings

Scratch adhesion test was conducted to estimate the adhesive strength of the oxidized aluminum coatings formed on Fe9Cr1Mo steel, as described in section 3.2. The results of optical microscopy examination of the scratch track on the oxidized aluminum coating are shown in Fig. 6.2.1a–h.

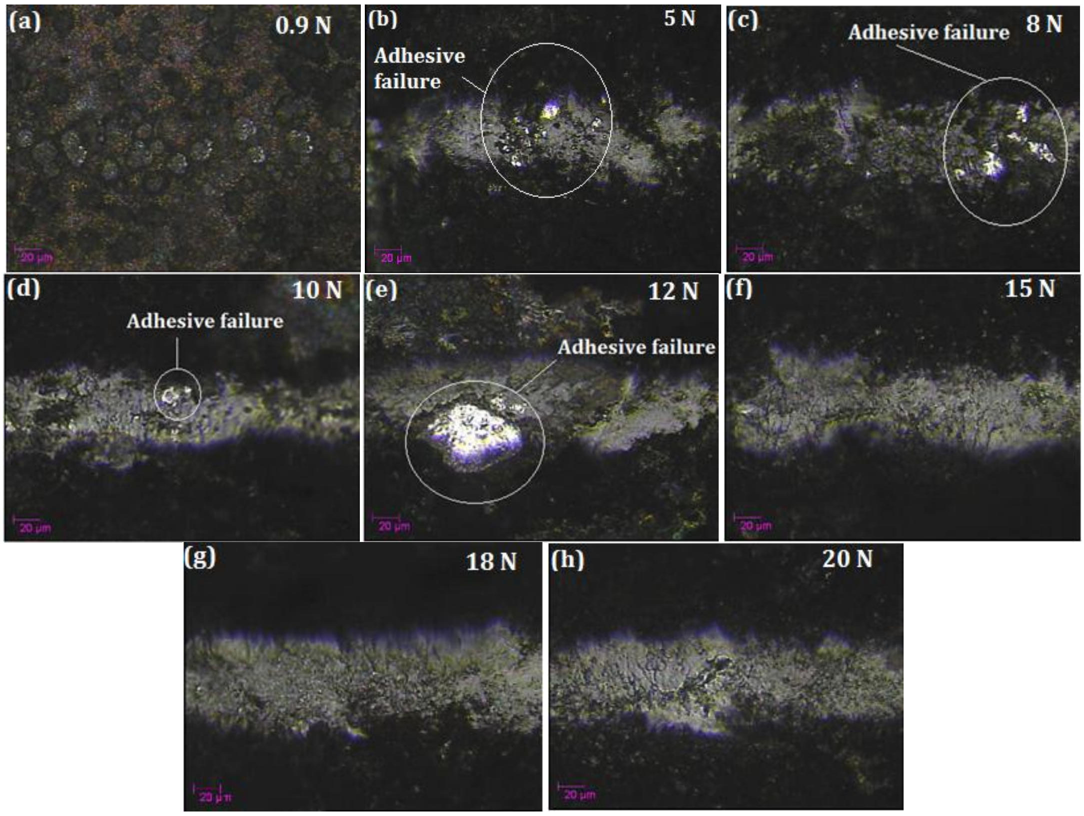

**Fig. 6.2.1** Optical microscopy images of the scratch track corresponding to different stages of loads, during scratch adhesion testing of the aluminum coated Fe9Cr1Mo steel after subjecting it to thermal oxidation treatment.

The optical images showed no major adhesive damage to the coating up to a maximum test load of 20 N. However, at a few locations on the scratch tracks, especially along the edges, partial adhesive delamination was noticed (Fig. 6.2.1b–e) which may be due to insufficient diffusion of aluminum atoms occurring at such spots.

The graphs of normal load and friction, acoustic emission and penetration depth, recorded during the scratch testing are shown in Fig. 6.2.2a, b and c, respectively. Large fluctuations in frictional force and coefficient of friction were observed during the course of movement of the indenter (Fig. 6.2.2a). This happened mainly due to higher roughness of the wet alumina blasted Fe9Cr1Mo steel substrate used for coating deposition. Further, in agreement with the adhesive failure seen along the scratch track at some locations (Fig. 6.2.1), there was appreciable acoustic emission, in the form of sharp peaks, detected by the acoustic sensor just after the indenter traversed a distance of 0.3 mm on the specimen (Fig. 6.2.2b). Moreover, around midway of the scratch track there was maximum acoustic emission (Fig. 6.2.2b) and this could probably indicate spallation occurring to brittle alumina phase of the coating. However, the acoustic emission decreased to a much lower value after the indenter attained a load of 14 N. This was attributed to the untransformed, ductile, aluminum exposed to the indenter after complete removal of the top oxide layer. Presence of untransformed aluminum just below the oxide layer was confirmed from the (111), (200) and (220) XRD reflections of the thermally oxidized specimen (Fig. 6.1.1). The load versus penetration depth curve shown in Fig. 6.2.2c did not show continuous increase in depth of penetration as the load increased progressively. This was again attributed to the uneven surface of the wet alumina blasted T91 steel substrate.

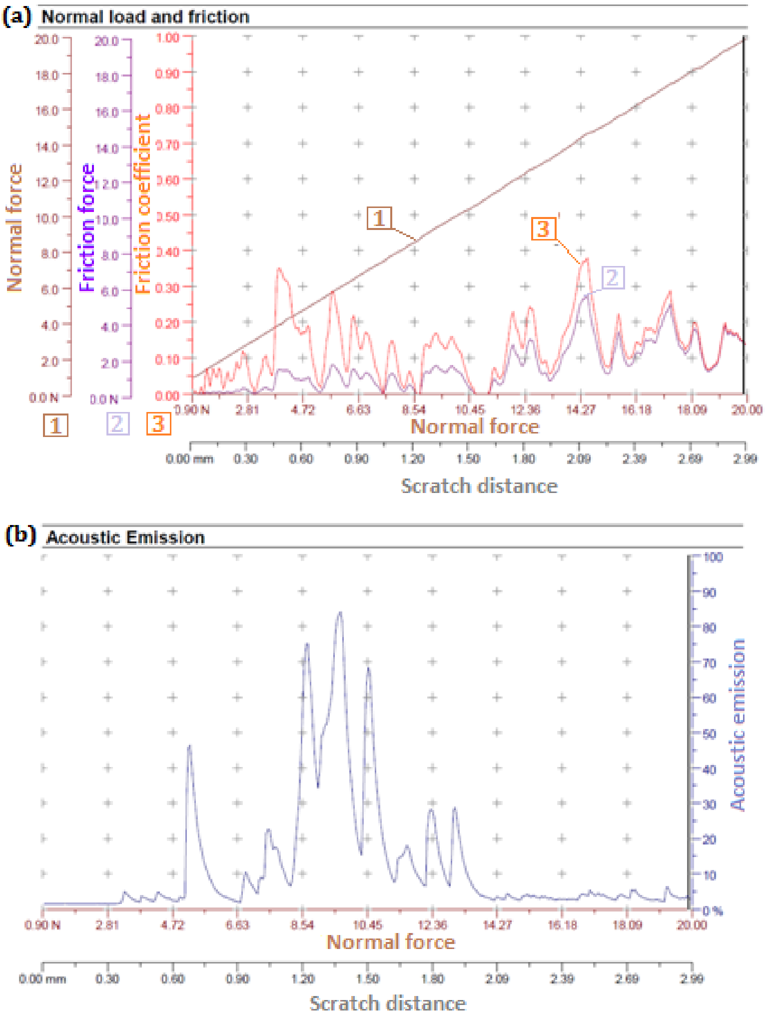

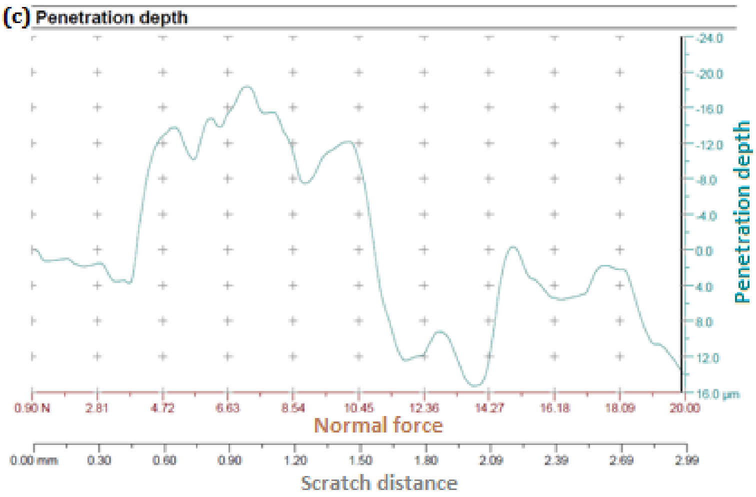

**Fig. 6.2.2** (a) Normal load and friction, (b) acoustic emission and (c) penetration depth curves recorded during scratch adhesion test of a thermally oxidized aluminum coating formed on Fe9Cr1Mo steel.

## 6.3 Anodization of electroplated aluminum in sulphuric acid

SEM image of the aluminum oxide layer formed by anodization of aluminum plated Fe9Cr1Mo alloy in 20 Vol.-% $H_2SO_4$ at 15V and for 15 min., as described in section 3.3, is shown in Fig. 6.3.1. The higher magnification image shown in the inset revealed that the anodized specimen had an uneven morphology with a less porous microstructure compared to the anodic aluminum oxide coatings formed on bulk aluminum specimens, reported earlier by various authors [179,180]. The conversion of aluminum to alumina could not be detected by XRD measurement of this specimen probably due to the formation of a very thin oxide layer. However, the incorporation of oxygen in aluminum after anodization was verified by EDS measurement, pattern shown in the inset of Fig. 6.3.1. The EDS analysis showed approximately 15 wt.-% O present in the anodized specimen. The reason for measured oxygen concentration being lower than that of the stoichiometric alumina was thought to be the very low thickness of the anodic film. It may be recalled that in EDS analysis the interaction depth of electrons in the specimen is up to the order of several micrometers.

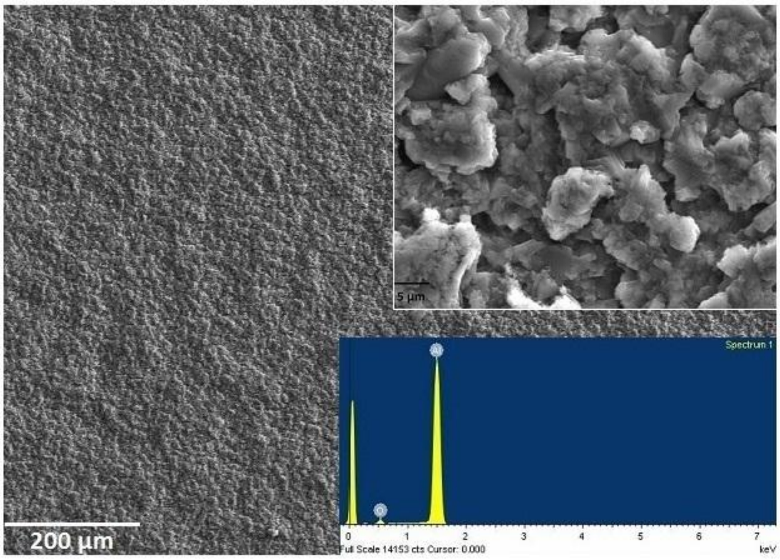

**Fig. 6.3.1** SEM image of a aluminum coating formed on Fe9Cr1Mo steel using $AlCl_3$ (98%)-EMIC (98%) ionic liquid bath and subsequently anodized in 20 Vol.-% $H_2SO_4$ at 15V and 4-5°C for 15 min. Inset shows higher magnification image and EDS spectrum shows incorporation of oxygen in aluminum after anodization.

## 6.4 Conclusions

The following conclusions were drawn from the present study.

- Electrodeposition of aluminum in $AlCl_3$-EMIC ionic liquids followed by a two-step thermal oxidation resulted in the formation of electrically insulative alumina coatings on wet alumina blasted Fe9Cr1Mo steel. Adherent coatings could not be obtained on a mirror polished substrate.
- Post deposition thermal oxidation of aluminum plated Fe9Cr1Mo steel in air leads to its outer layer transforming to amorphous alumina.
- Thermal oxidation of the aluminum plated Fe9Cr1Mo steel in air leads to the formation of $Fe_2Al_5$, $Fe_3Al$ and $AlCr_2$ intermetallics by reaction of aluminum with the substrate. These intermetallics were present at the interface between unreacted aluminum and substrate.

- Thermal oxidation conducted in two-steps leads to improved bonding of oxidized aluminum with Fe9Cr1Mo steel that could not be achieved by the single stage thermal oxidation.

# Chapter-7

# Properties of Alumina Coatings Formed by Anodization of Aluminum in Oxalic Acid

This chapter describes characteristics and properties of the alumina coatings formed on aluminum substrate by electrochemical oxidation or anodization. In this chapter, results of the experiments done on the anodization behaviour of aluminum in 10% oxalic acid, as discussed in section 3.4, are given. The experimental conditions are being mentioned here again for a quick recap. Aluminum sheets were anodized at room temperature using 10% oxalic acid at 10-30V for 1h-1h 20 min. The so formed aluminum oxide on aluminum base was studied in detail for thickness, crystal structure, morphology, chemical composition, topography, electrical resistivity, hardness, cohesive/adhesive strength and wear resistance using eddy current probe, XRD, FE-SEM, EDS and XPS, stylus based profilometer, 4-point probe, nanoindentation, micro scratch tester and wear tester, respectively. The experimental conditions were optimized to obtain hard, scratch and wear resistant coatings suitable for corrosion protection applications. Few anodization experiments were done using ultrasound assisted 10% oxalic acid bath at 90, 120 and 200W ultrasound power, 30V anodizing potential and 30 minutes duration and, surface morphology, topography and chemical composition of the resulting coatings were established.

## 7.1 Crystal structure and chemical composition of anodic alumina coatings

XRD measurements were conducted on the anodic alumina coatings formed on aluminum at different potentials, details given in section 3.4, to ascertain the associated change in crystal structure of the so formed oxide. The Bragg-Brentano XRD patterns of the aluminum specimens anodized at 20 V and 30 V are shown in Fig. 7.1.1a. It is clear that even after anodizing the reflections of metallic aluminum remained very intense in the pattern. The small peaks in Fig. 7.1.1a marked as ‘X’ belonged to the aluminum hydroxide ($Al(OH)_3$). However, these peaks did not appear consistently in both the 20 V and 30 V patterns. Further, there could not be found any peak pertaining to crystalline alumina. In order to reconfirm the XRD results GIXRD measurements were done on the aluminum specimens anodized at various potentials and the results are shown in Fig. 7.1.1b. In this case there are no peaks belonging to any crystalline phase and only one unresolved peak can be observed for every specimen. Therefore, it is clear that the aluminum oxide coatings formed on aluminum by anodizing aluminum in 10% oxalic acid at 10-30 V are amorphous. The formation of amorphous aluminum oxide coatings by anodizing has been widely reported by many authors [18,181,182]. The appearance of peaks of aluminum hydroxide in the Bragg-Brentano XRD pattern was due to atmospheric hydration of the anodized aluminum (The specimens were stored for a few days before carrying out the Bragg–Brentano XRD measurements).

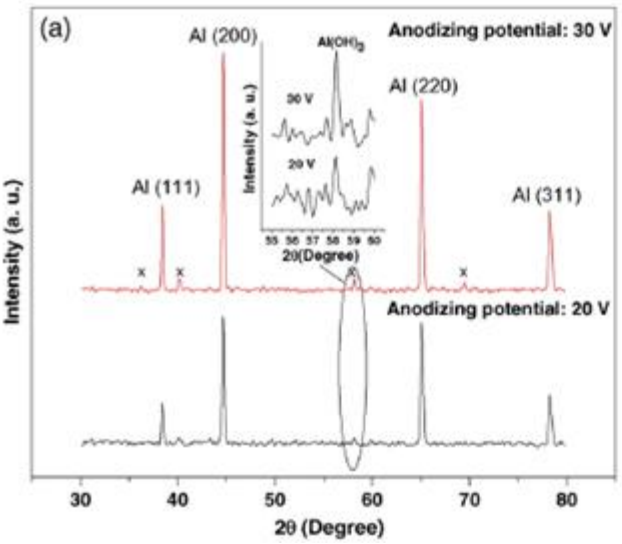

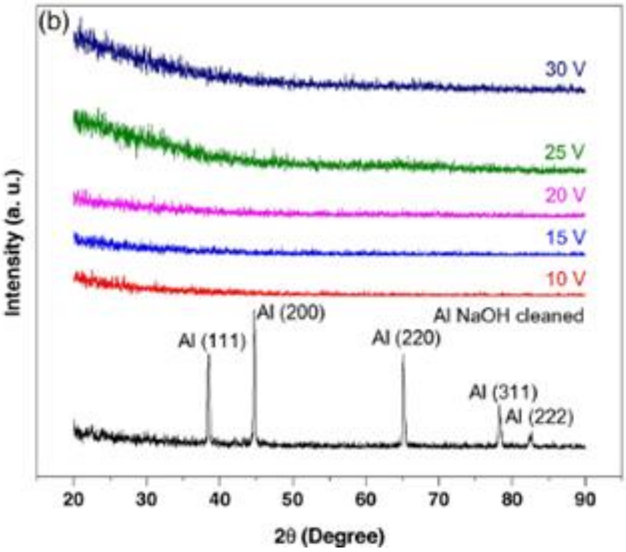

**Fig. 7.1.1** (a) Bragg-Brentano and (b) grazing incidence XRD patterns of the aluminum specimens anodized in 10% oxalic acid for 1h at different potentials. Inset in (a) shows the characteristic peak for $Al(OH)_3$.

The oxygen concentration of the anodized aluminum, measured by EDS (details given in section 3.4), is plotted as a function of anodizing potential in Fig. 7.1.2. There could be seen marginal increase in oxygen concentration as the anodizing potential was increased. Moreover, the minimum and maximum oxygen concentrations were 55.2 wt.-% and 56.6 wt.-%, respectively whereas, the calculated concentration of oxygen in alumina ($Al_2O_3$) is approximately 47.1 wt.-%. This indicates that the so formed alumina was hyper-stoichiometric. The EDS results of anodic alumina coatings reported in this work are in excellent agreement with the same reported by Chang et al. [183] who obtained amorphous alumina coatings by anodization of aluminum in aqueous ammonium adipate solution. Stojadinovic et al. [184] reported that with increasing current density more number of carboxylate ions got diffused into the growing oxide, leading to the increased oxygen concentration of the coating. Similarly, Mason [185] also reported that an increased amount of sulfate ions got incorporated into the aluminum oxide with increasing current density, for anodizing carried out in sulphuric acid solutions. Furthermore, Wang et al. [186] observed that during anodizing of aluminum in oxalic acid solutions, oxalate ions got incorporated into the oxide coating. Stepniowski et al. [187] showed that the rate of incorporation of impurity ions into the oxide coating increased with increasing anodizing potential. Therefore in the present work, the increase in concentration of oxygen in the aluminum oxide coating was attributed to the incorporation of impurities from the electrolyte.

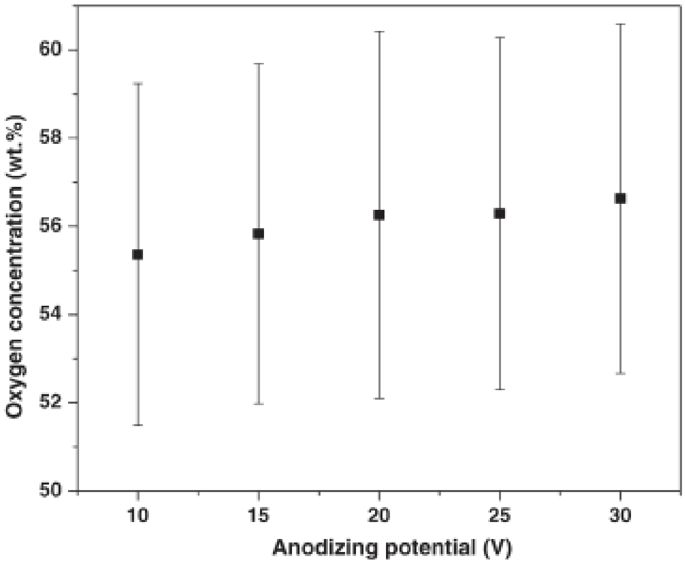

**Fig. 7.1.2** Measured oxygen concentration as function of potential for aluminum specimens anodized in 10% oxalic acid for 1h.

The thickness of the anodic coatings obtained on aluminum substrate at different potentials is listed in column 2 of Table 7.1. The table shows continuous increase in the thickness of the coating on increasing the potential. The increase in coating thickness with increasing anodizing potential can be attributed to the increase in current density. The increased current density resulted in fast reaction at anode with higher rate of oxygen evolution. This leads to the formation of thicker oxide at anode. Naief and Rashid [188] observed that the thickness of the anodic oxide coating is proportional to the applied potential. Moreover, they reported an exponential increase in the thickness of oxide coating with increasing anodizing potential [188]. Similarly, Araoyinbo et al. [189] reported increased rate of anodic reaction on account of the increase in applied potential.

**Table 7.1** Properties of anodic aluminum oxide coatings formed at various potentials

| Potential (V), time | Thickness (t)(μm) | $R_a$ (μm) | ρ (Ω.cm) | H (HV) (Calc.) | H (HV) (Meas.) | | τ (MPa) (Calc.) |
|---|---|---|---|---|---|---|---|
| | | | | | Highest | Avg. | |
| 10, 1h | 2.7±5% | 0.231±5% | - | - | - | - | - |
| 15, 1h | 6.2±5% | 0.291±5% | - | - | - | - | - |
| 20, 1h 20 min | 18.5±5% | 0.556±5% | - | - | - | - | - |
| 20, 1h | 12.9±5% | 0.349±5% | $8.4 \times 10^6$±10% | 448 | 432 | 347 | 23.6 |
| 25, 1h | 15.2±5% | 0.361±5% | $9.5 \times 10^7$±10% | 519 | 583 | 418 | 26.9 |
| 30, 1h | 19.7±5% | 0.593±5% | $1.7 \times 10^9$±10% | 683 | 657 | 520 | 34.6 |

## 7.2 Morphology, topography and coating thickness

Surface morphology of the aluminum specimens, anodized at various potentials (experimental and measurement details are given in section 3.4), as examined under FE-SEM, is shown in Fig. 7.2.1a–j. The FE-SEM images indicate formation of cellular microstructure. It is clear that the anodized surface has relatively smaller pores (Fig. 7.2.1a, c and e) at 10–20 V whereas comparatively uneven microstructure with larger pores can be seen for the anodizing conducted at 25 and 30 V (Fig. 7.2.1g and i). These features are more clearly visible in the higher magnification images (Fig. 7.2.1b, d, f, h and j). Moreover, for anodizing conducted at 25 and 30 V, the average diameter of the pores and the interpore distance can be estimated as close to 10 nm and 50 nm, respectively (Fig. 7.2.1h and j). The formation of large pores at higher anodizing potentials was attributed to the increased rate of dissolution of the oxide [188,190]. The electrochemical reaction occurring during dissolution of the anodic oxide is as per reaction 7.2.1 [190].

$$Al_2O_3(s) + 6H^+(aq.) \rightarrow 2Al^{3+}(aq.) + 3H_2O(l) \qquad (7.2.1)$$

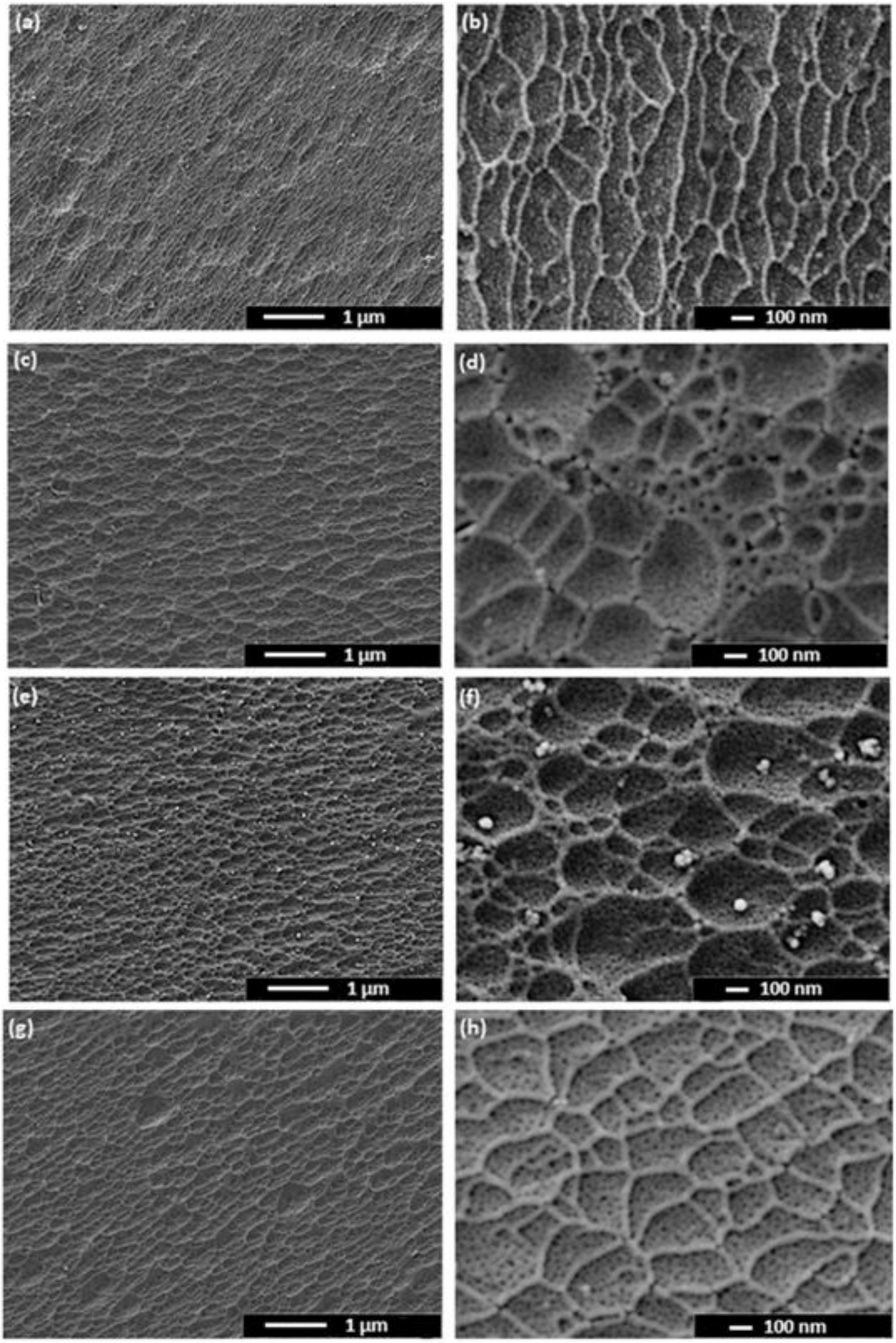
(a)
1 µm
(b)
100 nm
(c)
1 µm
(d)
100 nm
(e)
1 µm
(f)
100 nm
(g)
1 µm
(h)
100 nm

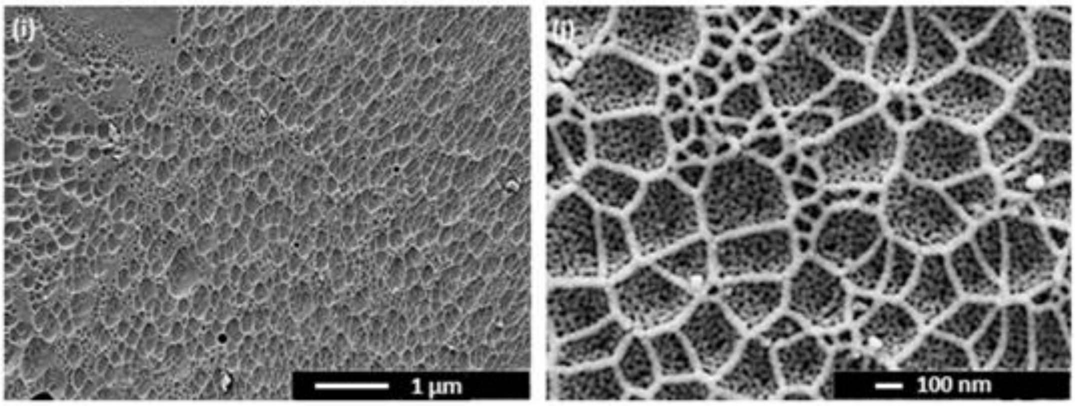

**Fig. 7.2.1** FE-SEM images of aluminum anodized in 10% oxalic acid for 1h at (a) 10, (c) 15, (e) 20, (g) 25 and (i) 30 V. (b), (d), (f), (h) and (j) are higher magnification images of (a), (c), (e), (g) and (i), respectively.

The thickness measured by eddy current method for the anodic oxide coating formed on aluminum at 30 V is about 19.7 µm, as can be seen from column 2 of Table 7.1. The cross-section view FE-SEM image of this coating (image not shown) revealed an average thickness of about 16.6 µm. This shows that the thickness measured by eddy current method is comparable and in agreement with the same measured by cross-section view SEM. However, the difference in the thickness measured by SEM and eddy current method is due to the parameters like surface roughness, surface curvature and contact pressure that affect the measurement by eddy current method [191].

3D surface profiles of the specimens anodized in the potential range of 10–30 V, as measured by the profilometer, are shown in Fig. 7.2.2a–e. The average roughness ($R_a$) of these specimens is given in the third column of Table 7.1. It is clear that the applied potential had a marked effect on the surface topography and roughness of the coatings. The specimens obtained at higher potentials showed uneven topography with higher average roughness (Fig. 7.2.2d and e), compared to the specimens obtained at lower potentials (Fig. 7.2.2a, b and c).

The higher potential resulted in faster dissolution of the anodized aluminum leading to the formation of uneven surface with large pores therefore more roughness.

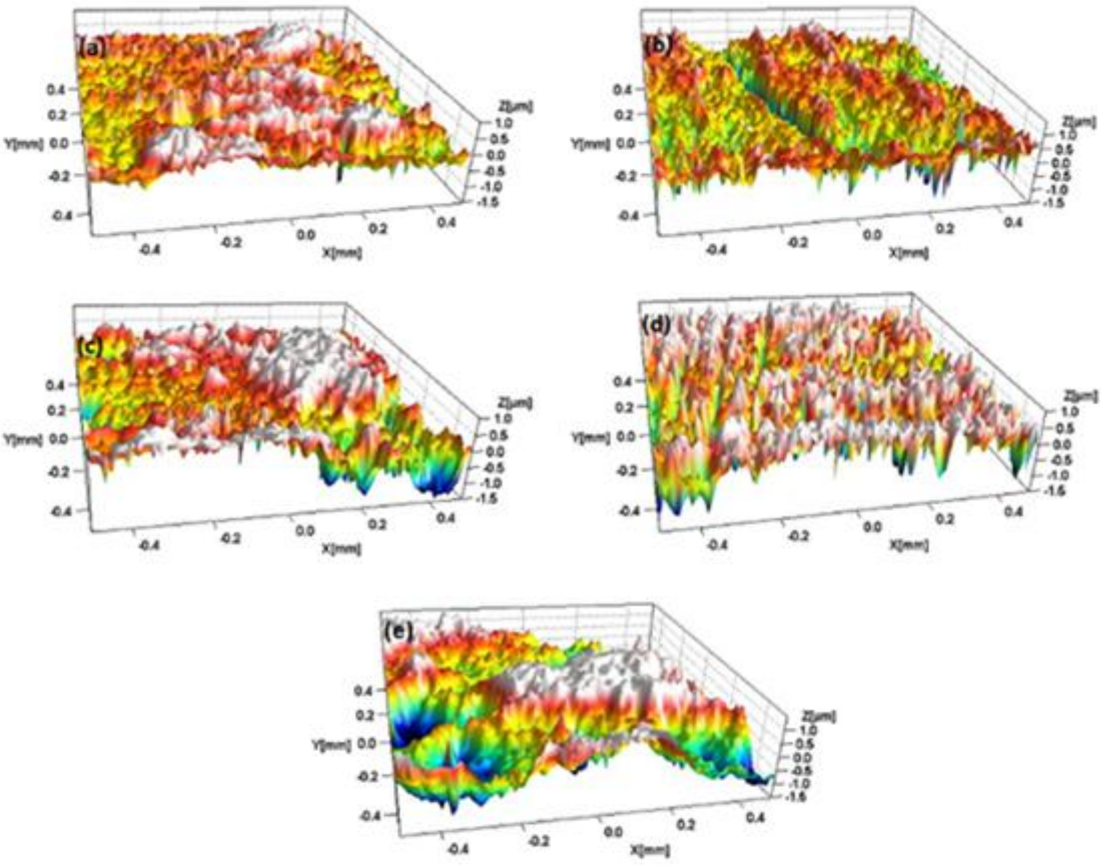

**Fig. 7.2.2** 3D surface profiles of aluminum specimens anodized in 10% oxalic acid bath for 1h at (a) 10, (b) 15, (c) 20, (d) 25 and (e) 30 V potential.

## 7.3 Electrical resistivity

The values of electrical resistivity of the aluminum specimens anodized at 20, 25 and 30 V, measured by four probe method (for measurement procedure details see section 3.4), are listed in the fourth column of Table 7.1. The oxide coatings obtained on aluminum substrate at potentials lower than 20 V were much thin and due to higher leakage current the resistivity of these coatings was not considered to be very accurate and therefore these values are not reported. The electrical resistivity has been found to increase significantly on increasing the anodizing potential. This was due to higher porosity of the coatings formed at higher anodizing potentials, evident from the FE-SEM images shown in Fig. 7.2.1. According to Zulfequar and Kumar [192], the electrical conductivity (σ) of a porous ceramic can be expressed as

$$\sigma = f_s\sigma_s + f_p\sigma_p \tag{7.3.1}$$

where, $\sigma_s$ and $\sigma_p$ are the electrical conductivity of the solid and the pore, respectively and, $f_s$ and $f_p$ are the volume fraction of the solid and the pore, respectively

Since $\sigma = \frac{1}{\rho}$ therefore, equation 7.3.1 can be written as

$$\frac{1}{\rho} = f_s\frac{1}{\rho_s} + f_p\frac{1}{\rho_p}$$

$$\text{Or, } \rho = \frac{\rho_s\rho_p}{f_s\rho_p + f_p\rho_s} \tag{7.3.2}$$

where, $\rho_s$ and $\rho_p$ are the electrical resistivity of the solid and pore, respectively

Since $\rho_p >> \rho_s$ therefore, equation 7.3.2 reduces to $\rho = \frac{\rho_s}{f_s}$ (7.3.3)

Equation 7.3.3 shows that for a more porous material (i.e. smaller $f_s$) the resistivity will be higher. From the electrical resistivity values listed in Table 7.1 (column 4) it can be deduced that the anodic coating is electrically insulative. However, the resistivity of anodic aluminum oxide coatings formed on aluminum was substantially lower than that of the pure alumina ($10^{14}$ Ω·cm) [193]. The reason for this anomaly may be the elements like Fe and Cu present in the aluminum. Moreover, in general, the properties of materials in the form of films and coatings are significantly different than the properties of materials in the form of bulk.

## 7.4 Scratch adhesion and microhardness

Optical images of the scratch impressions, left on the specimens anodized at 20, 25 and 30 V for 1 h, are shown in Figs. 7.4.1–7.4.3 (see section 3.4 for details of coating formation and scratch testing). Onset of parallel vertical cracks on the anodized aluminum surface at the beginning of the test, i.e. at normal load of about 1 N, are visible in Figs. 7.4.1a, 2a and 3a. On increasing the load further numerous vertical and horizontal cracks appeared in the coating formed on aluminum, as revealed in Figs. 7.4.1–7.4.3. Moreover, as the normal load is increased the cracks become wider. Cracks have also been found to propagate along both the edges of the scratch impressions. These features can be clearly observed in the SEM images shown in Fig. 7.4.4a–f. The cracks observed in the SEM images are about 5–7.5 μm wide and the coating appears to be crushed by the indenter in Fig. 7.4.4d. However, despite numerous cracks there was no adhesive delamination in the coating till 24 N load, in the case of anodic coatings formed on aluminum at 20 V (Fig. 7.4.1). Moreover, the load for adhesive failure was found to be significantly lower viz. 17.6 N and 11.7 N (Figs. 7.4.2f and 7.4.3d) for the coatings formed at 25 V and 30 V, respectively. This confirmed improved adhesive strength of aluminum oxide coatings formed on aluminum at a relatively low potential.

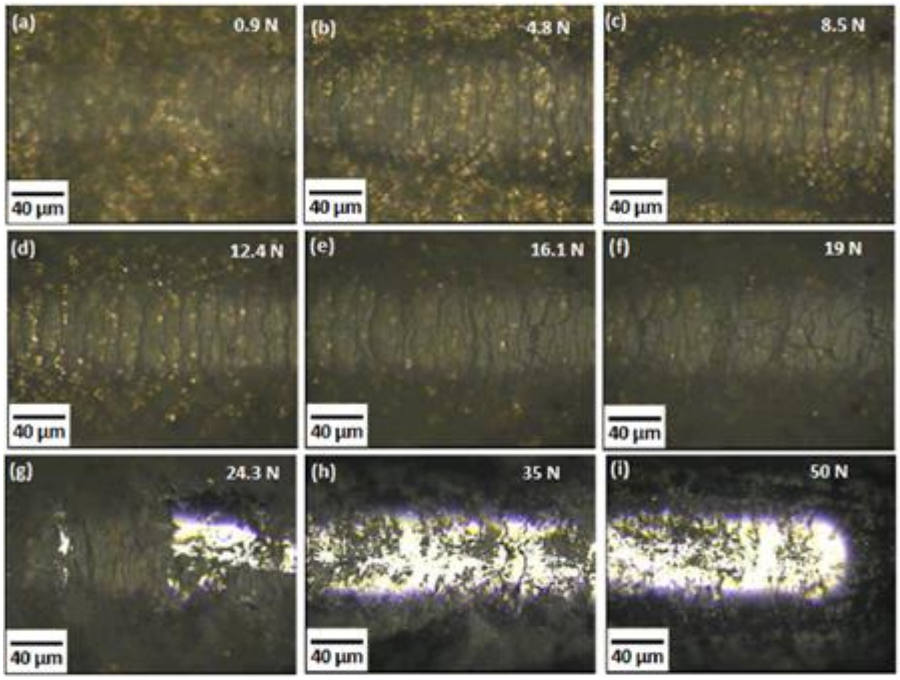

**Fig. 7.4.1** Optical microscopy images of scratch impressions on the aluminum specimen anodized in 10% oxalic acid at 20 V for 1 h, at different normal loads (marked on the images).

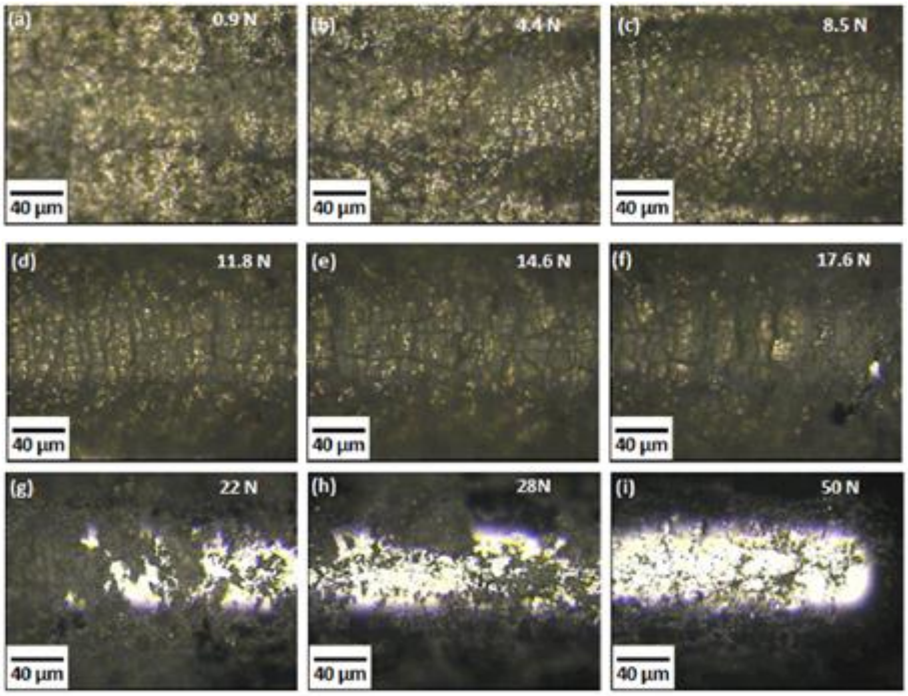

**Fig. 7.4.2** Optical microscopy images of scratch impressions on the aluminum specimen anodized in 10% oxalic acid at 25 V for 1 h, at different normal loads (marked on the images).

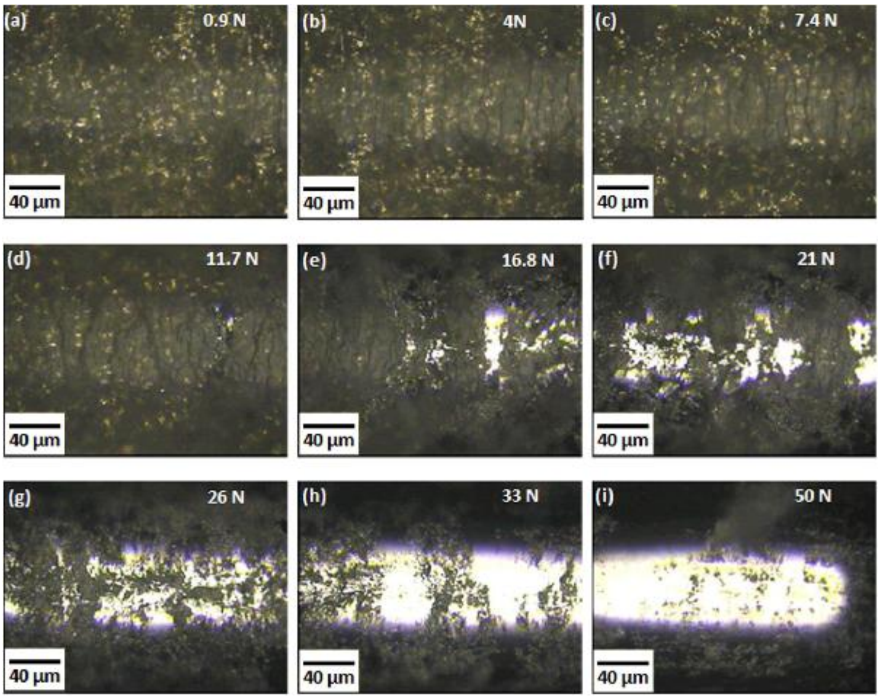

**Fig. 7.4.3** Optical microscopy images of scratch impressions on the aluminum specimen anodized in 10% oxalic acid at 30 V for 1 h, at different normal loads (marked on the images).

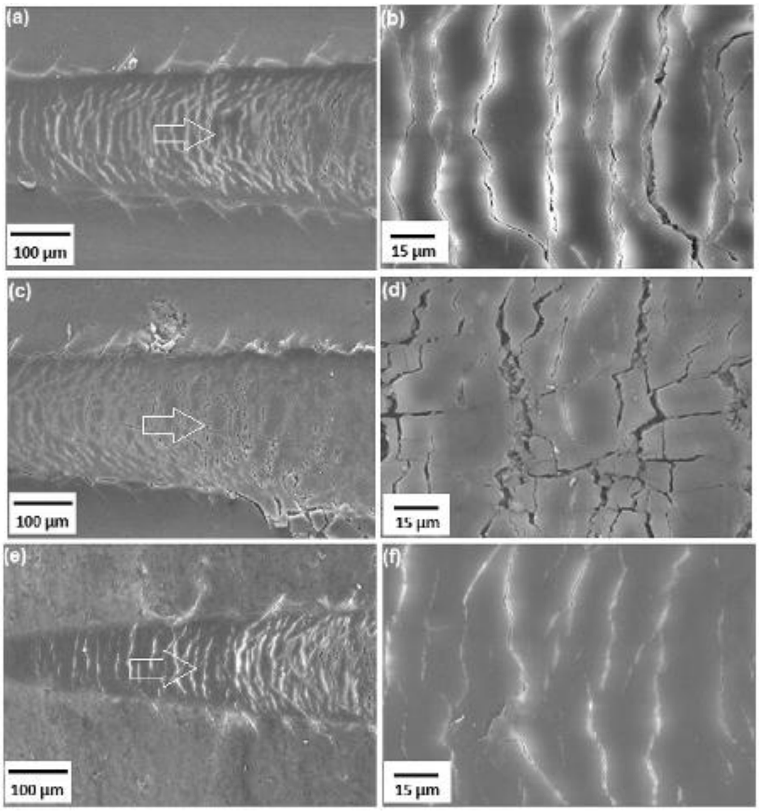

**Fig. 7.4.4** SEM images of scratch impressions on the aluminum anodized in 10% oxalic acid at (a) 20, (c) 25 and (e) 30 V. (b), (d) and (f) are higher magnification images of (a), (c) and (e), respectively.

Optical images of the scratch impressions left on the specimen anodized at 20 V for 1 h and 20 min are shown in Fig. 7.4.5a–i. By increasing the anodizing time the thickness and roughness of the oxide coating formed on this aluminum specimen was made close to that on the specimen anodized at 30 V (column 2 and 3, Table 7.1). From the shown optical images of the scratch impressions (Fig. 7.4.5a–i) the load for adhesive failure for this specimen was found to be about 19.1 N, which is close to that for the specimen anodized at 30 V. This established that the poor adhesive strength of the coating formed at a relatively high potential is mainly due to the increased thickness and roughness of the coating.

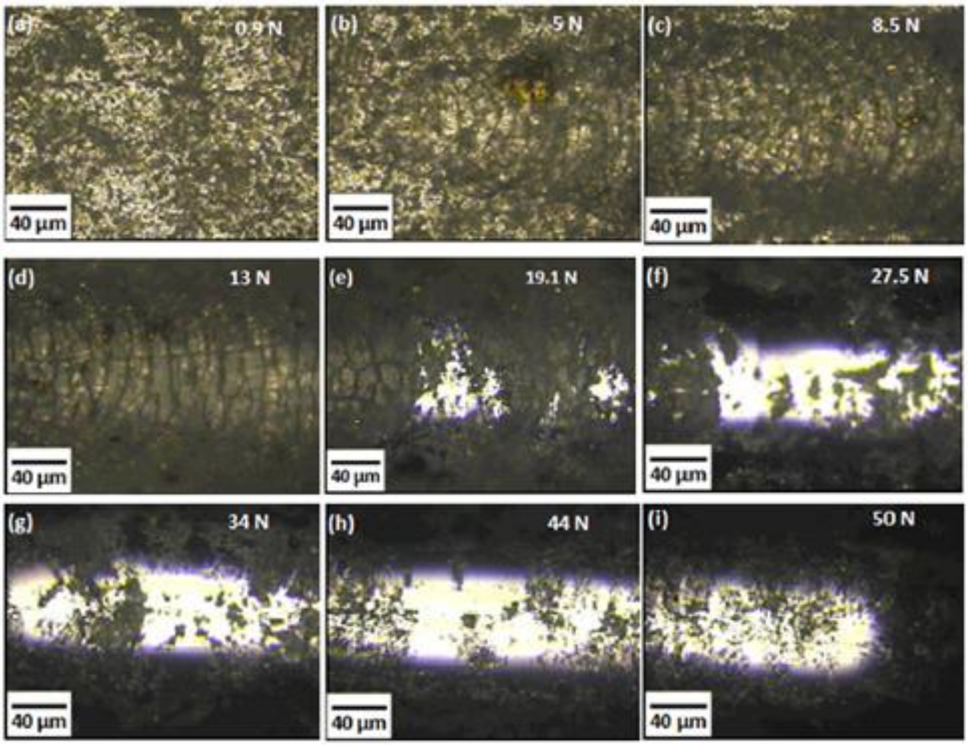

**Fig. 7.4.5** Optical microscopy images of scratch impressions on the aluminum specimen anodized in 10% oxalic acid at 20 V for 1 h and 20 min, at different normal loads (marked on the images).

The critical load for adhesive failure observed from the optical images (Fig. 7.4.1–7.4.3) is in agreement with the same obtained from the acoustic emission curves shown in Fig. 7.4.6. In the shown acoustic emission curves (Fig. 7.4.6), the first noticeable peak can be found at about 21 N, for the specimen obtained at 20 V (anodizing time 1 h), whereas, the corresponding peaks for the specimens obtained at 25 V and 30 V are found at 14.4 N and 10.5 N, respectively. It may also be noted that the acoustic peak indicating adhesive failure was noticed at a load higher than the load corresponding to adhesive delamination observed by optical examination of the scratch impressions (Fig. 7.4.1–7.4.3 and Fig. 7.4.6). This is due to the fact that acoustic emission starts only when cracks generate and propagate to an extent that a measurable acoustic signal is generated. Due to the same reason there was no detectable acoustic emission during cohesive failure of the anodic coatings formed on aluminum. The acoustic emission recorded during scratch testing of the specimen anodized at

20 V for 1 h and 20 min is shown in the bottom of Fig. 7.4.6. On comparing Fig. 7.4.5a–i and Fig. 7.4.6 it can be found that the acoustic emission observed in this case at 0–12 N is because of the wide cohesive cracks formed in the coating. Moreover, from Fig. 7.4.6, the load for adhesive failure for this specimen can be found to be about 15 N which is again close to that for the specimen anodized at 30 V.

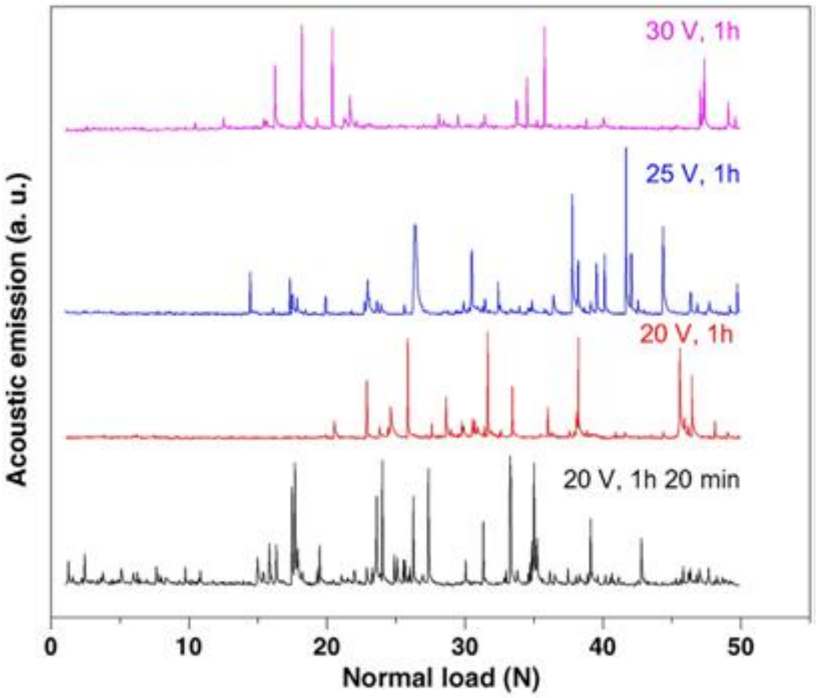

**Fig. 7.4.6** Acoustic emission curves recorded during scratch testing of the aluminum specimens anodized in 10% oxalic acid at different potentials and anodizing times.

Steinmann et al. [194] reported that the critical load for adhesive failure should be higher for thicker coatings. They argued that in order to plastically deform thick coatings higher load is required. In the present work, relatively thick anodic coatings were obtained on aluminum substrate at higher potentials. However, the critical load for adhesive failure was found to be low for such coatings. This discrepancy can be explained in terms of the following three factors; (i) the higher average roughness of the specimens obtained at higher potentials (column 3, Table 7.1), (ii) the increase in internal stresses in the coatings on increasing the anodizing potential [195] and (iii) the increase in hardness of the coating on increasing the anodizing potential (column 6, Table 7.1). From Figs. 7.2.1h, j and 7.2.2d, e it is clear that the surface of the coatings formed on aluminum at 25 and 30 V was highly uneven. The large asperities present on the specimen surface acted as notches ahead of the indenter tip thereby produced large stress concentration. This could result in adhesive failure of the coating at a relatively low load [195]. Further, there is volume expansion in the oxide formed at higher potentials [164]. This leads to generation of stresses at the oxide/metal interface [195]. This can also lead to failure of thick coatings formed on aluminum at a relatively low load. From Table 7.1 (column 6) and Fig. 7.4.7a–c it is evident that the higher anodizing potential leads to the formation of harder oxide. This makes the coating more brittle. The brittle oxide coating along with large pores present could fail at a comparatively low load. Vojkuvka et al. [52] also observed that the oxide coatings formed by anodization of aluminum in oxalic acid solutions are relatively brittle. The scratch test results (Figs. 7.4.1–7.4.3, 7.4.5 and 7.4.6) clearly demonstrate that the load for adhesive failure becomes similar for the specimens of same thickness and roughness (columns 2 and 3; Table 7.1) obtained at different potentials.

Chouanine et al. [196] reported that in microscratch testing of coatings, the expressions for surface hardness (H) and shear strength (τ) can be given as below

$$H = \frac{F_c}{\pi r^2} \tag{7.4.1}$$

$$\tau = \frac{F_c}{\pi r^2}\left[\frac{r}{\left(R^2 - r^2\right)^{\frac{1}{2}}}\right] \tag{7.4.2}$$

where, $F_c$: critical load for cohesive failure; R: radius of the indenter; r: half-width of scratch impression

Using equations 7.4.1 and 7.4.2 the values of surface hardness and shear strength were calculated for the aluminum anodized at 20, 25 and 30 V. These values are listed in the fifth and seventh columns of Table 7.1, respectively. In the sixth column of Table 7.1 the experimentally measured highest and five point average microhardness values are listed. The calculated values of surface hardness (converted into HV, for comparison) can be found to be in agreement with the experimentally measured values and also with the values reported in literature [197] for alumina coatings. Moreover, from Table 7.1 (column 6) it is clear that the higher anodizing potentials lead to the formation of harder coating on aluminum substrate. This is well supported by reduced size of the diagonals of the indenter impressions created in the specimens (Fig. 7.4.7a–c) during hardness measurement. Similarly, the calculated values of shear strength for anodized aluminum were found to be in agreement with the values reported in literature [197] for alumina coatings. The increase in surface hardness and shear strength of aluminum oxide coating with increase in anodizing potential is because of the decrease in pore density and increased level of stresses in the coating [198]. The anodized aluminum can be considered as equivalent to a hard oxide coating formed on the soft aluminum substrate.

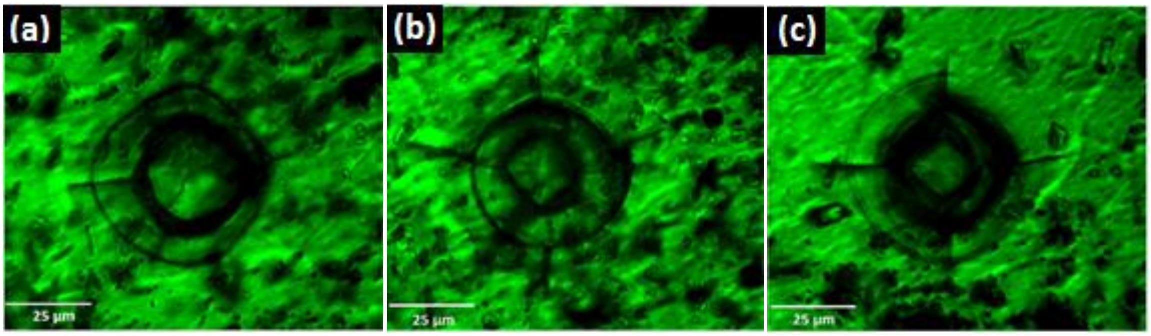

**Fig. 7.4.7** Optical microscopy images of the indentations created on aluminum specimens anodized in 10% oxalic acid for 1h at (a) 20, (b) 25 and (c) 30 V, during Vickers' hardness test.

Bull and Berasetegui [199] presented a very detailed and comprehensive review on the scratch testing of coatings. According to them [199], there are two mechanisms of scratch damage to a hard coating formed on a soft substrate. These mechanisms are buckling and wedge spallation. Buckling is observed in the case of coatings having thickness about 10 μm; whereas for much thicker coatings the commonly observed failure mode is wedge spallation [199]. However, according to Burnett and Rickerby [200], the following failure modes can happen during scratch testing of hard coatings: spallation, buckling, chipping, conformal cracking and tensile cracking. In the case of conformal cracking, cracks are caused by the generation of tensile bending moment in the coating pressed under the indenter [200]. Similarly, tensile cracks are caused by the frictional forces generated as the indenter progressed into the coating [200]. It is to be noted that the cracks formed by buckling are accompanied by the propagation of cracks outside the scratch edges [200]. On the other hand, the cracks formed by conformal cracking or tensile cracking remain confined within the scratch groove only [200]. The careful examination of the SEM images of scratch impression (Fig. 7.4.4a–f) suggests that the parallel curved cracks observed in the present work can be assigned to buckling, conformal cracking and tensile cracking. Buckling, in which plastic pile-up of coating takes place in front of the indenter, leads to the formation of curved cracks along the scratch track due to compressive stresses generated ahead of the moving indenter [199]. The mathematical expression for critical buckling stress ($\sigma_b$) for a planar interface is given by [201]

$$\sigma_b = \frac{1.22E_c}{1-\nu_c^2}\left(\frac{t}{R}\right)^2 \tag{7.4.3}$$

where, $E_c$: elastic modulus of the coating; $\nu_c$: Poisson's ratio of the coating; $t$: thickness of the coating; $R$: radius of the buckled region

## Calculation of load for buckling

If h is the actual depth of penetration of the indenter during scratch test, then with the help of Fig. 7.4.8, the approximate radius of the buckled region can be expressed as

$$R = \sqrt{R_0^2 - (R_0 - h)^2} \tag{7.4.4}$$

From the SEM image of scratch impressions the load corresponding to the first crack due to buckling was tracked to be about 3–4 N. Corresponding to this load the depth of penetration (h) of the indenter is about 15 μm (Fig. 7.4.9). Therefore, the radius of the buckled region is

$$R = \sqrt{200^2 - 185^2} \approx 76\,\mu\text{m} \tag{7.4.5}$$

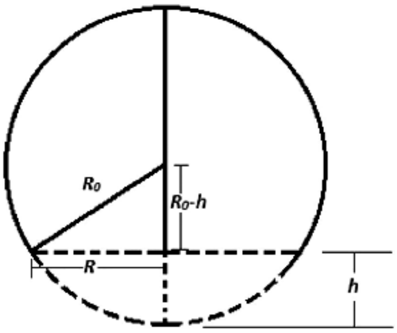

**Fig. 7.4.8** The schematic diagram of indenter tip used for calculating radius of the buckled region, during scratch testing of anodized aluminum.

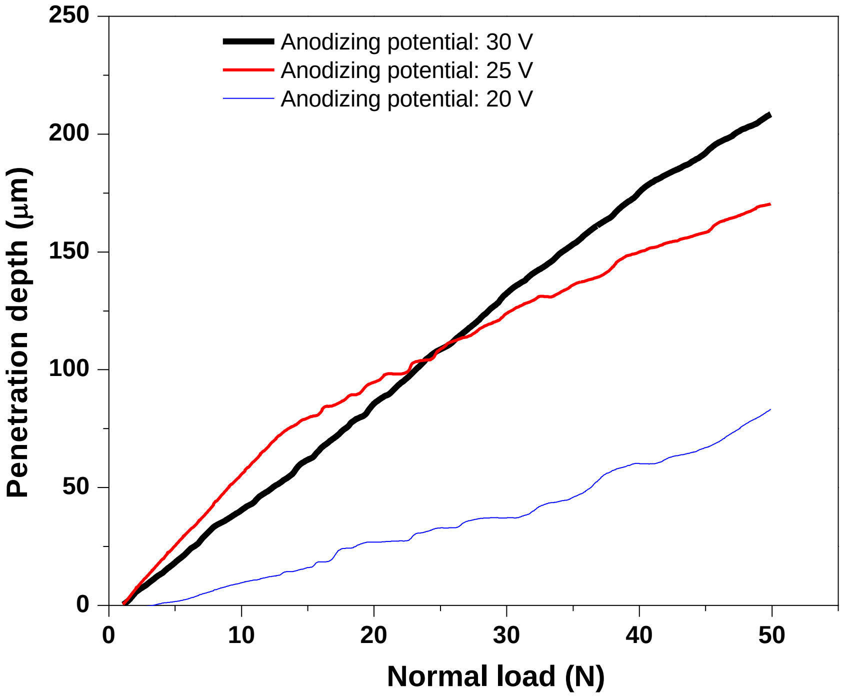

**Fig. 7.4.9** Depth of penetration as a function normal load for the aluminum specimens anodized in 10% oxalic acid for 1h at 20, 25 and 30 V, recorded during scratch test.

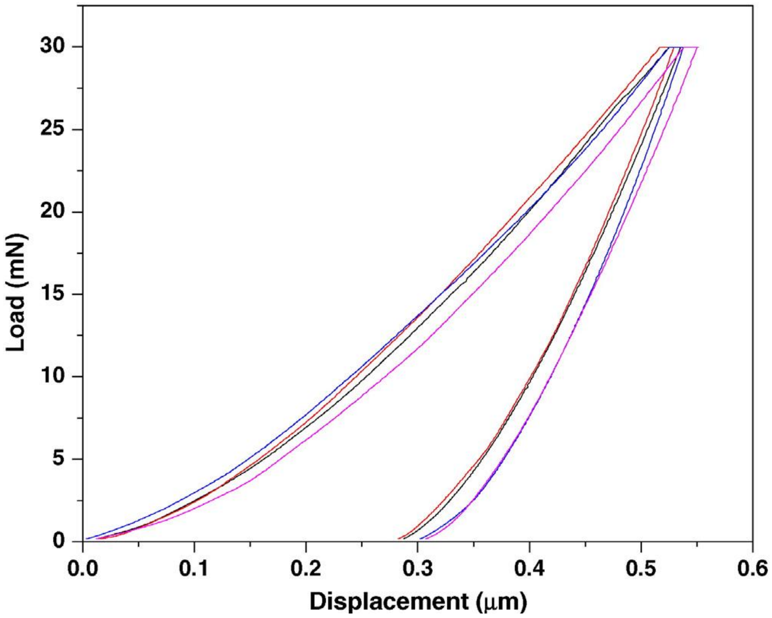

**Fig. 7.4.10** Load-displacement curves recorded during nanoindentation measurement on the aluminum specimen anodized in 10% oxalic acid for 1h at 30V.

With the help of Fig. 7.4.10 the value of elastic modulus for the anodic coating formed on aluminum at 30 V was estimated to be around 100 GPa. The literature reported value of Poisson's ratio for alumina is 0.22 [202]. The thickness of this coating measured by cross-section view SEM is 16.6 μm. On putting the values of all parameters along with the radius of buckled region into equation 7.4.3 the value of critical buckling stress for the coating formed on aluminum at 30 V was found to be 6.1 GNm$^{-2}$.

The actual area of the coating subjected to normal load by the indenter can be calculated as

$$A = \frac{\pi}{4} r^2 = \frac{\pi}{4}\left(30 \times 10^{-6}\right)^2 \approx 7 \times 10^{-10} m^2 \qquad (7.4.6)$$

where, *r* is scratch half-width corresponding to the first crack due to buckling

The value of *r* was obtained from the SEM images of the initial portion of the scratch impressions. Therefore, the force exerted by the indenter on the coating can be computed as

$$F = \sigma_b \times A = 4.3N \tag{7.4.7}$$

Although the calculated critical force for buckling is approximate only as it is very difficult and complex to predict the actual state of stress ahead of the moving indenter. Still, the value of critical force for buckling calculated using the equation suggested by Evans [201] agrees well with the experimentally observed value for the cracks formed by buckling, during scratch testing of the anodic aluminum oxide coatings formed on aluminum.

The depth of penetration of indenter recorded as a function of normal load, during scratch testing, on the coatings formed on aluminum at 20, 25 and 30 V is shown in Fig. 7.4.9. The depth of penetration includes both the elastic and plastic deformations occurring to the specimen. The elastic deformation is recovered as soon as the load becomes zero whereas the scratch impressions left on the specimens are due to the permanent plastic deformation. From Fig. 7.4.9, it can be found that the depth of penetration is much higher for the specimens anodized at higher potentials. It is seen that the load for adhesive failure was low for the coatings obtained at higher potentials (Figs. 7.4.1–7.4.3). Adhesive failure at a relatively low load could result in early interaction of the underlying aluminum to the indenter. The soft aluminum was easily penetrated by the indenter at increasing load. Therefore, the depth of penetration was more for the specimens anodized at higher potentials. The increased depth of penetration for the specimens anodized at higher potentials can also be due to the presence of large pores on the surface of the specimens, as it is easy to break a relatively porous surface.

The frictional force curves recorded during scratch testing of anodized aluminum specimens are shown in Fig. 7.4.11. It is clear that the frictional force curve corresponding to the specimen formed at 20 V is relatively smooth than the curves obtained for the specimens formed at 25 and 30 V. This happened due to the formation of smoother anodized surface at lower potentials, confirmed from the FE-SEM and surface profilometry images (Fig. 7.2.1

and Fig. 7.2.2, respectively). A relatively smooth surface permits easy movement of the indenter whereas on rough surfaces, the movement of indenter is restricted. At lower potentials (20 and 25 V), the oxide coating formed on aluminum had fine pores and also had lesser roughness (column 3, Table 7.1), therefore it allowed easier movement of the indenter (Fig. 7.4.11). For a more porous and rough coating obtained at a higher potential (30 V), the movement of indenter is more difficult (Fig. 7.4.11).

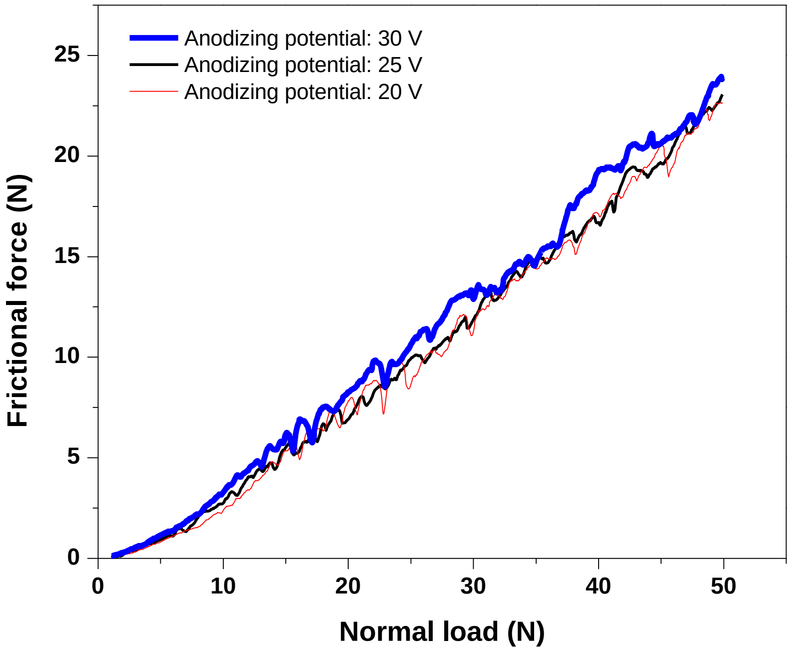

**Fig. 7.4.11** Frictional force curves recorded during scratch testing of the aluminum specimens anodized in 10% oxalic acid for 1h at 20, 25 and 30 V.

## 7.5 Wear and friction behaviour of alumina coatings

In this section, results of reciprocating-sliding wear test of the anodic alumina coatings formed on aluminum substrate in oxalic acid bath are highlighted. The descriptions of anodization and wear test procedure are given in section 3.4. In this study, the effects of anodizing potential used for obtaining the alumina coatings and the normal load applied during wear testing on wear volume, wear rate and coefficient of friction are described.

## 7.5.1 Reciprocating-sliding wear behaviour

Wear volume of the aluminum specimens anodized at various potentials, as a function of normal load applied during wear test, is shown in Fig. 7.5.1.1a. The profilometry image of a worn surface is shown in Fig. 7.5.1.1b. At a given normal load the wear volume can be found to decrease linearly as the anodizing potential is increased (Fig. 7.5.1.1a). This was attributed to the fact that at higher anodizing potentials the coating becomes harder. Therefore, the coating showed higher resistance against abrasion damage caused by the sliding counter body and so the wear volume decreased. Further, the wear volume can be found to increase linearly as the load during wear test was increased. This is in accordance with the formula given in literature for wear volume calculation as a function of normal load of wear measurement [203].

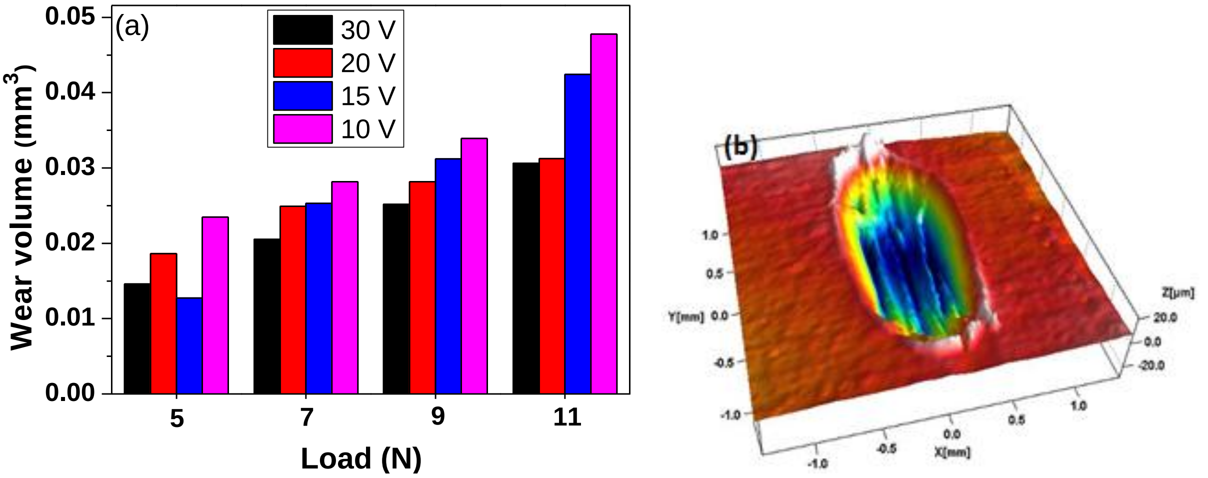

**Fig. 7.5.1.1** (a) Wear volume of the anodic alumina coatings formed on aluminum in 10% oxalic acid for 1h at different potentials, as a function of normal load, and (b) 3D profilometry image of a worn anodized aluminum specimen.

It may be noted that there is no specific unit to describe the wear resistance of a material. However, the reciprocal of wear volume loss is normally accepted as a measure of wear resistance. Thus, based on wear volume data the coating formed on aluminum substrate at a higher potential showed improved wear resistance (Fig. 7.5.1.1a). Similarly, the wear resistance decreased as the load applied during wear test was increased (Fig. 7.5.1.1a).

Wear rate of the aluminum anodized at various potentials, as a function of normal load, is shown in Fig. 7.5.1.2. Similar to the wear volume the wear rate was also found to decrease linearly as the anodizing potential was increased. However, in contrary to the wear volume the wear rate did not change appreciably on increasing the normal load and it remained nearly constant in the applied load range of 5–11 N. This was essentially due to the fact that in wear rate calculation the normal load of wear test and sliding distance are taken into account.

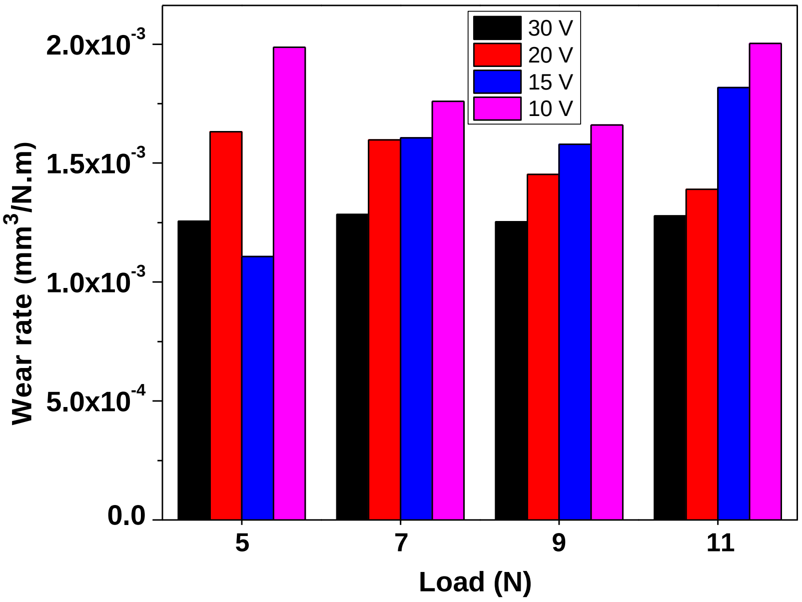

**Fig. 7.5.1.2** Wear rate of the anodic alumina coatings formed on aluminum in 10% oxalic acid for 1h, as a function of normal load and anodizing potential.

### 7.5.2 Friction behaviour

The coefficient of friction curves recorded during wear test of the anodized aluminum specimens at 5, 7 and 9 N loads are shown in Fig. 7.5.2.1a-c. It can be found that the coefficient of friction decreased as the load became higher. This was due to the fact that at a higher normal load the tangential shear force becomes higher. This leads to easy rupture of the surface asperities of the bodies in contact, preventing the interlocking of counter bodies, thus the coefficient of friction decreases. Further, the value of coefficient of friction was found to be marginally higher for the anodic coatings formed on aluminum at higher potentials (20 V and 30 V). This was attributed to the increased roughness of these coatings, as seen in section 7.2. A higher surface roughness leads to easy and firm interlocking of surface asperities of counter bodies and hence the coefficient of friction increases.

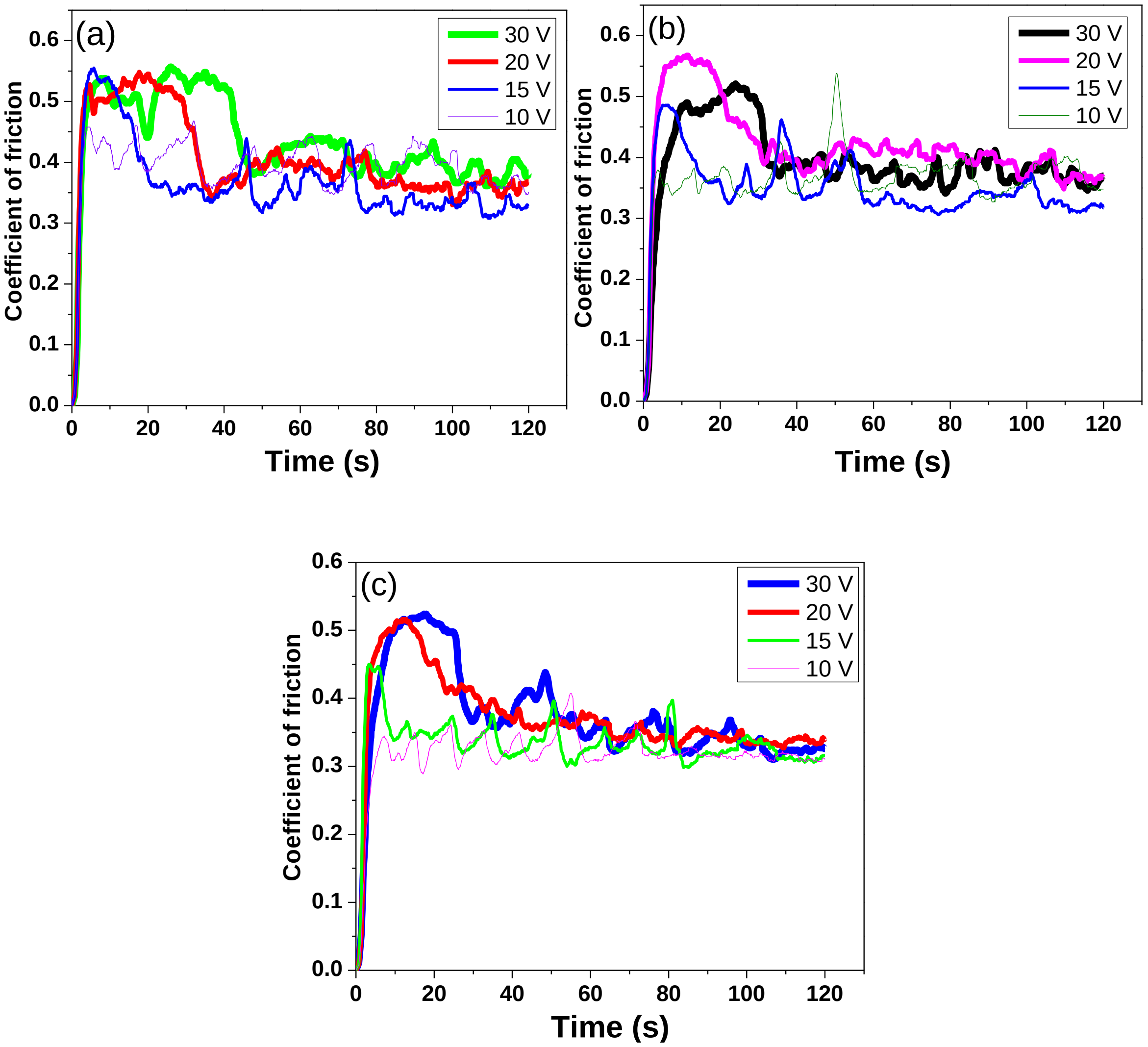

**Fig. 7.5.2.1** Coefficient of friction versus time curves recorded during wear test of the anodic alumina coatings formed on aluminum in 10% oxalic acid for 1h, at (a) 5, (b) 7 and (c) 9 N load.

## 7.6 Ultrasound assisted anodization of aluminum in oxalic acid

This section deals with the anodization behaviour of aluminum in ultrasound agitated 10% oxalic acid solution at a constant potential of 30 V, as described in section 3.4. In this section, the effect of ultrasound power (90, 120 and 200W) on the topography, roughness, morphology and chemical composition of the alumina coatings formed on aluminum substrate has been studied.

### 7.6.1 Effect of ultrasound power on topography

3D profilometry images of the aluminum specimens anodized at different ultrasound powers and 30V anodizing potential, as per description given in section 3.4, are shown in Fig. 7.6.1.1a-d. The average roughness of the specimens is plotted as a function of ultrasound power in Fig. 7.6.1.2a. A sharp decrease in the values of average roughness was found on increasing the ultrasound power. The coating formed without ultrasonic agitation had an average roughness of 471 nm whereas the roughness was around 243 nm when the power was kept at 200 W. The formation of smoother surface at a higher ultrasound power was also clearly verified from the line profiles recorded during profilometry (Fig. 7.6.1.2b). The formation of coatings with higher roughness, without application of ultrasound agitation, was attributed to the unclean and untidy deposition [204]. But, when ultrasound was applied the specimen surface became much clean and tidy that could promote the formation of a uniform coating with lower roughness [204]. Further, the increase in ultrasound power could result in increased vibration of specimen and electrolyte leading to a further decrease in roughness of the coating formed on aluminum.

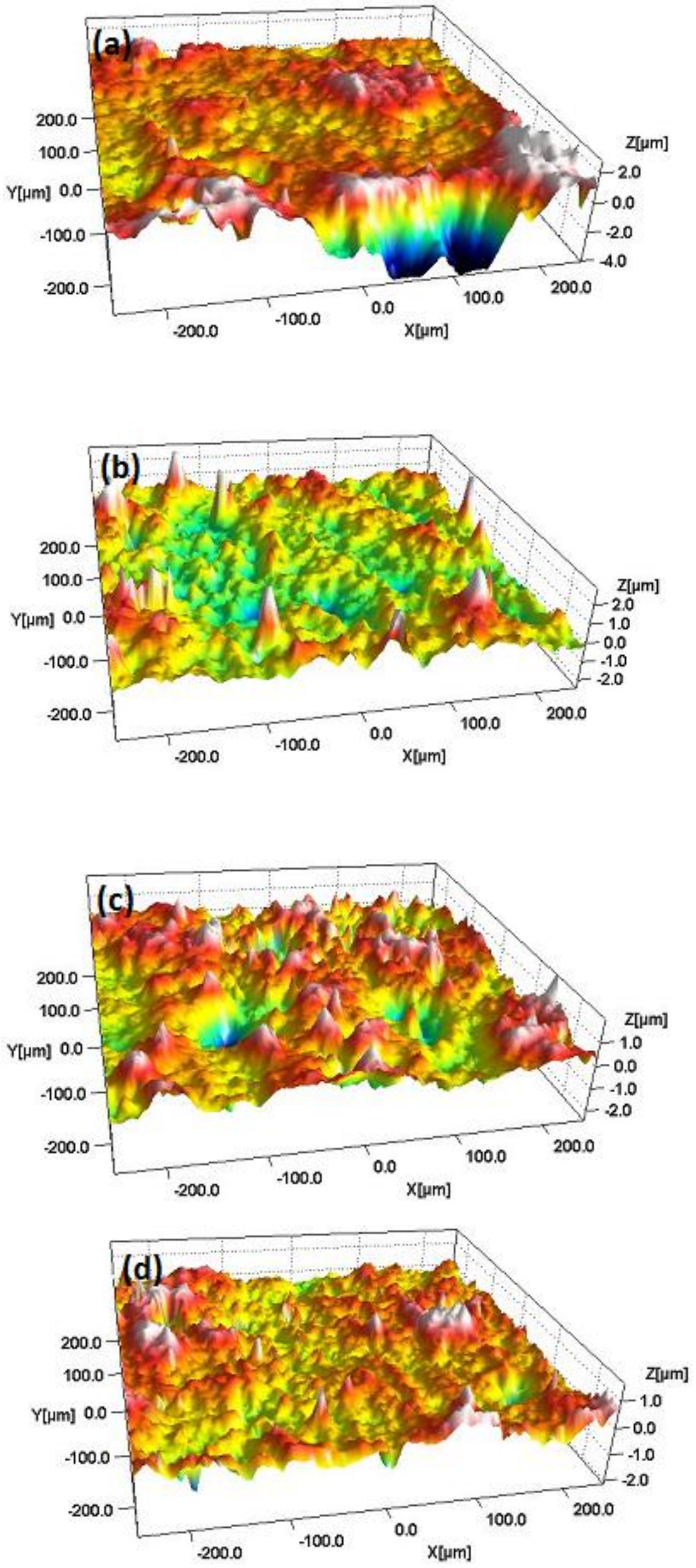

**Fig. 7.6.1.1** 3D surface profilometry images of the anodic alumina coatings formed on aluminum in 10% oxalic acid for 30 min at (a) 0, (b) 90, (c) 120 and (d) 200 W ultrasound powers.

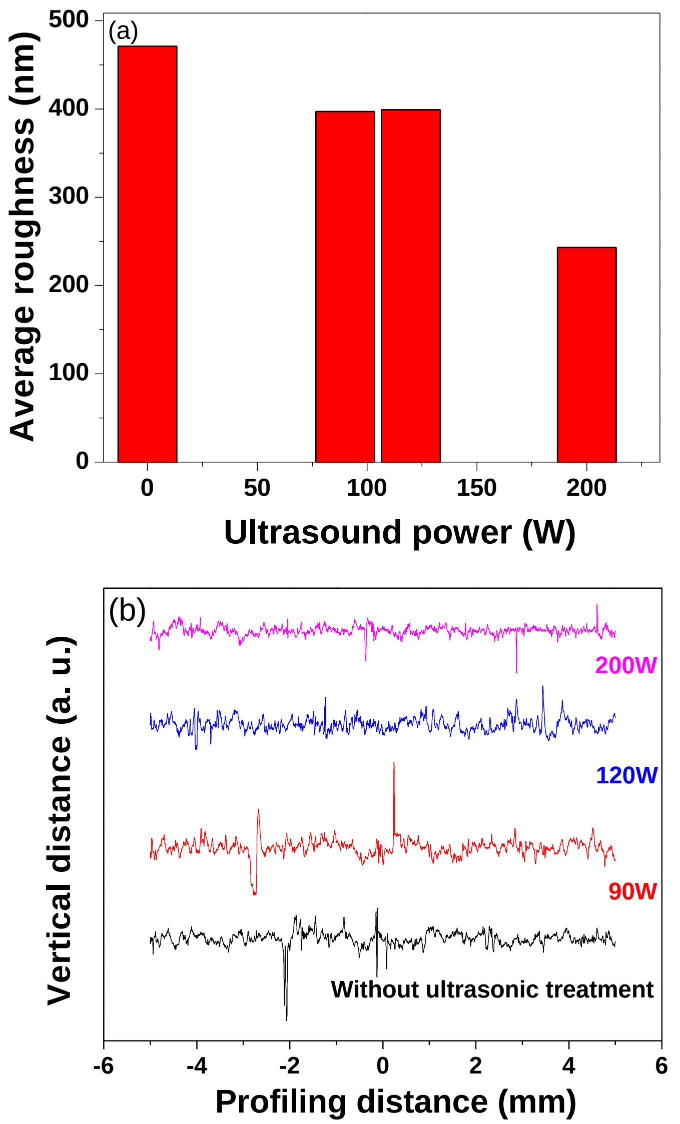

**Fig. 7.6.1.2** (a) Average roughness of the alumina coatings formed on aluminum in 10% oxalic acid for 30 min, as a function of ultrasound power employed during anodization, and (b) Profilometry line scans recorded on alumina coatings formed at different ultrasound powers.

### 7.6.2 Effect of ultrasound power on morphology of coatings

Morphology of the aluminum specimen, anodized in a quiescent 10% oxalic acid, as revealed by FE-SEM examination (for details see section 3.4), is shown in Fig. 7.6.2.1a. In Fig. 7.6.2.1b-d morphologies of the specimens anodized at various ultrasound powers are shown. An uneven morphology with several defects in the microstructure can be easily seen in the case of anodic coating formed on aluminum substrate without ultrasound (Fig.

7.6.2.1a). The formation of such defects was attributed to the nonuniform and unclean deposition. Fig. 7.6.2.1b–d shows the formation of much uniform coating when ultrasound agitation was used. This was again attributed to the clean and uniform deposition due to the vibrations resulting from ultrasonication. It may be noted that during aluminum anodization oxygen bubbles are formed on the anode surface due to outward diffusion of $O^{2-}$ ions from the barrier oxide layer [204]. During the progress of anodization these bubbles coalesced to form a large bubble and getting swept away from the cathode surface [204]. The removal of such oxygen bubbles hinders the growth of anodic layer since the $Al^{3+}$ ion moving route is blocked [204]. The application of ultrasound waves paves the way for easy detention of oxygen bubbles, facilitating uniform growth of the coating [204]. The FIB cut cross-section is shown for the coating formed on aluminum, without ultrasonication, in Fig. 7.6.2.1e. It can be seen that there are various perpendicularly arranged nanotubes. However, many tubes were not fully developed and some of them were found to be terminating before reaching the outer surface.

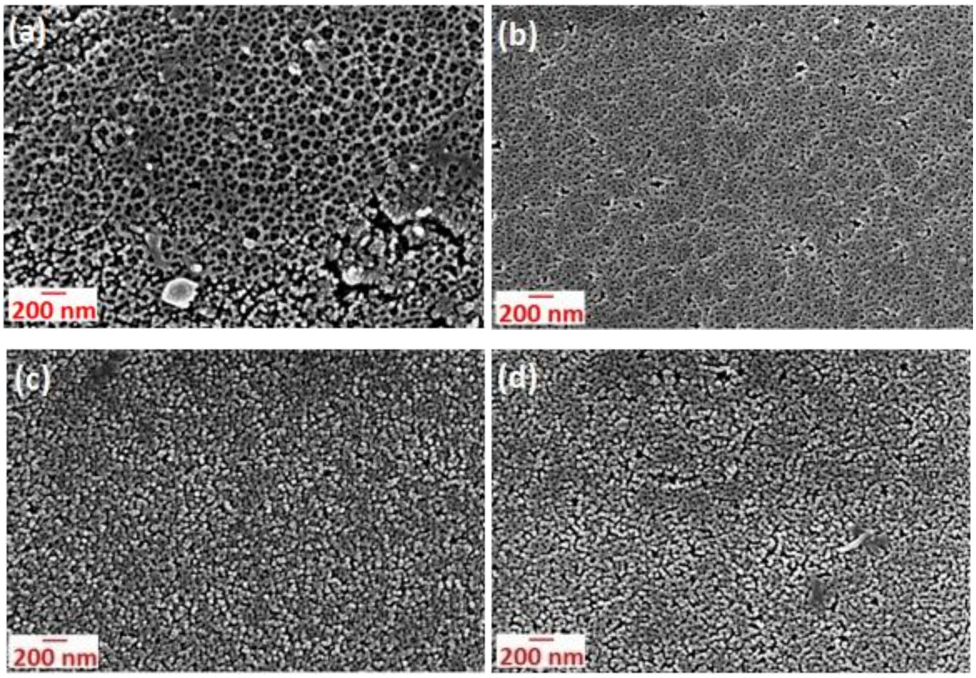

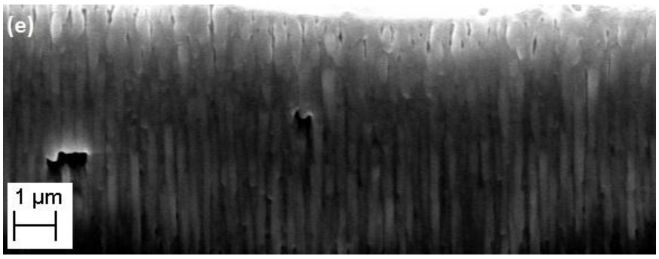

**Fig. 7.6.2.1** FE-SEM images of the aluminum specimens anodized in 10% oxalic acid for 30 min at (a) 0, (b) 90, (c) 120 and (d) 200 W ultrasound powers. (e) Represents the FIB cut FE-SEM cross-section view image of (a).

### 7.6.3 Effect of ultrasound power on chemical composition of coatings

The effect of ultrasound power on chemical composition of the anodic alumina coatings formed on aluminum was studied by XPS, as per details given in section 3.4. It should be kept in mind that XPS is a surface analytical technique which cannot probe more than 5-10 nm inside a given material. Therefore, the shown XPS data refer to the outermost anodic layers and it do not represent chemical composition of the bulk coating. XPS general survey spectra for the aluminum anodized at different ultrasound powers are shown in Fig. 7.6.3.1. There are peaks pertaining to Al-2p, Al-2s, C-1s, O-1s and O-Auger. The presence of carbon was assigned to the oxalate ions diffused into the oxide layers from the oxalic acid used for anodization [186]. The high resolution O-1s and Al-2p spectra are shown in Fig. 7.6.3.2a–d and Fig. 7.6.3.3a–d, respectively, for the anodic coatings formed at different anodization powers. The binding energy corresponding to the peaks associated with the resolved O-1s spectra and the Al-2p spectra clearly showed the formation of $Al_2O_3$. It may be noted that the likely sources of oxygen in the anodic aluminum oxide coatings are alumina and aluminum hydroxide related phases from aluminum side and $H_2O$, C-O-H, C=O, O-C=O, C-O species from the electrolyte side (oxalic acid). In the present work, the XPS O-1s spectra of anodic coatings could be resolved into peaks pertaining to $Al_2O_3$ and C=O phases. This was based on the best fitting of experimentally obtained data. The quantitative analysis of XPS measurement is summarized in Table 7.6. It was found that the coatings formed without ultrasonication were stoichiometric and, application of ultrasonic agitation during anodization resulted in decreased oxygen concentration of the coatings. This was attributed to the fact that, as mentioned earlier, due to vibration caused by ultrasound agitation of the bath the oxygen bubbles formed on the anode surface are swept away quickly, therefore the $Al^{3+}$ movement path for the growth of barrier layer becomes hindered [204]. This could decrease the oxygen concentration of the coatings. However, at 200W the oxygen concentration was found to be slightly on the higher side, which may be because of the increased bath temperature due to intense ultrasound agitation. The bath temperature measured after anodizing was approximately 50 °C.

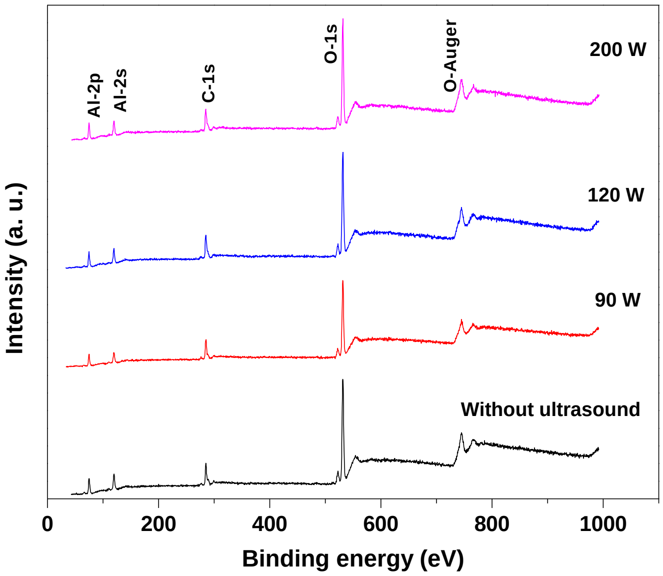

**Fig. 7.6.3.1** General survey XPS-spectra of the anodic alumina coatings formed on aluminum in 10% oxalic acid for 30 min at different ultrasound powers.

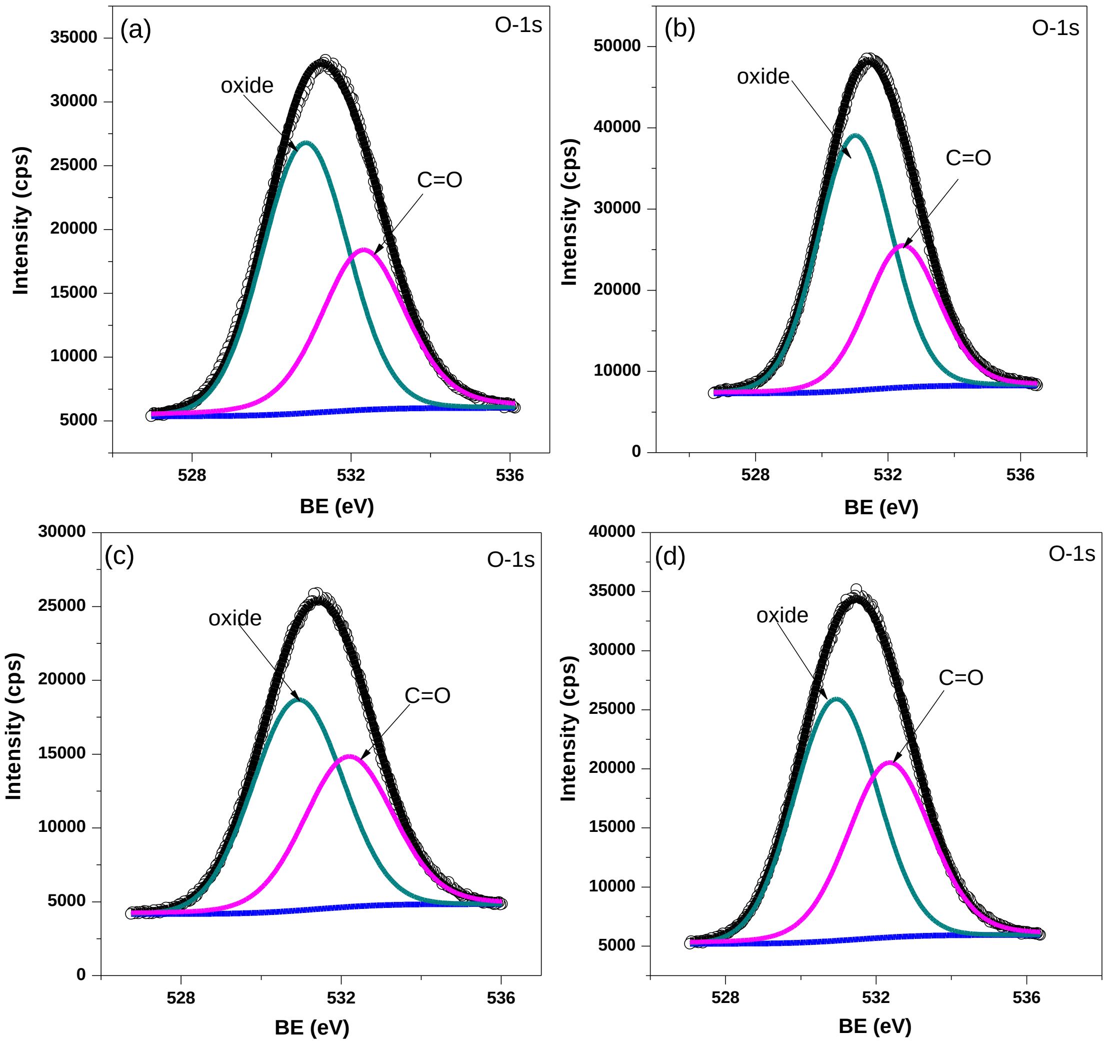

**Fig. 7.6.3.2** Resolved O-1s spectra of the alumina coatings formed on aluminum in 10% oxalic acid bath for 30 min at (a) 0, (b) 90, (c) 120 and (d) 200 W ultrasound powers.

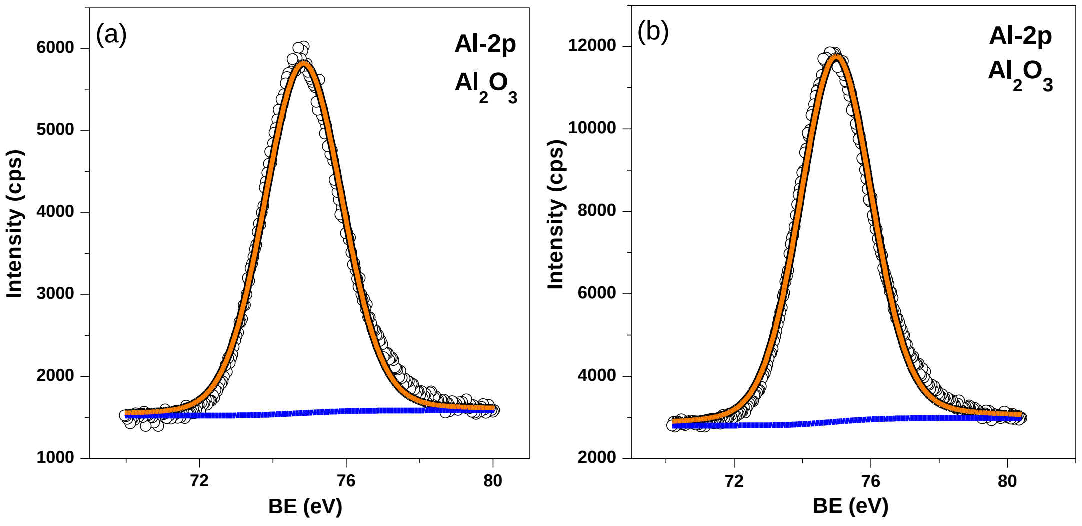

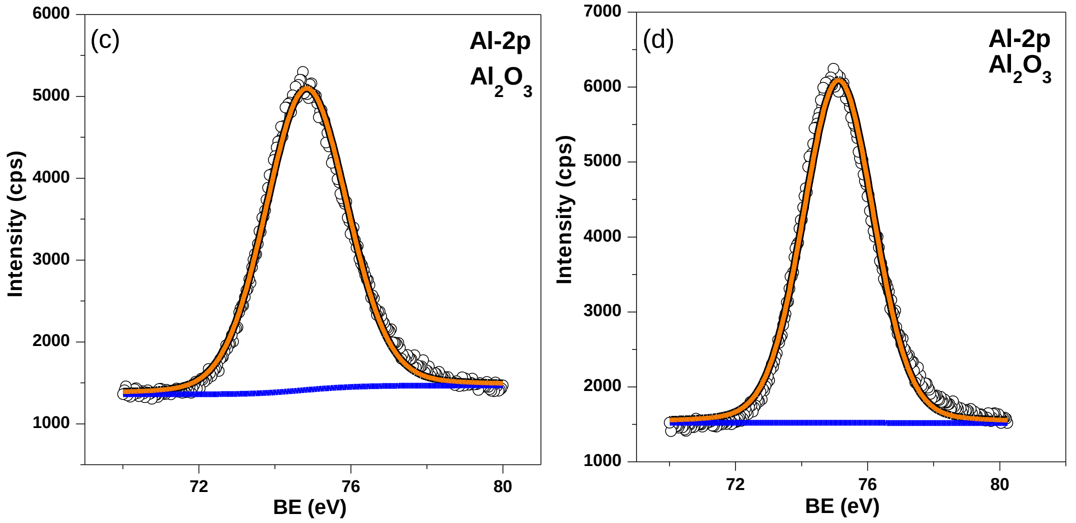

**Fig. 7.6.3.3** Resolved Al-2p spectra of the alumina coatings formed on aluminum in 10% oxalic acid bath for 30 min at (a) 0, (b) 90, (c) 120 and (d) 200 W ultrasound powers.

**Table 7.6** XPS derived chemical composition and stoichiometry of anodic alumina coatings

| **Ultrasound power (W)** | **O (at.-%)** | **Stoichiometry** |
|---|---|---|
| 0 | 61.6 | $AlO_{1.60}$ |
| 90 | 53.7 | $AlO_{1.16}$ |
| 120 | 55.9 | $AlO_{1.27}$ |
| 200 | 59.0 | $AlO_{1.43}$ |

## 7.7 Conclusions

The following conclusions were drawn from the present study

- Anodization of aluminum in 10% oxalic acid at 10-30 V potential leads to the formation of amorphous alumina coatings on aluminum substrate.
- Higher anodizing potential leads to the formation of porous and rougher coatings. Also, at higher potentials the coating contained a slightly higher proportion of oxygen.
- Although the anodized aluminum had sufficiently high value of electrical resistivity, the electrical resistivity was significantly lower than that of the pure alumina reported

in literature. Also, the resistivity was found to increase on increasing the anodizing potential.

- Higher anodizing potential leads to the formation of harder coating.
- Anodized aluminum showed the onset of horizontal and vertical parallel cohesive cracks during scratch testing at a load of about 1N. However, the load for adhesive failure was found to increase significantly on decreasing the potential during anodization.
- Coating thickness had a strong influence on roughness and adhesion.
- Average roughness and porosity had a significant impact on the adhesion of coatings.
- The anodic coatings formed on aluminum at higher potentials had improved wear resistance.
- Ultrasonic agitation during anodization leads to the formation of smoother aluminum oxide coatings on aluminum.
- The power of ultrasound agitation had strong influence on the chemical composition of the coatings. The coatings formed at a higher power were found to contain lesser oxygen.

# Chapter-8

## Characteristics of Anodic Alumina Coatings Formed in a Mixture of Oxalic Acid and Citric Acid

This chapter deals with the results of the experiments conducted on anodization behaviour of aluminum in mixed solutions of oxalic acid and citric acid, as described in section 3.5. In this chapter, the effect of two important anodizing parameters namely, bath concentration and applied potential on the crystal structure, chemical composition, surface morphology and porosity of the alumina coatings formed on aluminum substrate has been investigated. For a quick recap the experimental conditions are summarized here again as follows. Aluminum sheets were anodized at 20-70Vfor 1h in mixed solutions of oxalic acid and citric acid for total acid concentrations amounting to 5g oxalic acid and 5g citric acid to 35g oxalic acid and 35g citric acid. In such experiments the ratio of oxalic acid to citric acid was kept constant at 1:1 and the volume of solution was also fixed at 250 ml. The resulting aluminum oxide coatings on aluminum base were analyzed by XRD, XPS and FE-SEM.

### 8.1 Crystal structure of anodic alumina coatings

XRD measurements of the aluminum specimens after anodizing them at the maximum potential of 70 V using solutions of lowest and saturation level of acid concentrations were done to identify the effect of bath concentration on the crystal structure of the anodic alumina coatings. The reason behind selecting the maximum potential for specimen preparation for XRD studies was that the crystallinity of anodic metal oxides is expected to be better at higher potentials. The details of coating preparation and XRD measurements are given in section 3.5.

XRD patterns of the aluminum anodized at 70 V using mixed solutions of oxalic acid and citric acid of two different acid concentrations are shown in Fig. 8.1.1. There can be found (111), (200), (220), (311) and (222) peaks, all pertaining to metallic aluminum only. Further, there were no peaks belonging to crystalline alumina. This could indicate that the so formed oxide on aluminum was amorphous. Moreover, no new peak was found on increasing the total amount of acid from 10g to the maximum soluble amount of 70g. This showed that the strength of anodizing medium has no relation with the formation of crystalline or amorphous oxide. It may be noted that the alumina coatings formed by anodization technique are mostly of amorphous nature under un-annealed conditions. Therefore, the XRD results shown in this work are in line with the same reported previously in literature [18,181,182].

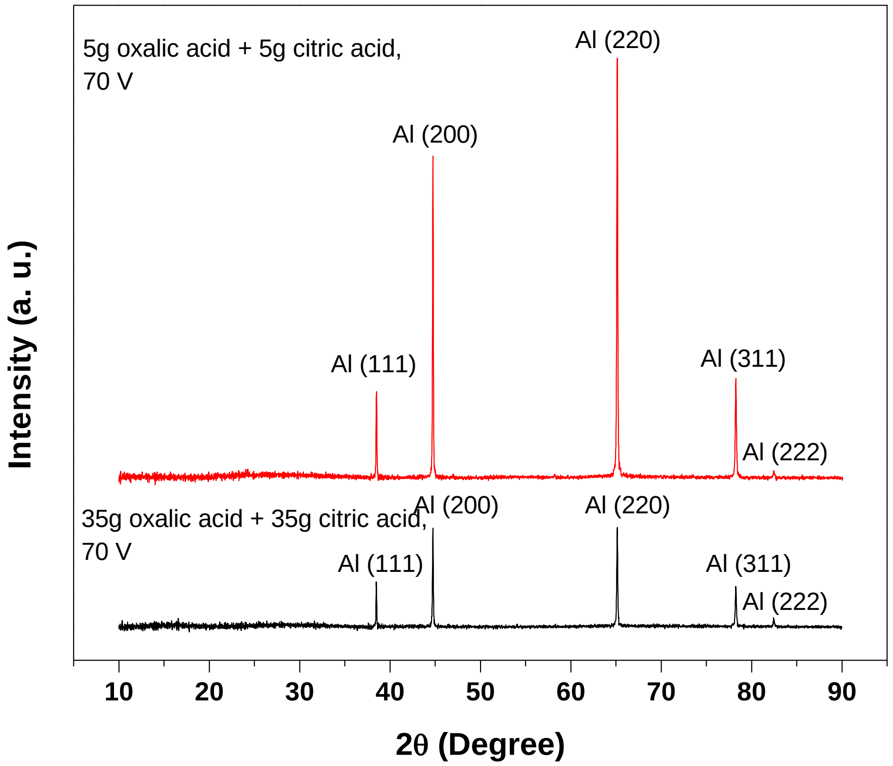

**Fig. 8.1.1** XRD patterns of the alumina coatings formed on aluminum substrate by anodization of aluminum at 70V, using baths of two different concentrations of oxalic acid and citric acid.

## 8.2 Surface morphology and porosity

FE-SEM examinations were conducted on the anodic alumina coatings formed on aluminum using solutions of various acid concentrations and applied potentials, as per details given in section 3.5, to identify their effect on morphology and porosity of the coatings. Fig. 8.2.1a-f shows the FE-SEM images of the anodic aluminum oxide coatings formed on aluminum in a mixed solution of 35g oxalic acid and 35g citric acid, in the anodizing potential range of 20–70 V. There can be found vast difference in morphology of the coatings. The coatings formed in the potential range of 20–50 V showed stripe type morphology with pores formed in between the ridges of the stripe (Fig. 8.2.1a–d). Further, the stripes were oriented randomly up to the anodizing potential of 40 V (Fig. 8.2.1a–c). However, at 50 V there can be seen the formation of nearly parallel stripes having much less gap between the ridges. Moreover, at 60 V the tendency to form stripe type morphology was found to be diminished and finally, at 70 V the stripe type morphology was completely replaced by uniform morphology showing the formation of pores of various shapes. The stripe type of morphology for anodic aluminum oxide coatings has been observed by several authors previously [115,205] however, no satisfactory explanation has been given for the same. The most likely reason for variation in morphology was sought as the pre-treatment induced differences in topography of the aluminum substrate that resulted in variation in field-assisted-dissolution of the oxide during anodization. Further, at a relatively high potential, the substrate surface topography related effects becomes insufficient to form a stripe type of morphology, due to higher dissolution of the anodic oxide.

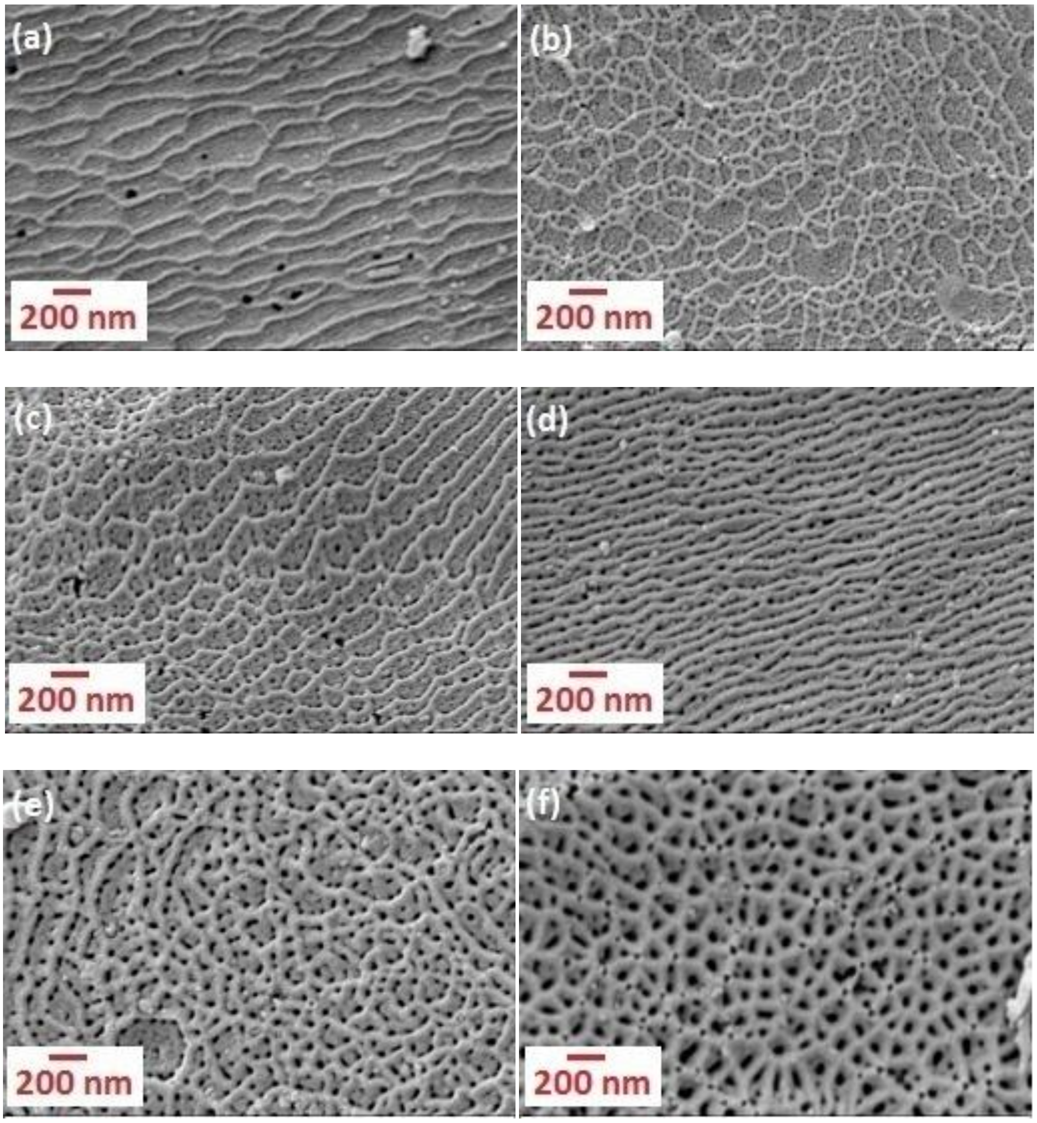

**Fig. 8.2.1** FE-SEM images of the anodic alumina coatings formed on aluminum in a mixed solution consisting of 35g oxalic acid and 35g citric acid at (a) 20, (b) 30, (c) 40, (d) 50, (e) 60 and (f) 70 V.

Morphologies of the anodic coatings formed on aluminum at 70 V using 5g oxalic and 5g citric, 15g oxalic and 15g citric, and 25g oxalic and 25g citric acid solutions are shown in Fig. 8.2.2a, b and c, respectively. An analysis of these images revealed the formation of incomplete stripe type morphology in the case of coatings formed in 5g oxalic and 5g citric, 15g oxalic and 15g citric, and 25g oxalic and 25g citric acid solutions (Fig. 8.2.2a–c), but for 35g oxalic acid and 35g citric acid solution there could be seen complete absence of stripe morphology (Fig. 8.2.1f). This difference was attributed to the faster dissolution of the oxide layer in a stronger acid.

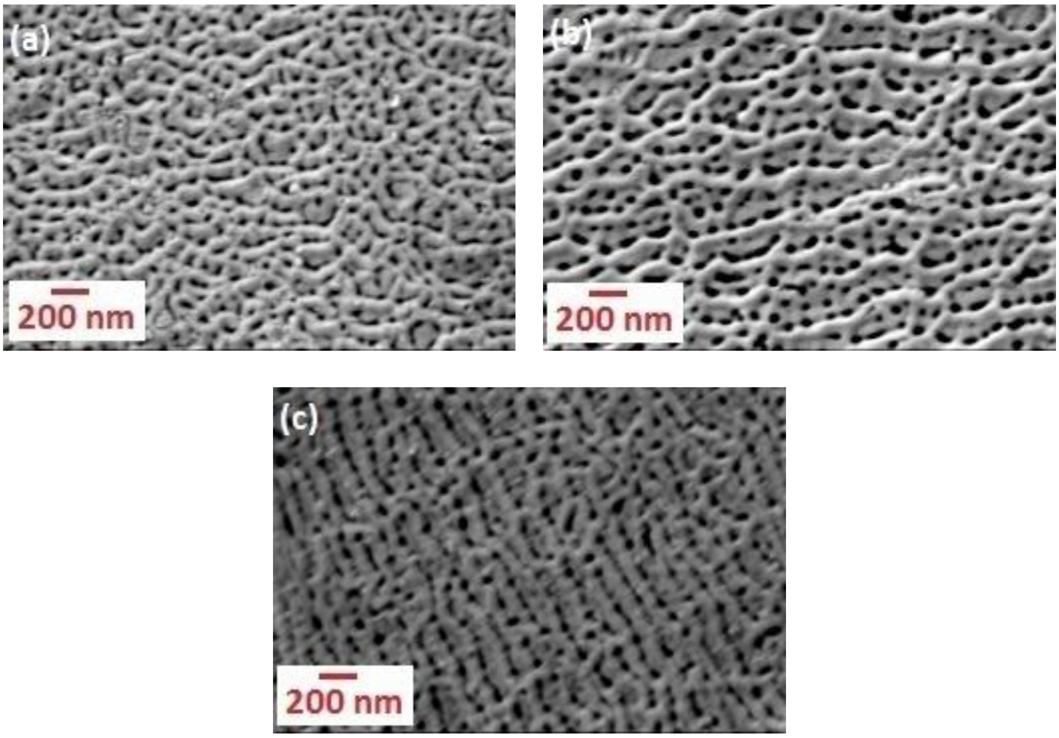

**Fig. 8.2.2** FE-SEM images of the anodic alumina coatings formed on aluminum at 70 V using a mixed solution consisting of (a) 5g oxalic acid and 5g citric acid, (b) 15g oxalic acid and 15g citric acid and (c) 25g oxalic acid and 25g citric acid.

A plot of porosity of anodic coatings on aluminum substrate versus potential applied during anodization is shown in Fig. 8.2.3a. The porosity calculation was done by analyzing the FE-SEM images using ImageJ software, as mentioned in section 3.5. The porosity can be found to increase in a linear fashion with increasing anodizing potential. The higher porosity at a higher potential was attributed to the faster field-assisted-dissolution of the oxide layer [206]. Porosity of the anodic coatings formed using baths of different strength is shown in Fig. 8.2.3b. The porosity of the coating formed in a stronger bath was found to be only marginally higher. A comparison of Fig. 8.2.3a and Fig. 8.2.3b easily revealed that the porosity depends much on anodizing potential than the strength of anodizing bath.

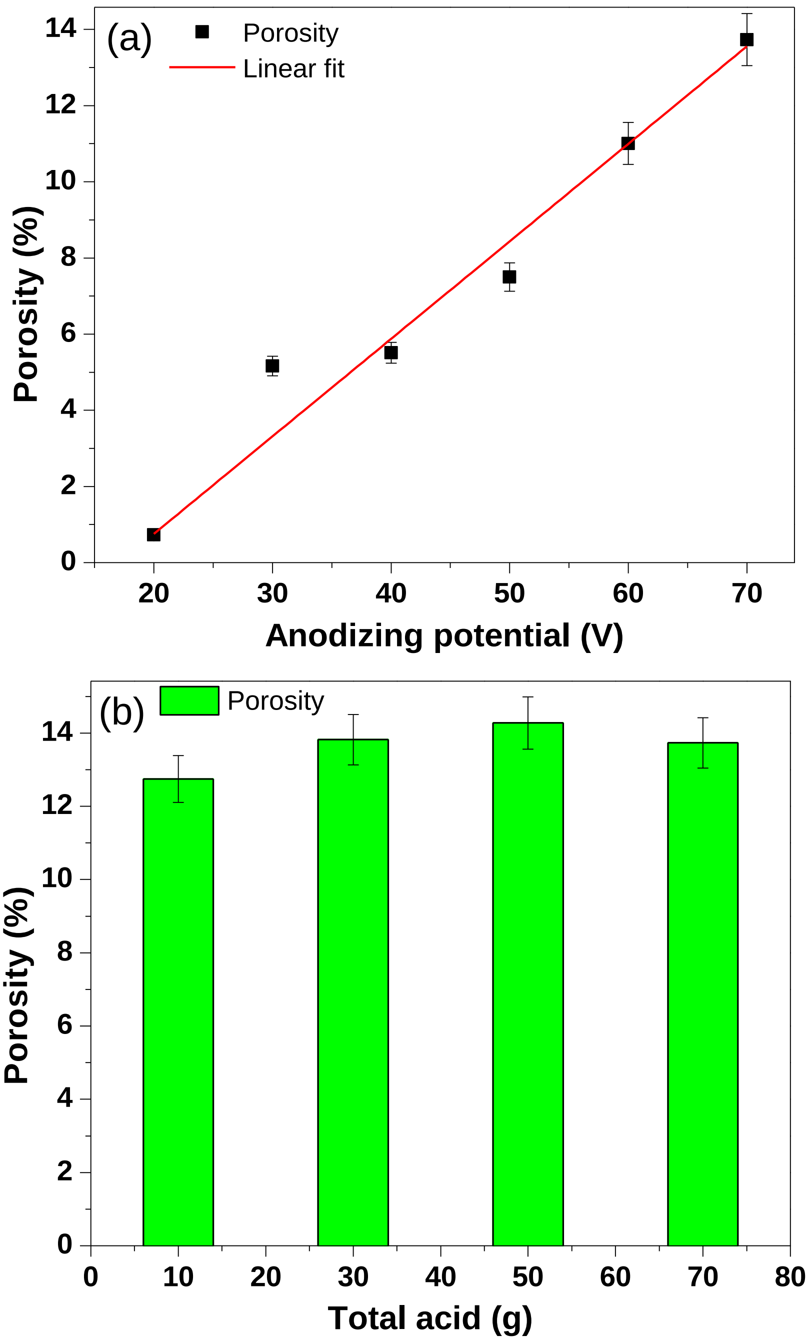

**Fig. 8.2.3** Calculated porosity (%) of the aluminum oxide coatings formed on aluminum as a function of (a) anodization potential and (b) bath composition.

## 8.3 Chemical composition and stoichiometry

XPS studies were carried out on the anodic alumina coatings formed on aluminum substrate at various anodizing potentials and bath concentrations to reveal their effect on the chemical composition of the coatings (for details of procedure see section 3.5). XPS general survey spectra for the anodic coatings formed at different potentials, in a mixed solution consisting of 35g oxalic acid and 35g citric acid are shown in Fig. 8.3.1. Corresponding to each coating there can be found peaks pertaining to Al-2p, Al-2s, C-1s, O-1s, O-Auger and C-Auger. The presence of carbon was attributed to both the specimen contamination during handling as well as the ingress of oxalate ions into the anodic layers during anodization [186].

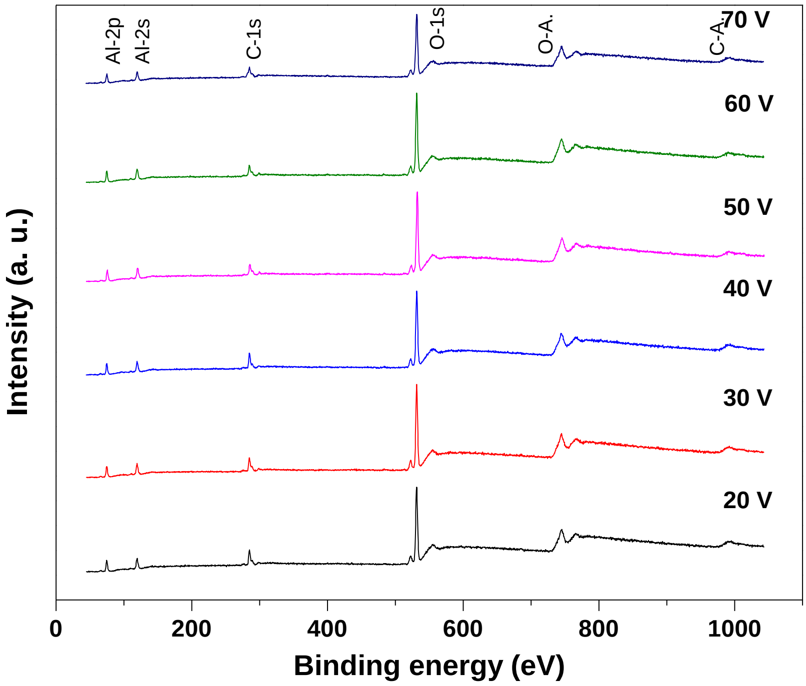

**Fig. 8.3.1** General survey XPS spectra of the anodic aluminum oxide coatings formed on aluminum, using a mixed solution consisting of 35g oxalic acid and 35g citric acid at 20-70V potentials.

The high resolution Al-2p spectra for all specimens and the resolved and fitted Al-2p spectrum for the coating formed at 20V are shown in Fig. 8.3.2a and b, respectively. The resolved Al-2p spectrum showed the presence of two peaks one at 74.5 eV and the other at 76 eV (Fig. 8.3.2b). The high intensity peak present at 74.5 eV was assigned to $Al_2O_3$ whereas the low intensity binding energy peak at 76 eV was found to be close to that of the aluminum hydroxide phase [207]. The formation of aluminum hydroxide related phase was believed to be due to atmospheric hydration of the anodized specimens. The existence of aluminum hydroxide was also detected during XRD measurements of the anodic alumina coatings formed in oxalic acid, as discussed in section 7.1. The high resolution O-1s spectra for all specimens and the resolved and fitted O-1s spectrum for the coating formed at 20 V are shown in Fig. 8.3.3a and b, respectively. There can be found only one resolved peak in the O-1s spectrum shown in Fig. 8.3.3b. This observation was in contrary to the two resolved peaks found for Al-2p spectra in Fig. 8.3.2b. This anomaly was attributed to the fact that the value of binding energy for O in $Al_2O_3$ and Al-OH phases are very close (for Al-OH the B.E. is marginally higher) therefore the O-1s spectra could not be resolved into two separate peaks. Further, for the anodic coating formed on aluminum at 70 V both the Al-2p and O-1s peaks are found to be marginally shifted towards the higher binding energy side (Figs. 8.3.2a and 8.3.3a). Also, the fitted Al-2p spectrum for this coating did not show the peak of aluminum hydroxide (Fig. 8.3.4). This could indicate that in this coating hydration did not occur. Because of this fact the Al-2p and O-1s spectra for the coating formed at 70 V were shifted towards the higher binding energy side.

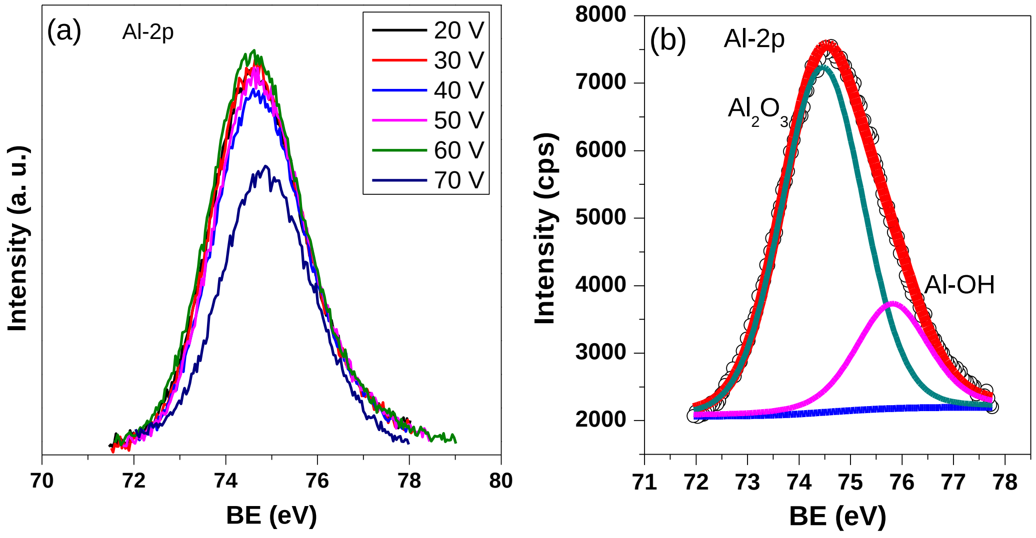

**Fig. 8.3.2** (a) High resolution Al-2p spectra for the anodic aluminum oxide coatings formed on aluminum at 20-70V, using a mixed solution consisting of 35g oxalic acid and 35g citric acid and (b) resolved Al-2p spectrum for the coating formed at 20 V.

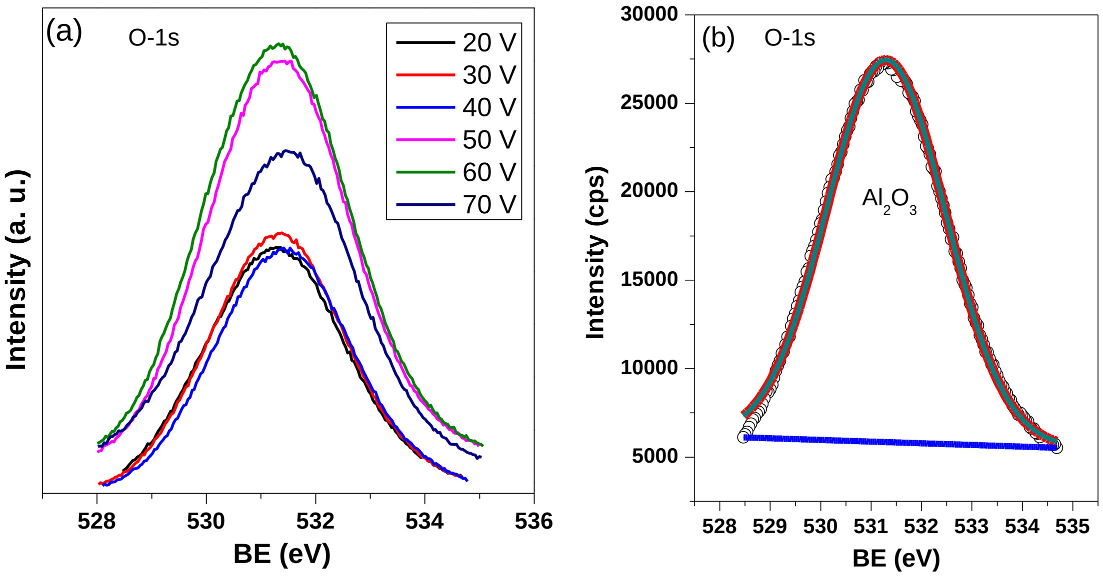

**Fig. 8.3.3** (a) High resolution O-1s spectra for the anodic aluminum oxide coatings formed on aluminum at 20-70V, using a mixed solution consisting of 35g oxalic acid and 35g citric acid and (b) resolved O-1s spectrum for the coating formed at 20 V.

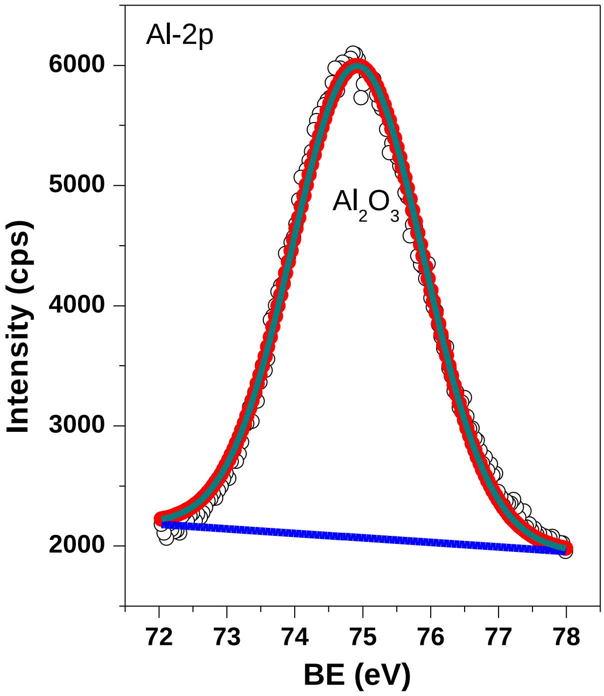

**Fig. 8.3.4** Resolved Al-2p spectrum for the anodic alumina coating formed on aluminum substrate at 70V, using a mixed solution consisting of 35g oxalic acid and 35g citric acid.

The oxygen concentration of the anodic coatings formed on aluminum, as determined by quantitative analysis of XPS results is plotted as a function of anodizing potential in Fig.

8.3.5. The oxygen concentration was found to increase linearly with anodizing potential. The minimum oxygen concentration was found to be 55.84 at.-% for the coating formed at 20 V whereas the maximum was 68.48 at.-% for the coating obtained at 70 V. The oxygen concentration of stoichiometric alumina is 60 at.-% therefore the anodic coatings formed at potentials lower than 40 V were hypo-stoichiometric whereas the coatings formed at potentials higher than 40 V were hyper-stoichiometric (Fig. 8.3.5). At 40V the oxygen concentration was 60.17 at.-% (Fig. 8.3.5) and this showed the formation of stoichiometric alumina on aluminum substrate at this potential. The increase in oxygen concentration with potential was attributed to the enhanced diffusion rate of oxalate ions from anodizing bath to the anodic layers during anodization. The migration of ionic species from anodizing bath to the anodic layers and their effect on the properties of the coatings is previously known up to some extent [186,187]. Lastly, XPS results of the aluminum oxide coatings formed on aluminum at 70 V using anodizing bath of different concentrations did not show any definite effect on chemical composition of the coatings.

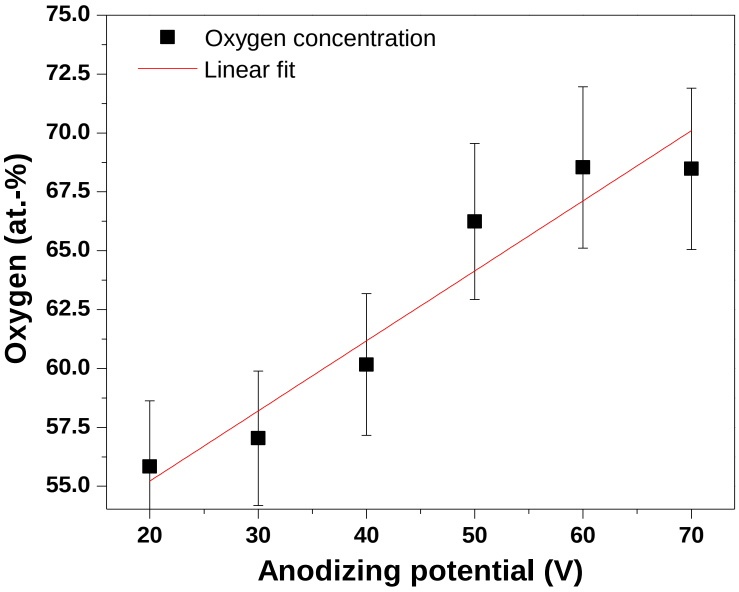

**Fig. 8.3.5** XPS derived oxygen concentration (at.-%) of the anodic alumina coatings formed on aluminum, using a mixed solution consisting of 35g oxalic acid and 35g citric acid, as a function of potential applied during anodization.

## 8.4 Conclusions

The following conclusions were drawn from the present study.

- Aluminum anodization experiments conducted in mixed solutions of oxalic acid and citric acid established that bath concentration had no relation with the formation of crystalline anodic aluminum oxide.
- The alumina coatings formed on aluminum substrate were found to be amorphous irrespective of the bath concentration used for anodization, for experiments conducted at 20–70V.
- The porosity of anodic aluminum oxide coatings on aluminum was found to increase linearly as the anodizing potential was increased.
- Bath concentration had no major influence on porosity of anodic coatings.
- The oxygen concentration of the anodic aluminum oxide coatings formed on aluminum substrate was found to increase linearly with anodizing potential. Stoichiometric alumina was obtained at 40V.

# Bibliography

1. R. Kumar, V. Prabhakar, and J. Saini, Alumina, *IJCET*, 2013, **3**, p 1679-1685

2. https://www.aluminum.org/industries/production/alumina-refining

3. https://todaysmachiningworld.com/magazine/how-it-works-coatings-for-cutting-tools/

4. G. Balakrishnan, R. Thirumurugesan, E. Mohandas, D. Sastikumar, P. Kuppusami, and J. I. Song, Phase Transition and Thermal Expansion Studies of Alumina Thin Films Prepared by Reactive Pulsed Laser Deposition, *J. Nanosci. Nanotechnol.*, 2014, **14**, p 7728–7733

5. G. Balakrishnan, P. Kuppusami, S. T. Sundari, R. Thirumurugesan, V. Ganesan, E. Mohandas, and D. Sastikumar, Structural and Optical Properties of γ-Alumina Thin Films Prepared by Pulsed Laser Deposition, *Thin Solid Films*, 2010, **518**, p 3898–3902

6. R. P. Singh, and S. Singhal, Investigation of Machining Characteristics in Rotary Ultrasonic Machining of Alumina Ceramic, *Mater. Manuf. Processes*, 2017, **32**, p 309–326

7. M. M. Hanon, E. Akman, B. G. Oztoprak, M. Gunes, Z. A. Taha, K. I. Hajim, E. Kacar, O. Gundogdu, and A. Demir, Experimental and Theoretical Investigation of the Drilling of Alumina Ceramic using Nd:YAG Pulsed Laser, *Opt. Laser Technol.*, 2012, **44**, p 913–922

8. R. Boidin, T. Halenkovič, V. Nazabal, L. Beneš, and P. Něme, Pulsed Laser Deposited Alumina Thin Films, *Ceram. Int.*, 2016, **42**, p 1177–1182

9. M. Touzin, D. Goeuriot, C. Guerret-Piécourt, D. Juvé, and H. -J. Fitting, Alumina based Ceramics for High-Voltage Insulation, *J. Eur. Ceram. Soc.*, 2010, **30**, p 805–817

10. B. H. Yan, F. Y. Huang, and H. M. Chow, Study on the Turning Characteristics of Alumina-based Ceramics, *J. Mater. Process. Technol.*, 1995, **54**, p 341-347

11. J. Muller, and D. Neuschutz, Efficiency of α-Alumina as Diffusion Barrier between Bond Coat and Bulk Material of Gas Turbine Blades, *Vacuum*, 2003, **71**, p 247–251

12. Tun-Ping Teng, Yi-Hsuan Hung, Tun-Chien Teng, and Jyun-Hong Chen, Performance Evaluation on an Air-cooled Heat Exchanger for Alumina Nanofluid under Laminar Flow, *Nanoscale Res. Lett.*, 2011, **6**, p 488

13. Chang-Woo Kwon, Ji-Won Son, Jong-Ho Lee, Hyun-Mi Kim, Hae-Weon Lee, and Ki-Bum Kim, High-Performance Micro-Solid Oxide Fuel Cells Fabricated on Nanoporous Anodic Aluminum Oxide Templates, *Adv. Funct. Mater.*, 2011, **21**, p 1154–1159

14. A. S. Kumar, A. R. Durai, and T. Sornakumar, Machinability of Hardened Steel using Alumina based Ceramic Cutting Tools, *Int. J. Refract. Metals Hard Mater.*, 2003, **21**, p 109–117

15. Youn-Soo Park, Sung-Kwan Hwang, Won-Sik Choy, Yong-Sik Kim, Young-Wan Moon, and Seung-Jae Lim, Ceramic Failure After Total Hip Arthroplasty with an Alumina-on-Alumina Bearing, *J. Bone Joint Surg.*, 2006, **88**, p 780–787

16. J. Tinschert, G. Natt, N. Mohrbotter, H. Spiekermann, and K. A. Schulze, Lifetime of Alumina- and Zirconia Ceramics Used for Crown and Bridge Restorations, *J. Biomed. Mater. Res. Part B*, 2007, **80**, p 317-321

17. S. Stojadinovic, R. Vasilic, I. Belca, M. Tadic, B. Kasalica, and L. Zekovic, Structural and Luminescence Characterization of Porous Anodic Oxide Films on Aluminum Formed in Sulfamic Acid Solution, *Appl. Surf. Sci.*, 2008, **255**, p 2845–2850

18. S. Stojadinovic, R. Vasilic, Z. Nedic, B. Kasalica, I. Belca, and L. Zekovic, Photoluminescent Properties of Barrier Anodic Oxide Films on Aluminum, *Thin Solid Films*, 2011, **519**, p 3516–3521

19. I. A. Vrublevsky, K. V. Chernyakova, A. Ispas, A. Bund, and S. Zavadski, Optical Properties of Thin Anodic Alumina Membranes Formed in a Solution of Tartaric Acid, *Thin Solid Films*, 2014, **556**, p 230–235

20. V. Branzoi, F. Golgovici, and F. Branzoi, Aluminum Corrosion in Hydrochloric Acid Solutions and the Effect of some Organic Inhibitors, *Mater. Chem. Phys.*, 2002, **78**, p 122–131

21. V. Lopez, J. A. Gonzalez, E. Otero, E. Escudero, and M. Morcillo, Atmospheric Corrosion of Bare and Anodised Aluminium in a Wide Range of Environmental Conditions. Part II: Electrochemical Responses, *Surf. Coat. Technol.*, 2002, **153**, p 235–244

22. N. Tsyntsaru, B. Kavas, J. Sort, M. Urgen, and J. P. Celis, Mechanical and Frictional Behaviour of Nano-porous Anodised Aluminium, *Mater. Chem. Phys.*, 2014, **148**, p 887–895

23. H. S. Kim, D. H. Kim, W. Lee, S. J. Cho, J. H. Hahn, and H. S. Ahn, Tribological Properties of Nanoporous Anodic Aluminum Oxide Film, *Surf. Coat. Technol.*, 2010, **205**, p 1431–1437

24. S. T. Aruna, N. Balaji, J. Shedthi, V. K. William Grips, Effect of Critical Plasma Spray Parameters on the Microstructure, Microhardness and Wear and Corrosion Resistance of Plasma Sprayed Alumina Coatings, *Surf. Coat. Technol.*, 2012, **208**, p 92–100

25. X. Nie, E. I. Meletis, J. C. Jiang, A. Leyland, A. L. Yerokhin, and A. Matthews, Abrasive Weary Corrosion Properties and TEM Analysis of $Al_2O_3$ Coatings Fabricated using Plasma Electrolysis, *Surf. Coat. Technol.*, 2002, **149**, p 245–251

26. T. Islam, L. Kumar, and S. A. Khan, A Novel Sol–gel Thin Film Porous Alumina Based Capacitive Sensor for Measuring Trace Moisture in the Range of 2.5–25 ppm, *Sens. Actuators, B*, 2012, **173**, p 377–384

27. L. F. Marsal, L. Vojkuvka, P. Formentin, J. Pallarés, and J. Ferré-Borrull, Fabrication and Optical Characterization of Nanoporous Alumina Films Annealed at different Temperatures, *Opt. Mater.*, 2009, **31**, p 860–864

28. J. Muller, M. Schierling, E. Zimmermann, and D. Neuschutz, Chemical Vapor Deposition of Smooth a-$Al_2O_3$ Films on Nickel Base Superalloys as Diffusion Barriers, *Surf. Coat. Technol.*, 1999, **120–121**, p 16–21

29. S. Li, D. He, X. Liu, S. Wang, and L. Jiang, Deuterium Permeation of Amorphous Alumina Coating on 316L Prepared by MOCVD, *J. Nucl. Mater.*, 2012, **420**, p 405–408

30. R. Snyders, K. Jiang, D. Music, S. Konstantinidis, T. Markus, A. Reinholdt, J. Mayer, and J. M. Schneider, Composition–constitution–morphology Relationship of $Al_2O_3$ Thin Films Deposited by Plasma Assisted Chemical Vapor Deposition, *Surf. Coat. Technol.*, 2009, **204**, p 215–221

31. Y. You, A. Ito, R. Tu, and T. Goto, Low-temperature Deposition of $\alpha$-$Al_2O_3$ Films by Laser Chemical Vapour Deposition using a Diode Laser, *Appl. Surf. Sci.*, 2010, **256**, p 3906–3911

32. M. D. Groner, F. H. Fabreguette, J. W. Elam, and S. M. George, Low-Temperature $Al_2O_3$ Atomic Layer Deposition, *Chem. Mater.*, 2004, **16**, p 639–645

33. T. Kohara, H. Tamagaki, Y. Ikari, and H. Fujii, Deposition of $\alpha$-$Al_2O_3$ Hard Coatings by Reactive Magnetron Sputtering, *Surf. Coat. Technol.*, 2004, **185**, p 166–171

34. P. Nayar, A. Khanna, D. Kabiraj, S. R. Abhilash, B. D. Beake, Y. Losset, and B. Chen, Structural, Optical and Mechanical Properties of Amorphous and Crystalline Alumina Thin Films, *Thin Solid Films*, 2014, **568**, p 19–24

35. R. Brill, F. Koch, J. Mazurelle, D. Levchuk, M. Balden, Y. Yamada-Takamura, H. Maier, and H. Bolt, Crystal Structure Characterisation of Filtered Arc Deposited Alumina Coatings: Temperature and Bias Voltage, *Surf. Coat. Technol.*, 2003, **174–175**, p 606–610

36. O. Sarikaya, Effect of Some Parameters on Microstructure and Hardness of Alumina Coatings Prepared by the Air Plasma Spraying Process, *Surf. Coat. Technol.*, 2005, **190**, p 388–393

37. M. Ghrib, R. Ouertani, M. Gaidi, N. Khedher, M. B. Salem, and H. Ezzaouia, Effect of Annealing on Photoluminescence and Optical Properties of Porous Anodic Alumina Films Formed in Sulfuric Acid for Solar Energy Applications, *Appl. Surf. Sci.*, 2012, **258**, p 4995–5000

38. T. Wang, J. Pu, C. Bo, and L. Jian, Sol–gel Prepared $Al_2O_3$ Coatings for the Application as Tritium Permeation Barrier, *Fusion Eng. Des.*, 2010, **85**, p 1068–1072

39. G. K. Zhang, C. A. Chen, D. L. Luo, and X. L. Wang, An Advance Process of Aluminum Rich Coating as Tritium Permeation Barrier on 321 Steel Workpiece, *Fusion Eng. Des.*, 2012, **87**, p 1370–1375

40. H. G. Yang, Q. Zhan, W. W. Zhao, X. M. Yuan, Y. Hu, and Z. B. Han, Study of an Iron-Aluminide and Alumina Tritium Barrier Coating, *J. Nucl. Mater.*, 2011, **417**, p 1237–1240

41. Z. Guikai, L. Ju, C. Chang'an, D. Sanping, and Ling Guoping, Tritium Permeation Barrier-Aluminized Coating Prepared by Al-plating and Subsequent Oxidation Process, *J. Nucl. Mater.*, 2011, **417**, p 1245–1248

42. F. Yang, X. Xiang, G. Lu, G. Zhang, T. Tang, Y. Shi, and X. Wang, Tritium Permeation Characterization of $Al_2O_3$/FeAl Coatings as Tritium Permeation Barriers on 321 Type Stainless Steel Containers, *J. Nucl. Mater.*, 2016, **478**, p 144–148

43. J. Tang, and K. Azumi, Optimization of Pulsed Electrodeposition of Aluminum from $AlCl_3$-1-Ethyl-3-Methylimidazolium Chloride Ionic Liquid, *Electrochim. Acta*, 2011, **56**, p 1130–1137

44. T. Jiang, M. J. Chollier Brym, G. Dubé, A. Lasia, and G. M. Brisard, Electrodeposition of Aluminium from Ionic Liquids: Part II - Studies on the Electrodeposition of Aluminum from Aluminum Chloride ($AICl_3$)-Trimethylphenylammonium Chloride (TMPAC) Ionic Liquids, *Surf. Coat. Technol.*, 2006, **201**, p 10–18

45. A. M. Rashidi, and A. Amadeh, The Effect of Current Density on the Grain Size of Electrodeposited Nanocrystalline Nickel Coatings, *Surf. Coat. Technol.*, 2008, **202**, p 3772–3776

46. S. Stojadinovic, Lj. Zekovic, I. Belca, and B. Kasalica, Galvanoluminescence of Oxide Films Formed by Anodization of Aluminum in Phosphoric Acid, *Electrochem. Commun.*, 2004, **6**, p 427–431

47. G. D. Sulka, and W. J. Stepniowski, Structural Features of Self-organized Nanopore Arrays Formed by Anodization of Aluminum in Oxalic Acid at Relatively High Temperatures, *Electrochim. Acta*, 2009, **54**, p 3683–3691

48. S. Stojadinovic, I. Belca, Lj. Zekovic, B. Kasalica, and D. Nikolic, Galvanoluminescence of Porous Oxide Films Formed by Anodization of Aluminum in Chromic Acid Solution, *Electrochem. Commun.*, 2004, **6**, p 1016–1020

49. N. Hu, X. Dong, X. He, J. F. Browning, and D. W. Schaefer, Effect of Sealing on the Morphology of Anodized Aluminum Oxide, *Corros. Sci.*, 2015, **97**, p 17–24

50. G. E. J. Poinern, N. Ali, and D. Fawcett, Progress in Nano-Engineered Anodic Aluminum Oxide Membrane Development, *Materials*, 2011, **4**, p 487–526

51. R. K. Choudhary, K. P. Sreeshma, and P. Mishra, Effect of Surface Roughness of an Electropolished Aluminum Substrate on the Thickness, Morphology, and Hardness of Aluminum Oxide Coatings Formed During Anodization in Oxalic Acid, *J. Mater. Eng. Perform.*, 2017, **26**, p 3614–3620

52. L. Vojkuvka, A. Santos, J. Pallares, J. Ferre-Borrull, L. F. Marsal, and J. P. Celis, On the Mechanical Properties of Nanoporous Anodized Alumina by Nanoindentation and Sliding Tests, *Surf. Coat. Technol.*, 2012, **206**, p 2115–2124

53. F. Riddar, S. Hogmark, and A. K. Rudolphi, Comparison of Anodised Aluminium Surfaces from Four Fabrication Methods, *J. Mater. Process. Technol.*, 2012, **212**, p 2272–2281

54. U. Malayoglu, K. C. Tekin, U. Malayoglu, and S. Shrestha, An Investigation into the Mechanical and Tribological Properties of Plasma Electrolytic Oxidation and Hard-Anodized Coatings on 6082 Aluminum Alloy, *Mater. Sci. Eng., A*, 2011, **528**, p 7451–7460

55. Y. C. Choi, J. Y. Hyeon, S. D. Bu, and T. S. Bae, Effects of Anodizing Voltages and Corresponding Current Densities on Self-ordering Process of Nanopores in Porous Anodic Aluminas Anodized in Oxalic and Sulfuric Acids, *J. Korean Phys. Soc.*, 2009, **55**, p 835–840

56. S. Ono, and N. Masuko, Evaluation of Pore Diameter of Anodic Porous Films Formed on Aluminum, *Surf. Coat. Technol.*, 2003, **169-170**, p 139–142

57. E. Berretti, A. Giaccherini, S. M. Martinuzzi, M. Innocenti, T. J. S. Schubert, F. M. Stiemke, and S. Caporali, Aluminium Electrodeposition from Ionic Liquid: Effect of Deposition Temperature and Sonication, *Materials*, 2016, 9, p 719

58. H. O. Pierson, Chemical Vapour Deposition of Nonsemiconductor Materials, *ASM Metals HandBook Vol. 5 - Surface Engineering, 2002*

59. A. Larsson, and S. Ruppi, Microstructure and Properties of CVD $\gamma$-$Al_2O_3$ Coatings, *Int. J. Refract. Met. Hard Mater,* 2001, **19**, p 515–522

60. M. Halvarsson, and S. Vuorinen, The Influence of the Nucleation Surface on the Growth of CVD $\alpha$-$A1_2O_3$ and $\kappa$-$A1_2O_3$, *Surf. Coat. Technol.*, 1995, **76-77**, p 287-296

61. P. K. Tedrow, and R. Reif, Plasma-Enhanced Chemical Vapor Deposition, *ASM Metals HandBook Vol. 5 - Surface Engineering, 2002*

62. S. Konstantinidis, K. Jiang, A. Roobroek, F. Renaux, and J. M. Schneider, Pulsed Plasma Enhanced Chemical Vapor Deposition of Alumina Thin Films: Influence of the Duty Cycle on Structure and Elastic Properties, *Plasma Processes Polym.*, 2011, **8**, p 651–657

63. K. Jiang, K. Sarakinos, S. Konstantinidis, and J. M. Schneider, Low Temperature Synthesis of $\alpha$-$Al_2O_3$ Films by High Power Plasma Assisted Chemical Vapor Deposition, *J. Phys. D: Appl. Phys.*, 2010, **43**, p 325202

64. O. Kyrylov, R. Cremer, and D. Neuschutz, Deposition of Alumina Hard Coatings by Bipolar Pulsed PECVD, *Surf. Coat. Technol.*, 2003, **163–164**, p 203–207

65. M. C. Ntsama-Etoundi, J. Desmaison, P. Tristant, and C. Tixier, Remote Microwave Plasma Enhanced Chemical Vapour Deposition of Alumina on Metallic Substrates, *Surf. Coat. Technol.*, 1999, **120–121**, p 233–237

66. H. Kadokura, A. Ito, T. Kimura, and T. Goto, Moderate Temperature and High-speed Synthesis of $\alpha$-$Al_2O_3$ Films by Laser Chemical Vapor Deposition using Nd:YAG Laser, *Surf. Coat. Technol.*, 2010, **204**, p 2302–2306

67. R. W. Johnson, A. Hultqvist, and S. F. Bent, A Brief Review of Atomic Layer Deposition: From Fundamentals to Applications, *Mater. Today*, 2014, **17**, p 236–246

68. D. S. Finch, T. Oreskovic, K. Ramadurai, C. F. Herrmann, S. M. George, and R. L. Mahajan, Biocompatibility of Atomic Layer-deposited Alumina Thin Films, *J. Biomed. Mater. Res. Part A*, 2008, **87**, p 100–106

69. J. Kim, K. Chakrabarti, J. Lee, Ki-Young Oh, and C. Lee, Effects of Ozone as an Oxygen Source on the Properties of the $Al_2O_3$ Thin Films Prepared by Atomic Layer Deposition, *Mater. Chem. Phys.*, 2003,**78**, p 733–738

70. S. L. Rohde, Sputter Deposition, *ASM Metals HandBook Vol. 5 - Surface Engineering, 2002*

71. H. Kakati, A. R. Pal, H. Bailung, and J. Chutia, Deposition of Nanostructured Crystalline and Corrosion Resistant Alumina Film on Bell Metal at Low Temperature by rf Magnetron Sputtering, *Appl. Surf. Sci.*, 2009, **255**, p 7403–7407

72. E. Wallin, T. I. Selinder, M. Elfwing, and U. Helmersson, Synthesis of $\alpha$-$Al_2O_3$ Thin Films using Reactive High-power Impulse Magnetron Sputtering, *EPL*, 2008, **82**, 36002P1–36002P5

73. J. M. Schneider, W. D. Sproul, A. A. Voevodin, and A. Matthews, Crystalline Alumina Deposited at Low Temperatures by Ionized Magnetron Sputtering, *J. Vac. Sci. Technol., A*, 1997, **15**, p 1084–1088

74. J. S. Horwitz, Pulsed-Laser Deposition, *ASM Metals HandBook Vol. 5 - Surface Engineering, 2002*

75. G. Balakrishnanan, S. T. Sundari, R. Ramaseshan, R. Thirumurugesan, E. Mohandas, D. Sastikumar, P. Kuppusami, T. G. Kim, and J. I. Song, Effect of Substrate Temperature on Microstructure and Optical Properties of Nanocrystalline Alumina Thin Films, *Ceram. Int.*, 2013, **39**, p 9017–9023

76. G. Balakrishnan, R. V. Babu, K. S. Shin, J. I. Song, Growth of Highly Oriented γ- and α-$Al_2O_3$ Thin Films by Pulsed Laser Deposition, *Opt. Laser Technol.*, 2014, **56**, p 317–321

77. http://www.semicore.com/news/89-what-is-e-beam-evaporation

78. Li-jun He, C. Li, and Xing-zhao Liu, The Optical Properties of Alumina Films Prepared by Electron Beam Evaporation at Oblique Incidence, *Mater. Lett.*, 2013, **101**, p 1–4

79. I. N. Reddy, N. Sridhara, P. Bera, C. Anandan, A. K. Sharma, and A. Dey, Nanostructured Alumina Films by E-beam Evaporation, *Ceram. Int.*, 2015, **41**, p 10537–10546

80. D. M. Sanders, J. W. Glaser, and S. Falabella, Arc Deposition, *ASM Metals HandBook Vol. 5 - Surface Engineering, 2002*

81. B. K. Tay, Z. W. Zhao, and C. Q. Sun, Effects of Substrate Bias and Growth Temperature on Properties of Aluminium Oxide Thin Films by using Filtered Cathodic Vacuum Arc, *Surf. Coat. Technol.*, 2005, **198**, p 94–97

82. Y. S. Choong, B. K. Tay, S. P. Lau, X. Shi, and Y. H. Cheng, High Deposition Rate of Aluminum Oxide Film by Off-plane Double Bend Filtered Cathodic Vacuum Arc Technique, *Thin Solid Films*, 2001, **386**, p 1–5

83. Z. W. Zhao, B. K. Tay, G. Q. Yu, D. H. C. Chua, S. P. Lau, and L. K. Cheah, Optical Properties of Aluminium Oxide Thin Films Prepared at Room Temperature by Off-plane Filtered Cathodic Vacuum Arc System, *Thin Solid Films*, 2004, **447–448**, p 14–19

84. R. C. Tucker, Thermal Spray Coatings, *ASM Metals HandBook Vol. 5 - Surface Engineering, 2002*

85. V. P. Singh, A. Sil, and R. Jayaganthan, A Study on Sliding and Erosive Wear Behaviour of Atmospheric Plasma Sprayed Conventional and Nanostructured Alumina Coatings, *Mater. Design*, 2011, **32**, p 584–591

86. Y. Gao, X. Xu, Z. Yan, and G. Xin, High Hardness Alumina Coatings Prepared by Low Power Plasma Spraying, *Surf. Coat. Technol.*, 2002, **154**, p 189–193

87. E. Turunen, T. Varis, S. -P. Hannula, A. Vaidya, A. Kulkarni, J. Gutleber, S. Sampath, and H. Herman, On the Role of Particle State and Deposition Procedure on Mechanical, Tribological and Dielectric Response of High Velocity Oxy-fuel Sprayed Alumina Coatings, *Mater. Sci. Eng., A*, 2006, **415**, p 1–11

88. P. Saravanan, V. Selvarajan, D. S. Rao, S. V. Joshi, and G. Sundarajan, Influence of Process Variables on Quality of Detonation Gun Sprayed Alumina Coatings, *Surf. Coat. Technol.*, 2000, **123**, p 44–54

89. H. Habazaki, M. Uozumi, H. Konno, K. Shimizu, P. Skeldon, and G. E. Thompson, Crystallization of Anodic Titania on Titanium and its Alloys, *Corros. Sci.*, 2003, **45**, p 2063–2073

90. I. Sieber, H. Hildebrand, A. Friedrich, and P. Schmuki, Formation of Self-organized Niobium Porous Oxide on Niobium, *Electrochem. Commun.*, 2005, **7**, p 97–100

91. I. Sieber, B. Kannan, and P. Schmuki, Self-Assembled Porous Tantalum Oxide Prepared in $H_2SO_4$/HF Electrolytes, *Electrochem. Solid-State Lett.*, 2005, **8**, p J10–J12

92. S. Ono, K. Asami, T. Osaka, and N. Masuko, Structure of Anodic Films Formed on Magnesium, *J. Electrochem. Soc.*, 1996, **143**, p L62–L63

93. S. Ismail, Z. A. Ahmad, A. Berenov, and Zainovia Lockman, Effect of Applied Voltage and Fluoride Ion Content on the Formation of Zirconia Nanotube Arrays by Anodic Oxidation of Zirconium, *Corros. Sci.*, 2011, **53**, p 1156–1164

94. Y. Zuo, Peng-Hui Zhao, and Jing-Mao Zhao, The Influences of Sealing Methods on Corrosion Behavior of Anodized Aluminum Alloys in NaCl Solutions, *Surf. Coat. Technol.*, 2003, **166**, p 237–242

95. F. A. Bonilla, A. Berkani, Y. Liu, P. Skeldon, G. E. Thompson, H. Habazaki, K. Shimizu, C. John, and K. Stevens, Formation of Anodic Films on Magnesium Alloys in an Alkaline Phosphate Electrolyte, *J. Electrochem. Soc.*, 2002, **149**, p B4–B13

96. C. S. Kumar, S. M. Mayanna, K. N. Mahendra, A. K. Sharma, and R. U. Rani, Studies on White Anodizing on Aluminum Alloy for Space Applications, *Appl. Surf. Sci.*, 1999, **151**, p 280–286

97. F. Hekmat, B. Sohrabi, and M. S. Rahmanifar, Growth of the Cobalt Nanowires using AC Electrochemical Deposition on Anodized Aluminum Oxide Templates, *J. Nanostructure Chem.*, 2014, **4**, p 105

98. K. Abushgair, and O. Al-Araidah, Anodizing of Aluminum for Solar Cell Application, *NanoWorld J.*, 2016, **2**, p 15–19

99. F. Rumiche, H. H. Wang, W. S. Hu, J. E. Indacochea, and M. L. Wang, Anodized Aluminum Oxide (AAO) Nanowell Sensors for Hydrogen Detection, *Sens. Actuators, B*, 2008, **134**, p 869–877

100. J. Chen, S. Wang, L. Ding, Y. Jiang, and Haihui Wang, Performance of Through-hole Anodic Aluminum Oxide Membrane as a Separator for Lithium-ion Battery, *J. Membr. Sci.*, 2014, **461**, p 22–27

101. D. Brüggemann, Nanoporous Aluminium Oxide Membranes as Cell Interfaces, *J. Nanomater.*, 2013, **2013**

102. K. Schwirn, W. Lee, R. Hillebrand, M. Steinhart, K. Nielsch, and U. Gösele, Self-Ordered Anodic Aluminum Oxide Formed by $H_2SO_4$ Hard Anodization, *ACS Nano*, 2008, **2**, p 302–310

103. I. Mínguez-Bacho, S. Rodríguez-Lopez, A. Climent-Font, D. Fichou, M. Vazquez, and M. Hernandez-Velez, Variation of the Refractive Index by means of Sulfate Anion Incorporation into Nanoporous Anodic Aluminum Oxide Films, *Microporous Mesoporous Mater.*, 2016, **225**, p 192–197

104. H. Zhuo, F. Peng, L. Lin, Y. Qu, and F. Lai, Optical Properties of Porous Anodic Aluminum Oxide Thin Films on Quartz Substrates, *Thin Solid Films*, 2011, **519**, p 2308–2312

105. N. M. Yakovleva, L. Anicai, A. N. Yakovlev, L. Dima, E. Y. Khanina, M. Buda, and E. A. Chupakhina, Structural Study of Anodic Films Formed on Aluminum in Nitric Acid Electrolyte, *Thin Solid Films*, 2002, **416**, p 16–23

106. S. Shingubara, K. Morimoto, H. Sakaue, and T. Takahagi, Self-Organization of a Porous Alumina Nanohole Array Using a Sulfuric/Oxalic Acid Mixture as Electrolyte, *Electrochem. Solid-State Lett.*, 2004, **7**, p E15–E17

107. Tzung-Ta Kao, and Yao-Chung Chang, Influence of Anodization Parameters on the Volume Expansion of Anodic Aluminum Oxide Formed in Mixed Solution of Phosphoric and Oxalic Acids, *Appl. Surf. Sci.*, 2014, **288**, p 654–659

108. T. Kikuchi, T. Yamamoto, S. Natsui, and R. O. Suzuki, Fabrication of Anodic Porous Alumina by Squaric Acid Anodizing, *Electrochim. Acta*, 2014, **123**, p 14–22

109. J. Ren, and Y. Zuo, The Anodizing Behavior of Aluminum in Malonic Acid Solution and Morphology of the Anodic Films, *Appl. Surf. Sci.*, 2012, **261**, p 193–200

110. T. Kikuchi, T. Yamamoto, and R. O. Suzuki, Growth Behavior of Anodic Porous Alumina Formed in Malic Acid Solution, *Appl. Surf. Sci.*, 2013, **284**, p 907–913

111. T. Kikuchi, O. Nishinaga, S. Natsui, and R. O. Suzuki, Self-ordering Behavior of Anodic Porous Alumina via Selenic Acid Anodizing, *Electrochim. Acta*, 2014, **137**, p 728–735

112. T. Kikuchi, D. Nakajima, J. Kawashima, S. Natsui, and R. O. Suzuki, Fabrication of Anodic Porous Alumina via Anodizing in Cyclic Oxocarbon Acids, *Appl. Surf. Sci.*, 2014, **313**, p 276–285

113. S. Akiya, T. Kikuchi1, S. Natsui, N. Sakaguchi, and R. O. Suzuki, Self-ordered Porous Alumina Fabricated via Phosphonic Acid Anodizing, *Electrochim. Acta*, 2016, **190**, p 471–479

114. T. Kikuchi, O. Nishinaga, S. Natsui, and R. O. Suzuki, Fabrication of Self-ordered Porous Alumina via Etidronic Acid Anodizing and Structural Color Generation from Submicrometer-scale Dimple array, *Electrochim. Acta*, 2015, **156**, p 235–243

115. D. Nakajima, T. Kikuchi, S. Natsui, R. O. Suzuk, Superhydrophilicity of a Nanofiber-Covered Aluminum Surface Fabricated via Pyrophosphoric Acid Anodizing, *Appl. Surf. Sci.*, 2016, **389**, p 173–180

116. A. Santos, G. Macías, J. Ferré-Borrull, J. Pallarès, and L. F. Marsal, Photoluminescent Enzymatic Sensor Based on Nanoporous Anodic Alumina, *ACS Appl. Mater. Interfaces*, 2012, **4**, p 3584–3588

117. Wei-Chih Tsai, Shui-Jinn Wang, Jun-Ku Lin, Chia-Lung Chang, and Rong-Ming Ko, Preparation of Vertically-aligned Nickel Nanowires with Anodic Aluminum Oxide Templates and their Application as Field Emitters, *Electrochem. Commun.*, 2009, **11**, p 660–663

118. N. Hu, X. Dong, X. He, J. F. Browning, and D. W. Schaefer, Effect of Sealing on the Morphology of Anodized Aluminum Oxide, *Corros. Sci.*, 2015, **97**, p 17–24

119. https://en.wikipedia.org/wiki/Plasma_electrolytic_oxidation

120. De-Jiu Shen, Yu-Lin Wang, P. Nash, and Guang-Zhong Xing, Microstructure, Temperature Estimation and Thermal Shock Resistance of PEO Ceramic Coatings on Aluminum, *J. Mater. Process. Technol.*, 2008, **205**, p 477–481

121. S. Stojadinovic, R. Vasilic, I. Belca, M. Petkovic, B. Kasalica, Z. Nedic, and Lj. Zekovic, Characterization of the Plasma Electrolytic Oxidation of Aluminium in Sodium Tungstate, *Corros. Sci.*, 2010, **52**, p 3258–3265

122. G. Lv, W. Gu, H. Chen, W. Feng, M. L. Khosa, L. Li, E. Niu, G. Zhang, and Si-Ze Yang, Characteristic of Ceramic Coatings on Aluminum by Plasma Electrolytic Oxidation in Silicate and Phosphate Electrolyte, *Appl. Surf. Sci.*, 2006, **253**, p 2947–2952

123. Z. Wu, Y. Xia, G. Li, and F. Xu, Structure and Mechanical Properties of Ceramic Coatings Fabricated by Plasma Electrolytic Oxidation on Aluminized Steel, *Appl. Surf. Sci.*, 2007, **253**, p 8398–8403

124. D. Wang, and G. P. Bierwagen, Sol–gel Coatings on Metals for Corrosion Protection, *Prog. Org. Coat.*, 2009, **64**, p 327–338

125. C. J. Brinker, A. J. Hurd, P. R. Schunk, G. C. Frye, and C. S. Ashley, Review of Sol-gel Thin Film Formation, *J. Non-Cryst. Solids*, 1992, **147&148**, p 424–436

126. Y. Ueki, T. Kunugi, N. B. Morley, M. A. Abdou, Electrical Insulation Test of Alumina Coating Fabricated by Sol–gel Method in Molten PbLi Pool, *Fusion Eng. Des.*, 2010, **85**, p 1824–1828

127. B. Hua, M. Yao, R. Xiao, J. Chen, and X. Yao, Optical Properties of Amorphous $Al_2O_3$ Thin Films Prepared by a Sol–gel Process, *Ceram. Int.*, 2014, **40**, p 14133–14139

128. G. Ruhi, O. P. Modi, and I. B. Singh, Corrosion Behaviour of Nano Structured Sol-gel Alumina Coated 9Cr–1Mo Ferritic Steel in Chloride Bearing Environments, *Surf. Coat. Technol.*, 2009, **204**, p 359–365

129. A. Mitra, D. Jana, and G. De, Facile Synthesis of Hexagonally Ordered Mesoporous Aluminum Oxide Thin Films with High Catalytic Activity, *Microporous Mesoporous Mater.*, 2012, **158**, p 187–194

130. Yo-Yu Chang, Charng-Cheng Tsaur, and J. C. Rock, Microstructure Studies of an Aluminide Coating on 9Cr-1Mo Steel during High Temperature Oxidation, *Surf. Coat. Technol.*, 2006, **200**, p 6588–6593

131. Sven-Erik Wulf, W. Krauss, and Jürgen Konys, Comparison of Coating Processes in the Development of Aluminum-based Barriers for Blanket Applications, *Fusion Eng. Des.*, 2014, **89**, p 2368–2372

132. X. Xiang, X. Wang, G. Zhang, T. Tang, and X. Lai, Preparation Technique and Alloying Effect of Aluminide Coatings as Tritium Permeation Barriers: A Review, *Int. J. Hydrogen Energy*, 2015, **40**, p 3697–3707

133. H. Glasbrenner, and O. Wedemeyer, Comparison of Hot Dip Aluminised F82H-mod. Steel After Different Subsequent Heat Treatments, *J. Nucl. Mater.*, 1998, **257**, p 274–281

134. J. Purushothaman, R. Ramaseshan, S. K. Albert, R. Rajendran, N. Murugesan, C. Ramesh, and N. Gowrishankar, Preparation and Characterization of T-permeation Barrier on RAFM steel: Influence of HDA Melt Composition and Superheat, *Surf. Coat. Technol.*, 2017, **325**, p 697–707

135. M. A. Abro, and D. B. Lee, Effect of Al Hot-Dipping on High-Temperature Corrosion of Carbon Steel in $N_2$/0.1% $H_2S$ Gas, *Metals*, 2016, **6**, p 38

136. X. T. Li, L. J. Huang, S. L. Wei, Q. An, X. P. Cui, and L. Geng, Cycle Oxidation Behavior and Anti-oxidation Mechanism of Hot-dipped Aluminum Coating on TiBw/Ti6Al4V Composites with Network Microstructure, *Sci. Rep.*, 2018, **8**, p 5790

137. K. S. Forcey, D. K. Ross, and C. H. Wu, The Formation of Hydrogen Permeation Barriers on Steels by Aluminising, *J. Nucl. Mater.*, 1991, **182**, p 36–51

138. X. M. Yuan, H. G. Yang, W. W. Zhao, Q. Zhan, Y. Hu, and TMT Team, The Pack-cementation Process of Iron-aluminide Coating on China Low Activation Martensitic and 316L Austenitic Stainless Steel, *Fusion Sci. Technol.*, 2011, **60**, p 1065–1068

139. M. Jafarian, M. G. Mahjani, F. Gobal, and I. danaee, Electrodeposition of Aluminum from Molten $AlCl_3$–NaCl–KCl Mixture, *J. Appl. Electrochem.*, 2006, **36**, p 1169–1173

140. L. Barchi, U. Bardi, S. Caporali, M. Fantini, A. Scrivani, and A. Scrivani, Electroplated Bright Aluminium Coatings for Anticorrosion and Decorative Purposes, *Prog. Org. Coat.*, 2010, **67**, p 146–151

141. M. Lia, B. Gao, W. Chena, C. Liua, Z. Wanga, Z. Shia, and X. Hu, Electrodeposition Behavior of Aluminum from Urea-acetamide-lithium Halide Low-temperature Molten Salts, *Electrochim. Acta*, 2015, **185**, p 148–155

142. M. Lia, B. Gaoa, C. Liua, W. Chena, Z. Shia, X. Hua, and Z. Wang, Electrodeposition of Aluminum from $AlCl_3$/acetamide Eutectic Solvent, *Electrochim. Acta*, 2015, **180**, p 811–814

143. M. Galinski, A. Lewandowski, and I. Stepniak, Ionic Liquids as Electrolytes, *Electrochim. Acta*, 2006, **51**, p 5567–5580

144. D. Xue, Y. Chen, G. Ling, K. Liu, C. Chen, and G. Zhang, Preparation of Aluminide Coatings on the Inner Surface of Tubes by Heat Treatment of Al Coatings Electrodeposited From an Ionic Liquid, *Fusion Eng. Des.*, 2015, **101**, p 128–133

145. W. Krauss, J. Konys, and Sven-Erik Wulf, Corrosion Barriers Processed by Al Electroplating and their Resistance Against Flowing Pb–15.7Li, *J. Nucl. Mater.*, 2014, **455**, p 522–526

146. M. Galinski, A. Lewandowski, and I. Stepniak, Ionic Liquids as Electrolytes, *Electrochim. Acta*, 2006, **51**, p 5567–5580

147. Q. Zhang, Q. Wang, S. Zhang, X. Lu, and X. Zhang, Electrodeposition in Ionic Liquids, *ChemPhysChem*, 2016, **17**, p 335–351

148. S. Z. El Abedin, and F. Endres, Electrodeposition of Metals and Semiconductors in Air- and Water-Stable Ionic Liquids, *ChemPhysChem*, 2006, **7**, p 58–61

149. W. Simka, D. Puszczyk, and G. Nawrat, Electrodeposition of Metals from Non-aqueous Solutions, *Electrochim. Acta*, 2009, **54**, p 5307–5319

150. https://en.wikipedia.org/wiki/Deep_eutectic_solvent

151. J. Sun, and Ying-Chun Sun, Chemical Liquid Phase Deposition of Thin Aluminum Oxide Films, *Chin. J. Chem.*, 2004, **22**, p 661–667

152. P. Mohan, B. Yao, T. Patterson, and Y. H. Sohn, Electrophoretically Deposited Alumina as Protective Overlay for Thermal Barrier Coatings against CMAS Degradation, *Surf. Coat. Technol.*, 2009, **204**, p 797–801

153. R. Kavitha, and V. Jayaram, Deposition and Characterization of Alumina Films Produced by Combustion Flame Pyrolysis, *Surf. Coat. Technol.*, 2006, **201**, p 2491–2499

154. J. Exner, M. Hahn, M. Schubert, D. Hanft, P. Fuierer, and R. Moos, Powder Requirements for Aerosol Deposition of Alumina Films, *Adv. Powder Technol.*, 2015, **26**, p 1143–1151

155. Y. L. Wu, J. Hong, D. Peterson, J. Zhou, T. S. Cho, and D. N. Ruzic, Deposition of Aluminum Oxide by Evaporative Coating at Atmospheric Pressure (ECAP), *Surf. Coat. Technol.*, 2013, **237**, p 369–378

156. Q. X. Liu, S. Zein El Abedin, and F. Endres, Electroplating of Mild Steel by Aluminium in a First Generation Ionic Liquid: A Green Alternative to Commercial Al-Plating in Organic Solvents, *Surf. Coat. Technol.*, 2006, **201**, p 1352–1356

157. D. I. A. Fomin: PhD thesis, Studies on the Electrodeposition of Aluminium from different Air and Water Stable Ionic Liquids, Maschinenbau University, Clausthal, Germany, 2010

158. T. J. Tuaweri, E. M. Adigio, and P. P. Jombo, A Study of Process Parameters for Zinc Electrodeposition from a Sulphate Bath, *International Journal of Engineering Science Invention*, 2013, **2**, p 17–24

159. R. K. Choudhary, V. Kain, and R. C. Hubli, Formation of Alumina Aluminide Coatings on Ferritic-Martensitic T91 Steel, *J. Min. Metall. Sect. B-Metall.* 2014, **50 (2) B**, p 165 – 170

160. ASTM International, Designation: B499 − 09 (Reapproved 2014), Standard Test Method for Measurement of Coating Thicknesses by the Magnetic Method: Nonmagnetic Coatings on Magnetic Basis Metals

161. J. Durkee, Cleaning of aluminum: Harvey in North Dakota writes…, *Metal Finishing*, 2009, **107**, p 60–62

162. C. H. Voon, M. N. Derman, U. Hashim, K. R. Ahmad, and K. L. Foo, Effect of Temperature of Oxalic acid on the Fabrication of Porous Anodic Alumina From Al–Mn Alloys, *J. Nanomater.*, 2013, **2013**, p 1–8

163. W. J. Stępniowski, and Z. Bojar, Synthesis of Anodic Aluminum Oxide (AAO) at Relatively High Temperatures. Study of the Influence of Anodization Conditions on the Alumina Structural Features, *Surf. Coat. Technol.*, 2011, **206**, p 265–272

164. A. M. Abd-Elnaiem, A. M. Mebed, A. Gaber, and M. A. Abdel-Rahim, Effect of the Anodization Parameters on the Volume Expansion of Anodized Aluminum Films, *Int. J. Electrochem. Sci.*, 2013, **8**, p 10515–10525

165. A. M. Abd-Elnaiem, A. M. Mebed, W. Ahmed El-Said, and M. A. Abdel-Rahim, Porous and Mesh Alumina Formed by Anodization of High Purity Aluminum Films at Low Anodizing Voltage, *Thin Solid Films*, 2014, **570**, p 49–56

166. A. P. Schuetze, W. Lewis, C. Brown, and W. J. Geerts, A Laboratory on the Four-point Probe Technique, *Am. J. Phys*, 2004, **72**, p 149–153

167. M. Zhang, V. Kamavaram and R. G. Reddy, Aluminum Electrowinning in Ionic Liquids at Low Temperature, *J. Light Met.*, 2005, ed. Halvor Kvande, TMS, Warrendale, p 583–588

168. T. Jiang, M. J. Chollier Brym, G. Dubé, A. Lasia, and G. M. Brisard, Electrodeposition of Aluminium from Ionic Liquids: Part I—Electrodeposition and Surface Morphology of Aluminium from Aluminium Chloride ($AlCl_3$)–1-Ethyl-3-Methylimidazolium Chloride ([EMIm]Cl) Ionic Liquids, *Surf. Coat. Technol.*, 2006, **201**, p 1–9

169. S. Sakoda, and K. Tosha, Shot Peening using Wet Blasting Machine with a Wide Nozzle, *Mater. Sci. Forum*, 2009, **614**, p 163–168

170. Q. X. Liu, S. Zen El Abedin, and F. Endres, Electrodeposition of Nanocrystalline Aluminum: Breakdown of Imidazolium Cations Modifies the Crystal Size, *J. Electrochem. Soc.*, 2008, **155**, p D357–D362

171. S. Schaltin, M. Ganapathi, K. Binnemans, and J. Fransaer, Modeling of Aluminium Deposition from Chloroaluminate Ionic Liquids, *J. Electrochem. Soc.*, 2011, **158**, p D634–D639

172. C. W. Tobias, M. Eisenberg, and C. R. Wilke, Diffusion and Convection in Electrolysis—A Theoretical Review, *J. Electrochem. Soc.*, 1952, **99**, p 359C–365C

173. A. Brenner and S. Senderoff, Calculation of Stress in Electrodeposits from the Curvature of a Plated Strip, *Journal of Research*, 1949, **42**, p 105-123

174. G. R. Stafford, O. E. Kongstein, and G. M. Haarberg, In Situ Stress Measurements during Aluminum Deposition from $AlCl_3$-EtMeImCl Ionic Liquid, *J. Electrochem. Soc.*, 2006, **153**, p C207–C212

175. G. Yue, X. Lu, Y. Zhu, X. Zhang, and S. Zhang, Surface Morphology, Crystal Structure and Orientation of Aluminium Coatings Electrodeposited on Mild Steel in Ionic Liquid, *Chem. Eng. J.*, 2009, **147**, p 79–86

176. J. P. Zhao, X. Wang, Z. Y. Chen, S. Q. Yang, T. S. Shi, and X. H. Liu, Overall Energy Model for Preferred Growth of TiN Films during Filtered Arc Deposition, *J. Phys. D: Appl. Phys.*, 1997, **30D**, p 5–12

177. J. Konys, W. Krauss, and N. Holstein, Development of Advanced Al Coating Processes for Future Application as Anti-corrosion and T-permeation Barriers, *Fusion Eng. Des.*, 2010, **85**, p 2141–2145

178. S. Caporali, A. Fossati, and U. Bardi, Oxidative Post-treatments for Enhanced Corrosion Resistance of Aluminium Electrodeposited from Ionic Liquids, *Corros. Sci.*, 2010, **52**, p 235–241

179. H. Masuda, F. Hasegwa, and S. Ono, Self-Ordering of Cell Arrangement of Anodic Porous Alumina Formed in Sulfuric Acid Solution, *J. Electrochem. Soc.*, 1997, **144**, p L127–L130

180. L. Zaraska, G. D. Sulka, J. Szeremeta, and M. Jaskula, Porous Anodic Alumina formed by Anodization of Aluminum Alloy (AA1050) and High Purity Aluminum, *Electrochim. Acta*, 2010, **55**, p 4377–4386

181. T. T. Kao, and Y. C. Chang, Influence of Anodization Parameters on the Volume Expansion of Anodic Aluminum Oxide Formed in Mixed Solution of Phosphoric and Oxalic Acids, *Appl. Surf. Sci.*, 2014, **288**, p 654–659

182. P. Bocchetta, C. Sunseri, A. Bottino, G. Capannelli, G. Chiavarotti, S. Piazza, and F. D. Quarto, Asymmetric Alumina Membranes Electrochemically Formed in Oxalic Acid Solution, *J. Appl. Electrochem.*, 2002, **32**, p 977–985

183. J. K. Chang, C. M. Liao, C. H. Chen, and W. T. Tsai, Microstructure and Electrochemical Characteristics of Aluminum Anodized Film Formed in Ammonium Adipate Solution, *J. Electrochem. Soc.*, 2003, **150**, p B266–B273

184. S. Stojadinovic, I. Belca, M. Tadic, B. Kasalica, Z. Nedic, and L. Zekovic, Galvanoluminescence Properties of Porous Oxide Films Formed by Anodization of Aluminum in Malonic acid, *J. Electroanal. Chem.*, 2008, **619-620**, p 125–130

185. R. B. Mason, Factors Affecting the Formation of Anodic Oxide Coatings in Sulfuric Acid Electrolytes, *J. Electrochem. Soc.*, 1955, **102**, p 671–675

186. J. Wang, C. W. Wang, S. Y. Li, and F. Zhou, The Effect of Oxalic and Sulfuric Ions on the Photoluminescence of Anodic Aluminum Oxide Formed in a Mixture of Sulfuric and Oxalic Acid, *Appl. Phys. A Mater. Sci. Process.*, 2009, **94**, p 939–942

187. W. J. Stepniowski, M. Norek, M. M. Domanska, A. Bombalska, A. N. Stepniowska, M. Kwasny, and Z. Bojar, Fabrication of Anodic Aluminum Oxide with Incorporated Chromate Ions, *Appl. Surf. Sci.*, 2012, **259**, p 324–330

188. T. M. Naief, and K. H. Rashid, First Scientific Conference on Modern Technologies in Oil and Gas Refinery-Chemical Eng. Dept., University of technology and midland refineries company, 2011

189. A. O. Araoyinbo, A. F. M. Noor, S. Sreekantan, and A. Aziz, Voltage Effect on Electrochemical Anodization of Aluminum at Ambient Temperature, *IJMME*, 2010, **5**, p 53–58

190. A. O. Araoyinbo, A. Rahmat, M. N. Derman, and K. R. Ahmad, Room Temperature Anodization of Aluminum and the Effect of the Electrochemical Cell in the Formation

of Porous Alumina films from Acid and Alkaline Electrolytes, *Adv. Mater. Lett.*, 2012, **3**, p 273–278

191. ASTM: B244-09, Standard Test Method for Measurement of Thickness of Anodic Coatings on Aluminum and of other Nonconductive Coatings on Nonmagnetic Basis Metals with Eddy-current Instruments, 2014, www.astm.org/standards/B244.htm

192. M. Zulfequar, and A. Kumar, Effect of Porosity on Electrical Conductivity of Hot Pressed AlN Ceramic, *Revue de Physique Appliquée*, 1986, **21**, p 525–529

193. M. F. Morks, I. Cole, P. Corrigan, and A. Kobayashi, Electrochemical Characterization of Plasma Sprayed Alumina Coatings, *JSEMAT*, 2011, **1**, p 107–111

194. P. A. Steinmann, Y. Tardy, and H. E. Hintermann, Adhesion Testing by Scratch Test Method: the Influence of Intrinsic and Extrinsic Parameters on the Critical Load, *Thin Solid Films*, 1987, **154**, p 333–349

195. J. C. Nelson, and R. A. Oriani, Stress Generation during Anodic Oxidation of Titanium and Aluminum, *Corros. Sci.*, 1993, **34**, p 307–326

196. L. Chouanine, M. Takano, F. Ashihara, and O. Kamiya, Surface Failure Mode Evaluation of Pure AlN and AlN with $Al_2O_3$ (0.1 μm) Oxide Layer by Microscratch Testing, *J. Mater. Sci.*, 2005, **40**, p 5703–5710

197. E. Lopez, F. Beltzung, and G. Zambelli, Measurement of Cohesion and Adhesion Strengths in Alumina Coatings Produced by Plasma Spraying, *J. Mater. Sci. Lett.*, 1989, **8**, p 346–348

198. T. C. Cheng, and C. C. Chou, The Electrical and Mechanical Properties of Porous Anodic 6061-T6 Aluminum Alloy Oxide Film, *J. Nanomater.*, 2015, **2015**, p 1–5

199. S. J. Bull, and E. G. Berasetegui, An Overview of the Potential of Quantitative Coating Adhesion Measurement by Scratch Testing, *Tribol. Int.*, 2006, **39**, p 99–114

200. P. J. Burnett, and D. S. Rickerby, The Relationship between Hardness and Scratch Adhesion, *Thin Solid Films*, 1987, **154**, p 403–416

201. H. E. Evans, Modelling Oxide Spallation, *Mater. High Temp.*, 1994, **12**, p 219–227

202. M. Asmani, C. Kermel, A. Leriche, and M. Ourak, Influence of Porosity on Young's Modulus and Poisson's Ratio in Alumina Ceramics, *J. Eur. Ceram. Soc.*, 2001, **21**, p 1081–1086

203. A. Ramalho, and J. C. Miranda, The Relationship between Wear and Dissipated Energy in Sliding Systems, *Wear*, 2006, **260**, p 361–367

204. R. Zhang, K. Jiang, Y. Zhu, H. Qi, and G. Ding, Ultrasound-assisted Anodization of Aluminum in Oxalic Acid, *Appl. Surf. Sci.*, 2011, **258**, p 586–589

205. Z. H. Sun, C. L. Xu, and H. L. Zhang, Highly Ordered Nanoscale Patterns on Anodic Aluminum Oxide (AAO) Surface, *Solid State Phenom.*, 2007, **121–123**, p 445–448

206. G. E. J. Poinern, N. Ali, and D. Fawcett, Progress in Nano-Engineered Anodic Aluminum Oxide Membrane Development, *Materials*, 2011, **4**, p 487–526

207. http://www.xpsfitting.com/2008/09/aluminum.html

# Thesis Highlight

**Name of the Student:** Rupesh Kumar Choudhary

**Name of the CI/OCC:** Bhabha Atomic Research Centre, Mumbai **Enrolment No.:** ENGG01201204015

**Thesis Title:** Formation of Alumina Coatings by Thermal and Anodic Oxidation Processes and their Characterization

**Discipline:** Metallurgical Engineering **Sub-Area of Discipline:** Metallurgical Engineering

**Date of viva voce:** 28th August 2020

Alumina, because of its excellent physical, chemical and mechanical properties, is considered as an important coating material for electronic and electrical devices, automobile and machinery, thermal engineering, energy, cutting tools, orthopaedic implants, etc. The high tritium permeation reduction factor of alumina makes it a potential candidate for their use as tritium permeation barrier for Test Blanket Modules (TBMs) of fusion reactors.

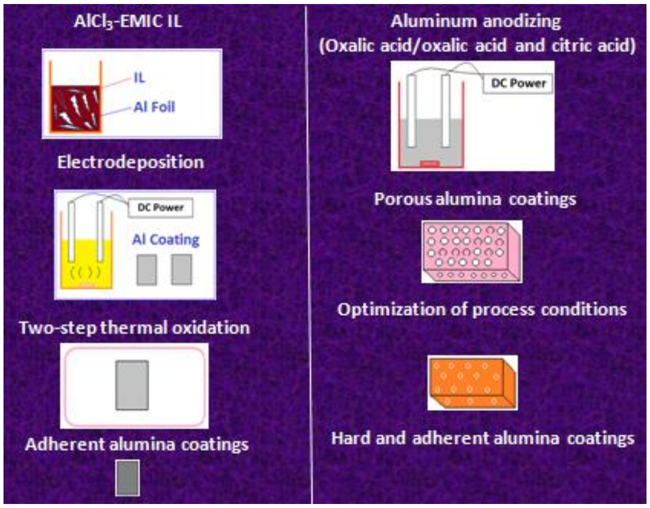

*Figure. Development of alumina coatings by thermal and anodic oxidation methods*

In this work, alumina coatings were formed by two different approaches. In the first approach, alumina coatings were developed for TBM related applications by thermal oxidation of the aluminum electrochemically obtained on T91 steel from $AlCl_3$-1-ethyl-3-methyl-imidazolium chloride ionic liquid. The so formed alumina coatings were studied for their crystalline phase, chemical composition and adhesion. Before converting aluminum to alumina the effect of bath purity, substrate types and their pre-treatments, and bath agitation on the properties of aluminum coatings was established. Alumina coatings formed by two-stage thermal oxidation of electrodeposited aluminum showed the formation of amorphous alumina having adhesive strength better than 20N. In the second approach, alumina coatings were developed for improving the corrosion behaviour of aluminum, by anodizing aluminum in oxalic acid and mixtures of oxalic acid and citric acid. The anodic alumina coatings did not show the formation of crystalline phase. By analysis of acoustic emission signal and optical microscopy imaging of scratch track during scratch testing it could be established that the coating formed at higher anodizing potential had inferior adhesive strength. Hardness, wear resistance and electrical resistivity of the coatings were found to improve as the potential during anodizing was increased.